A Search for Supersymmetry with Same–Sign Tau and Lepton Final States at the CMS Experiment

ARLO EMRYS GUNERATNE BRYER

High Energy Particle Physics

Blackett Laboratory
Imperial College London

Abstract

A search for Supersymmetry signals with Same–Sign Dileptons in the final state at the Large Hadron Collider is presented. The results are based on $976 \, \text{pb}^{-1}$ of pp collision data recorded by the Compact Muon Solenoid experiment at $7 \, \text{TeV}$ centre of mass energy. The analysis strategy for channels including a hadronically decaying τ ($e\tau, \mu\tau, \tau\tau$) is discussed in detail. The numbers of observed events are compatible with the expectation from Standard Model processes in all the considered channels with a total of 2.9 ± 1.7 predicted and 3 observed. An Upper Limit of total observed events from New Physics is extracted at the 95% Confidence Level and is equal to 5.8. The results are interpreted in the Constrained Minimal Supersymmetric Standard Model and a simplified Supersymmetry model favouring τ channels characterised by $\text{pp} \rightarrow \widetilde{g}\widetilde{g}$ with $Br(\widetilde{g} \rightarrow \widetilde{\chi}_1^{\pm} qq') = 100\%$ and $Br(\widetilde{\chi}_1^{+} \rightarrow \widetilde{\chi}_1^{0} \tau^{+} \nu_{\tau}) = 100\%$. A lower limit of $400 \, \text{GeV}$ on the gluino mass is set in the simplified model for neutralino masses up to $350 \, \text{GeV}$, with the exception of the region around $m_{\widetilde{g}} \approx m_{LSP}$. This exclusion extends to gluino masses of up to $620 \, \text{GeV}$ for neutralino masses of less than $100 \, \text{GeV}$.

Declaration

This thesis shows the work from the first officially approved CMS Same–Sign Dilepton analyses performed from 2009 to 2011. All work in chapters 4, 5 and 6, excluding 5.1.4 which was performed exclusively by Dr. M. Pioppi, is mine unless referenced and was carried out within the context of the Imperial College London and CERN SUSY groups and the greater CMS collaboration. Work by others is explicitly referenced throughout.

Arlo Guneratne Bryer, April 2012.

Acknowledgements

Working at CERN and analysing the first LHC data has been a truly thrilling experience and I have a lot of people to thank for helping along the way. Firstly, and most importantly, I'd like to thank Michele Pioppi for his extensive guidance and patience throughout the last few years – he has played a crucial role in my work from day one and I am very grateful and indebted to him. Thanks to my supervisor Oliver Buchmüller for providing moral and academic support as well as fascinating research topic.

A lot of colleagues outside my immediate working environment whilst at CERN have played a role in my work. These people include the members of the 'Imperial College and Friends' (ICF) working group and Alex Mott, Andrea Bocci and Massimiliano Chiorboli for their help with the HLT paths.

Thanks to my friends, old and new, who provided distraction and amusement when things got too intense, and in the case of my Imperial/CERN friends for the endless (sometimes on topic) arguing and discussing. In this vein, a big thanks to my good friend and colleague Alex Sparrow who has taught me a lot about computing and helped me far too many times to count. Thanks to Cat for putting up with it all and doing her best to keep me vaguely sane.

Finally, thank you to my immediate family who have provided enduring support throughout, in particular my parents who even found the time to do some proof reading.

Contents

List of Figures

List of Tables

"Nothing ever becomes real till it is experienced."
    — John Keats

Introduction

The last four decades of High Energy Physics (HEP) saw the confirmation of the Standard Model (SM) of particle physics. Notable highlights include the exploration of the weak force performed in various precursor experiments at the European Organization for Nuclear Research (CERN). In particular these comprised the discovery of neutral currents [1] followed by direct observation of the weak bosons [2–5], and finally, precision measurements performed by the Large Electron-Positron Collider (LEP) [6] experiments before the construction of the Large Hadron Collider (LHC). Prior to the LHC, the Tevatron at FermiLab was the highest energy hadron collider ($\sqrt{s} = 1.96$ TeV) in the world. Amongst its various successes was most notably the discovery of the top quark [7]. The Tevatron was finally stopped in September 2011.

The exploration of the SM is then a success of modern theoretical and experimental particle physics, having produced a powerful and generally well verified understanding of the fundamental constituents and behaviour of matter.

The LHC [8] and associated detectors build on the discoveries and confirmation of the SM as a description of particle physics below the 1 TeV scale. The increase in energy and detector technology with respect to the previous Tevatron generation are expected to yield discoveries of anticipated New Physics (NP) and the Higgs boson [9], as predicted by the mechanism of electroweak symmetry breaking, which has been searched for inconclusively at both LEP and the Tevatron and is the final piece of the SM.

For all the well measured predictions the SM has provided, there are some major problems with the scope and construction of the theory itself. Two clear experimental indicators exist. Firstly, there is the obvious omission of any description of gravity and its interactions at the fundamental scale. Secondly, and particularly in recent years from the area of astrophysics, there is conclusive evidence for the existence of Dark Matter (DM) [10] which also sits outside the framework of the SM. Theoretical arguments regarding the shortcomings of the SM have existed for some time and include fine–tuning cancellation of radiative corrections of the Higgs boson mass and the difficulty with

including gravity into the theoretical framework [11]. Additionally, the discovery or exclusion of the Higgs boson would, given the current extent of the excluded mass range [12], hint at the existence of NP at some higher energy scale.

Supersymmetry (SUSY) [13] has generated a large amount of interest and theoretical work in light of the aforementioned problems with the current status of experimental findings and theoretical structure of the SM [14]. The central postulate of the idea proposes that there exists a fundamental symmetry between bosons and fermions, thus fixing some theoretical problems with the SM as well as providing a set of predictive models for NP. Some important features include a potential candidate particle for the Cold Dark Matter (CDM) problem as well as a rich phenomenology in terms of expected signatures at a hadron collider. Importantly, SUSY cascades are favourable to final states including heavy leptons for certain regions of parameter space and leptonic final states may provide a means to probe the mass spectrum of any newly discovered particles [14, 15].

Although the signatures for SUSY and NP are varied, the LHC presents a particular challenge in correctly identifying these events from the large SM background produced at a hadron collider. Channels with low SM irreducible background offer an interesting prospective for discovery in the early years of running. In particular, the request for Same–Sign Dilepton (SSDL) provides a signature sensitive to NP with few SM processes producing the same final state.

This thesis presents a search for SUSY in SSDL final states based on a data sample corresponding to an integrated luminosity of 976 pb^{-1} collected in pp collisions at a centre of mass energy of $\sqrt{s} = 7$ TeV by the Compact Muon Solenoid (CMS) experiment. Particular attention is given to the τ inclusive final states. The thesis is organised in the following manner: a summary of the SM and overview of the primary features of SUSY and its phenomenological implications at the LHC is presented in chapter 1. Chapters 2 and 3 introduce the LHC machine, CMS detector components and performance as well as a description of the reconstruction methods used at CMS to define the physics objects used in the presented study. The SSDL analysis is then discussed in three sections with a focus on the τ channel components. Firstly the triggers and selection used in the τ SSDL analysis are shown in chapter 4. This chapter also includes the selection performance on Monte Carlo (MC) and associated MC background studies. Chapter 5 details the methods used in evaluating the SM background contribution as well as an assessment of the systematic errors. Finally, the results of the τ based SSDL analysis and a review of the light lepton (ee, eμ and $\mu\mu$) SSDL analysis and results are shown in chapter 6.

Natural units ($c = \hbar = k_B = 1$) are used throughout when referring to particle energies, momenta and masses.

Chapter 1.

Theoretical Background and Motivation

The theoretical understanding of matter and interactions went through major changes in the very late 19$^{\text{th}}$ and early 20$^{\text{th}}$ centuries. The discoveries of the elementary nature of particles like electrons and photons along with the start of the quantum and relativistic eras gave rise to very quick improvements in the theoretical picture of the time. By the 1950s a full quantum field theory of electrodynamics had been established, numerous features of the weak force were understood and a plethora of new particles had been discovered.

The following decade saw major successes in understanding particle physics using theoretical concepts of gauge invariance along with subsequent experimental evidence supporting the predictions. In particular, the unification of the then distinct Quantum Electro Dynamics (QED) and weak force to produce the current electroweak force was confirmed by the observation of weak neutral currents at CERN. The introduction of quarks and Quantum Chromo Dynamics (QCD) simplified the picture of previously discovered hadrons to bound states of the newly postulated fundamental quarks. Finally the idea of spontaneous symmetry breaking of the electroweak force via the Higgs mechanism was also postulated as a way of introducing mass naturally to the SM.

The sections below present an outline of the theoretical framework of the SM of particles and their interactions, with a particular focus on the electroweak and Higgs sectors. A full discussion of these topics may be found in [11, 16–21]. Constraints on the expected Higgs mass are also briefly discussed to illustrate what may be inferred from a Higgs–like observation at the LHC on the scale of NP. Finally, the shortcomings of the SM are

presented to motivate SUSY as a potential solution. SUSY is then discussed with an emphasis on expected phenomenology at the LHC.

1.1. The Standard Model

The SM is constructed as a local gauge invariant, renormalisable quantum field theory comprising a $SU(2)_L \otimes U(1)_Y$ electroweak sector and a $SU(3)$ strong (QCD) sector describing all known fermions, bosons and their interactions [11, 16, 17, 19].

The electroweak part of this structure is spontaneously broken via the Higgs mechanism which produces three massive spin-1 particles ($W^\pm$ and Z), one massless spin-1 particle (γ) and a yet to be discovered spin-0 Higgs boson. The masses of the other fermions in the theory are produced by coupling to the Higgs field.

The strong $SU(3)$ sector is assumed to be an unbroken symmetry.

In the following, the electroweak sector of the SM is first presented to introduce the matter fields and electroweak bosons. This is followed by a description of the Higgs mechanism [22–24] and electroweak symmetry breaking. Finally, the strong QCD sector is described.

1.1.1. Electroweak Sector

The electromagnetic and weak interactions between quarks and leptons is described by a Yang–Mills theory built from the $SU(2)_L \otimes U(1)_Y$ symmetry group.

Ignoring the Higgs sector, there exist two kinds of fields in the SM – the chiral quark and lepton (both fermion) fields and the force carrier bosons corresponding to the gauge fields.

The quarks and leptons exist in three generations. The weak force couples in a vector - axialvector ($V - A$) manner ($\gamma^\mu (1 - \gamma^5)$) whilst the electromagnetic force displays a purely vectorial (γ^μ) coupling. By introducing the concept of chirality via a projection defined as:

$$u_{R,L} = \frac{1 \pm \gamma^5}{2} u,$$

(1.1)

where γ^5 is defined as the product of the gamma matrices [11], we obtain the right and left handed projections ($u_{R,L}$) of the fermion spinor. The left-handed and right-handed fermions are in weak isospin doublets and singlets respectively. The weak force couples to left-handed particles and right-handed anti-particles. This feature of weak interactions combined with the different transformation of doublets and singlets under SU(2) accounts for parity violation in the SM.

The gauge fields of the theory correspond to the generators of the underlying symmetry. The electroweak sector has four such fields – B_μ corresponding to the single Y generator (hypercharge) of the $U(1)_Y$ group and $W_\mu^{i=1,2,3}$ corresponding to the three generators $T_i = \frac{1}{2}\tau_i$ of $SU(2)_L$. These four fields mix to produce the carriers (W$^\pm$, Z and γ) of the electroweak force as expressed in equations 1.2, 1.3 and 1.4.

$$W_\mu^\pm = \frac{1}{\sqrt{2}}(W_\mu^1 \mp W_\mu^2) \tag{1.2}$$

$$A_\mu = B_\mu \cos\theta_w + W_\mu^3 \sin\theta_w \tag{1.3}$$

$$Z_\mu = -B_\mu \sin\theta_w + W_\mu^3 \cos\theta_w \tag{1.4}$$

The fields representing the charged W$^\pm$ are produced in a linear combination of the charged weak isospin fields. The neutral W^3 and B fields mix to produce the neutral Z and γ. θ_w is the weak mixing angle.

1.1.2. Spontaneous Symmetry Breaking and the Higgs Sector

The electroweak part of the SM may be considered as:

$$\mathcal{L}_{electroweak} = \mathcal{L}_{scalar} + \mathcal{L}_{fermion} + \mathcal{L}_{gauge} + \mathcal{L}_{Yukawa}, \tag{1.5}$$

The fermion and gauge fields have been described in section 1.1.1.

The Lagrangian needs ultimately to generate three massive gauge bosons (W$^\pm$ and Z) and the massless photon. This is achieved via spontaneous symmetry breaking of $SU(2)_L \otimes U(1)_Y$ (the local gauge invariance of the electroweak theory) to $U(1)_{EM}$. The Goldstone theorem states that for every broken generator of a continuous symmetry

there is an additional massless 'Nambu–Goldstone' boson [25]. These are absorbed as an additional degree of freedom to the gauge bosons via the Higgs mechanism.

Consider firstly the bosonic section of this Lagrangian $\mathcal{L}_{boson} = \mathcal{L}_{scalar} + \mathcal{L}_{gauge}$ which may be written as:

$$\mathcal{L}_{boson} = (D_\mu \Phi)^\dagger (D^\mu \Phi) - V(\Phi) - \frac{1}{4}(B_{\mu\nu}B^{\mu\nu} + W^a_{\mu\nu}W^{a,\mu\nu}), \tag{1.6}$$

where Φ is a complex SU(2) doublet of scalar fields $\phi_{i=1,2,3,4}$ – the Higgs doublet:

$$\Phi = \begin{pmatrix} \phi^+ \\ \phi^0 \end{pmatrix} = \frac{1}{\sqrt{2}} \begin{pmatrix} \phi_1 + i\phi_2 \\ \phi_3 + i\phi_4 \end{pmatrix}, \tag{1.7}$$

and $V(\Phi)$ is the Higgs potential:

$$V(\Phi) = \mu^2 \Phi^\dagger \Phi + \lambda(\Phi^\dagger \Phi)^2, \tag{1.8}$$

which is invariant under SU(2) $\otimes$ U(1) and renormalisable as required. The scalar Higgs field is assigned hypercharge $Y = +1$ and transforms under the complete $SU(2) \otimes U(1)$ gauge as:

$$\Phi \rightarrow e^{i\alpha^a \tau^a} e^{i\beta/2} \Phi. \tag{1.9}$$

The covariant derivative D_μ may be written as:

$$D_\mu = \partial_\mu + ig\frac{\tau^i}{2}W^i_\mu + ig'\frac{Y}{2}B_\mu, \tag{1.10}$$

where g and g' are the coupling constants of the W^i_μ and B_μ SU(2) and U(1) gauge fields respectively. The gauge fields have strength tensors:

$$W^i_{\mu\nu} = \partial_\mu W^i_\nu - \partial_\nu W^i_\mu - g\epsilon_{ijk}W^j_\mu W^k_\nu \tag{1.11}$$

and

$$B_{\mu\nu} = \partial_\mu B_\nu - \partial_\nu B_\mu, \tag{1.12}$$

where ϵ_{ijk} is the anti-symmetric Levi–Civita symbol.

The Higgs potential (equation 1.8) displays two main behaviours depending on the choice of μ^2. The λ parameter is required to be positive to maintain vacuum stability. For $\mu^2 > 0$, the minimum of the potential $V(\Phi)$ is at $\Phi = 0$ and the gauge symmetry is unbroken. However, for $\mu^2 < 0$, the Φ field acquires a non-zero Vacuum Expectation Value (VEV) thereby spontaneously breaking the local gauge symmetry. This may be written as:

$$\langle 0|\Phi|0\rangle = \frac{1}{\sqrt{2}} \begin{pmatrix} 0 \\ v \end{pmatrix} \quad \text{where} \quad v = (-\mu^2/\lambda)^{1/2}. \tag{1.13}$$

This achieves the desired symmetry breaking of $SU(2) \otimes U(1)_Y$ leaving only the $U(1)_{EM}$ group of electromagnetism unbroken. The three broken generators produce massless fields as expected from Goldstone's theorem which can be absorbed as a third degree of freedom by three of the four vector bosons by choosing the unitary gauge of SU(2) thus producing three massive bosons. The remaining degree of freedom in Φ is the SM Higgs boson. This can be expressed as follows [11]:

$$\Phi = \frac{1}{\sqrt{2}} \begin{pmatrix} 0 \\ v \end{pmatrix} + \frac{1}{\sqrt{2}} \begin{pmatrix} \phi_1 + i\phi_2 \\ h + i\phi_3 \end{pmatrix} \xrightarrow{\text{unitary gauge}} = \frac{1}{\sqrt{2}} \begin{pmatrix} 0 \\ v + H \end{pmatrix}, \tag{1.14}$$

where $\phi_{i=1,2,3}$ are the massless Goldstone bosons which are removed by choosing the unitary gauge, and H is the remaining physical Higgs boson field.

Inserting this into the kinetic term $(D_\mu\Phi)^\dagger(D^\mu\Phi)$ of the Lagrangian in equation 1.6 generates masses for the W$^\pm$ and Z bosons whilst leaving the photon massless as required. This can be shown by considering only the relevant terms produced [11]:

$$\Delta\mathcal{L} = \frac{1}{2} \begin{pmatrix} 0 & v \end{pmatrix} (gW_\mu^i\tau^i + \frac{1}{2}g'B_\mu)(gW^{k\mu}\tau^k + \frac{1}{2}g'B^\mu) \begin{pmatrix} 0 \\ v \end{pmatrix}, \tag{1.15}$$

and evaluating the $W^i \tau^i$ term explicitly:

$$\Delta \mathcal{L} = \frac{v^2}{8} \left(g^2 (W_1^{\mu} + i W_2^{\mu}) + (g W_3^{\mu} + g' B^{\mu}) \right). \tag{1.16}$$

Three of the four vector bosons discussed in section 1.1.1 have now acquired mass terms with $m_W = g \frac{v}{2}$ for the W$^{\pm}$ and $m_Z = \frac{v}{2} \sqrt{g^2 + g'^2}$ for the Z. The physical photon is left massless.

In addition to providing mass to the vector bosons of the weak force, the Higgs field also provides a mechanism to produce massive fermions. Previously it was impossible to introduce mass terms 'by hand' to the lepton fields due to their $V - A$ structure. The scalar Higgs arranged in a complex $SU(2)$ doublet allows $SU(2) \otimes U(1)_Y$ invariant interactions of fermion fields ($SU(2)$ doublets or singlets) with the Higgs. The couplings of these interactions is contained within the $\mathcal{L}_{Yukawa}$ term of the Lagrangian in equation 1.5 and may be expressed as:

$$\mathcal{L}_{down} = -\lambda_e (\bar{L} \Phi e_R + \Phi^{\dagger} \bar{e}_R L) - \lambda_d (\bar{Q} \Phi d_R + \Phi^{\dagger} \bar{d}_R Q), \tag{1.17}$$

for leptons and down-type quarks, where L and Q represent the left-handed weak isodoublets of the leptons and the quarks respectively and the λ parameters are the Yukawa couplings. The second term for the lepton fields and quark fields are Hermitian conjugates of the first, which include $\bar{\Phi}$. This preserves total hypercharge of both the lepton and quark terms equal to 0 [21].

Finally, the Higgs field is self interacting. Considering the potential term in equation 1.8 after Electroweak Symmetry Breaking (EWSB):

$$V(h) = \frac{\mu^2}{2}(v + H)^2 + \frac{\lambda}{4}(v + H)^4 \tag{1.18}$$

$$= \lambda v^2 H^2 + \lambda v H^3 + \frac{\lambda}{4} H^4 - \frac{\lambda}{4} v^4, \tag{1.19}$$

which shows that the Higgs field is quantised by scalar massive particles of mass:

$$m_h = \sqrt{2}\mu = \sqrt{2\lambda}v, \tag{1.20}$$

determined by the parameter λ – the coupling of the Higgs to itself. The weak scale v in the theory can be expressed in terms of the Fermi constant G_F as $v = 2M_W/g \approx (\sqrt{2}G_F)^{-1/2} = 246$ GeV. The Higgs mass itself is unknown within the theory, with λ naively being able to have any value.

Theoretical bounds on the Higgs mass are outlined below for completeness.

Constraints on the Higgs Mass

There exist several theoretical arguments for relatively tight constraints on the mass of the Higgs, for a given scale Λ of NP [21, 26–28].

- Perturbative constraints: for $\lambda > 1$ the Higgs theory becomes strongly coupled. An upper bound on the Higgs mass may be found by considering what values the renormalised coupling λ_{renorm} may take and if m_h (equation 1.20) can be arbitrarily large. It can be shown considering the Renormalisation Group (RG) equation of the Higgs quartic coupling that the perturbative regime of the Higgs sector breaks down at some scale Λ (presumed NP scale) with exponential sensitivity to m_h.

- Unitarity constraints: considering Higgs boson contributions to the scattering amplitude of processes involving W and Z, it can be shown that $m_h < 780$ GeV and $\lambda \leq 5$.

- Stability constraints: the λ parameter of the Higgs potential (equation 1.8) needs to be positive and away from zero to ensure the potential is bound from below.

The bounds on the Higgs mass are shown as a function of energy scale Λ in figure 1.1 [28].

1.1.3. Quantum Chromo Dynamics

The strong interactions of the SM are described by a $SU(3)_c$ gauge theory with eight gluon fields $G_\mu^{=1,\dots,8}$ and quark matter fields. The corresponding gauge quantum number in this sector is colour charge, analogous to electric charge of QED.

The field strength tensor term of the QCD Lagrangian may be written as:

$$F_{\mu\nu}^i = \partial_\mu G_\nu^i - \partial_\nu G_\mu^i - g_s f_{ijk} G_\mu^j G_\nu^k, \tag{1.21}$$
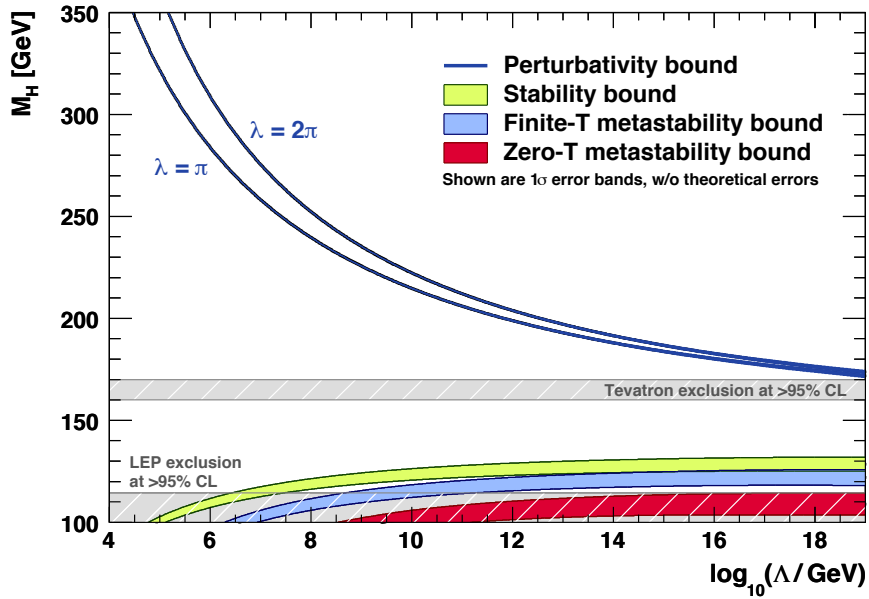
Figure 1.1.: Bounds on the Higgs mass from perturbative and stability arguments, as a function of energy scale Λ. Widths of the bands show uncertainties. The exclusions on the Higgs mass from the Tevatron and LEP experiments are shown. A description of the Finite-T and Zero-T metastabilitiy bounds may be found in [28]. Taken from [28].

where g_s is the QCD coupling constant and f_{ijk} are structure constants defined by the commutation relations of the Gell-Mann SU(3) matrices [18].

The last term of this shows that QCD includes three and four point self interactions; a property similar to the electroweak non-Abelian sector of the SM.

QCD is asymptotically free. At high energies/small scales (e.g. within baryons), the coupling becomes weak. It can be shown, and is verified experimentally, that colour charge is confined – quarks and gluons cannot be observed in isolation.

1.1.4. Problems with the Standard Model

Although the SM is a success of particle physics with remarkable agreement between theory and experiment, there exist several indications that it does not provide a complete picture. The hints of a deeper theory of nature arise in various fields. Firstly and most obviously, the SM provides no description of the fundamental interaction of matter and gravity.

Fine Tuning Problem

The discussion of the Higgs sector and its interaction with the other fields of the SM in section 1.1 excluded loop interactions. Equation 1.18 shows that there is a 4-boson self interacting term which, at the one-loop order correction, generates a contribution proportional to:

$$\lambda \int^{\Lambda} d^4 k \frac{1}{k^2 - m_h^2} \tag{1.22}$$
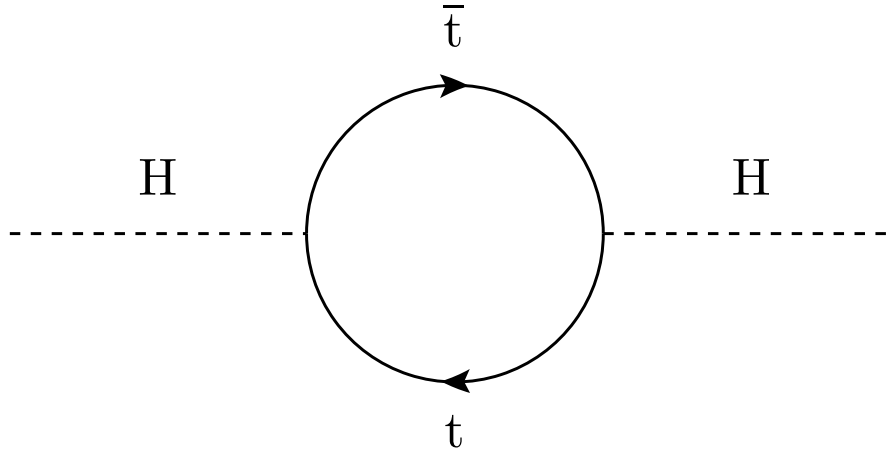
(a) Fermion correction to Higgs mass parameter.
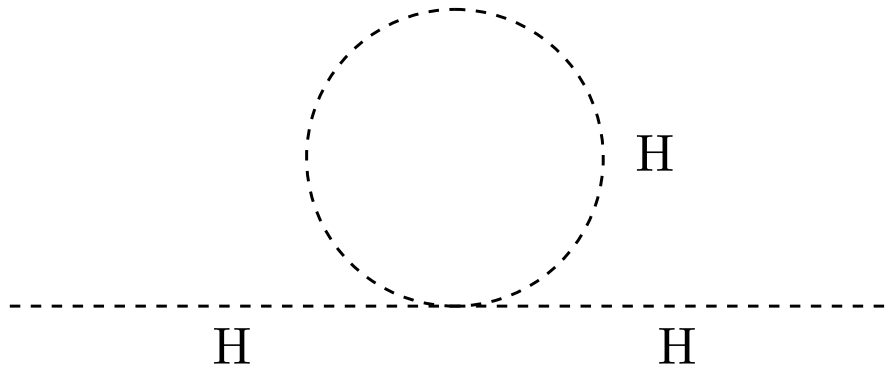
(b) Higgs mass squared correction from self interaction.

Figure 1.2.: First order quantum loop corrections to the Higgs mass parameter for a fermion loop and a scalar loop.

which, when evaluated, produces a positive correction of $\lambda \Lambda^2 \Phi^\dagger \Phi$ to the Higgs mass term $\mu^2 \Phi^\dagger \Phi$ in equation 1.8. This means the physical μ parameter of the Higgs potential becomes $\mu^2_{corrected} = \mu + \lambda \Lambda^2$. Additional similar corrections are produced in loops containing all the massive particles of the SM. These are illustrated in figure 1.2.

Here Λ is some physical cut-off scale of the theory imposed on the SM from the assumption that, for some energy scale, the model becomes invalid. This is expected for energies at most at the Planck scale ($\sim 10^{19}$ GeV) where quantum gravity effects must be considered, although it is reasonable to assume that this limit is reached for energies between this and the weak scale (~ 100 GeV).

The effect of the loop corrections pushes the Higgs μ^2 towards values approaching Λ. For Λ approaching Λ_{Planck} this becomes significantly greater than the expected ~ 100 GeV expected from the weak scale as well as being positive. In order to restore the desired weak scale and EWSB, *fine-tuning* of the bare (before corrections) μ^2 parameter is necessary.

Dark Matter

The presence of large quantities of weakly interacting, massive matter is observable at cosmological scales. This has been observed indirectly via the discrepancy between the theoretical expected rotation of galaxies based on their visible mass content and the observed rotation. This is commonly attributed to the presence of CDM [29]. Further, direct evidence has been observed in the collision of galaxy clusters, most notably in the Bullet cluster [30]. This provides the strongest direct empirical evidence to date. Finally, the latest Wilkinson Microwave Anisotropy Probe (WMAP) results have provided the best measurements of the parameters of the Lamda–CDM standard model of cosmology [31]. This constrains 'baryonic' matter (i.e. matter described by the SM) to around 4% whilst weakly interacting DM accounts for approximately 23%. The remaining mass content is made up of dark energy. The SM provides no description of DM, hinting at the existence of a more complete fundamental description of matter.

There exist several theoretical constructions of NP models which fix, in varying manners, the problems outlined above. A particularly appealing option is covered by SUSY theories.

1.2. Supersymmetry

SUSY [13, 32] introduces an excellent theoretical framework for naturally removing the fine tuning problem of the SM discussed in section 1.1.4. This is achieved by providing a fermion loop correction to the scalar one-loop correction and analogously a scalar

correction to the fermion loop. Considering the fermion contribution in figure 1.2a, the Higgs receives a contribution of the form $-g_f^2 \Lambda \Phi^\dagger \Phi$. Combined with the correction term from equation 1.22, the total contribution is of the form $(\lambda - g_f^2)\Lambda \Phi^\dagger \Phi$. In the situation where $g_f^2 = \lambda$, the Higgs mass corrections from quadratic divergences of Λ disappear.

In addition, several models of SUSY produce cascade decays ending in a massive, weakly interacting particle, providing a potential candidate to the DM problem.

SUSY particle theory postulates a new spacetime symmetry relating bosons and fermions. Specifically this is implemented via some spinor operator Q such that $Q\,|\text{boson}\rangle = |\text{fermion}\rangle$ and $Q\,|\text{fermion}\rangle = |\text{boson}\rangle$.

The lack of experimental evidence for the predicted sparticle spectrum implies SUSY must be a broken symmetry leading to sparticle masses greater than their SM counterparts.

1.2.1. The Minimal Supersymmetric Standard Model

The Minimal Supersymmetric Standard Model (MSSM) provides the minimal SUSY extension possible to the SM i.e. a corresponding superfield to each field of the SM. The SM fields and the associated superfields share the same quantum numbers from the underlying group structure of the SM. In addition, it can be shown from the commutation relations of the operator Q and the four-momentum operator P^μ that the number of bosonic and fermionic degrees of freedom for bosons and fermions in the same supermultiplet must be the same.

This produces an octet fermion field of 'gluinos' as superpartners to the SU(3) gluon fields and analogous SU(2) and U(1) fields – the 'winos' ($\widetilde{W}^\pm$) and 'bino' ($\widetilde{B}$). The combination of SM spin-1 bosons with a two component fermion is called a gauge supermultiplet. The SM leptons and quarks have corresponding spin-0 superpartners – 'sleptons' and 'squarks' – arranged in chiral supermultiplets for the left and right handed components originating from the SM weak interaction discussed in section 1.1.1.

The Higgs sector of the SM requires two Higgs doublets in SUSY. It can be shown [13] that this is due to the general structure of a SUSY theory. Specifically, the non-gauge interaction terms in a SUSY Lagrangian (which includes the mass terms) can not include $\phi^\dagger$ terms without violating the SUSY invariance of the Lagrangian. The SM fields and corresponding SUSY fields are summarised in table 1.1.

	spin-0	spin-1/2
squarks and quarks	$(\tilde{u}_L, \tilde{d}_L), \tilde{u}_R$	$(u_L, d_L), u_R$
sleptons and leptons	$(\tilde{\nu}_L, \tilde{e}_L), \tilde{e}_R$	$(\nu_L, e_L), e_R$
Higgs and higgsinos	(H_u^+, H_u^0)	$(\tilde{H}_u^+, \tilde{H}_u^0)$
	(H_d^0, H_d^-)	$(\tilde{H}_d^0, \tilde{H}_d^-)$
	spin-1/2	spin-1
gluino and gluon	$\tilde{g}$	g
winos, W fields	$\tilde{W}$	W
bino, B field	$\tilde{B}$	B

Table 1.1.: Arrangements of the chiral and gauge supermultiplets of the MSSM.

The broad features of the Minimal Supersymmetric Standard Model (MSSM) with soft SUSY breaking produce three interesting results [32]:

1. The Higgs sector in the MSSM is described by two Higgs doublets and predicts that the lightest physical Higgs boson should be ≤ 140 GeV.

2. The inverse running coupling constants of the strong, weak and electromagnetic force (α_{QCD}^{-1}, α_{weak}^{-1} and α_{EM}^{-1}) meet at high Q^2 assuming $\mathcal{O}(1\text{–}10$ TeV) as shown in figure 1.3, encouraging the idea of possible unification of the forces.

3. The mass parameters in the SM and any renormalisable SUSY are scale dependent in an analogous manner to the gauge couplings. It can be shown from the RG evolution that the Higgs m^2 may evolve from a positive to negative value for a scale 10^{16} GeV to 100 GeV and for sparticle masses of $\mathcal{O}(1$ TeV).

R-Parity

In order to adjust the basic phenomenology of the MSSM to be in agreement with experimental constraints, specifically the predicted decay of the proton, a new symmetry is introduced. The quantum number defined by R-parity (or matter parity) is
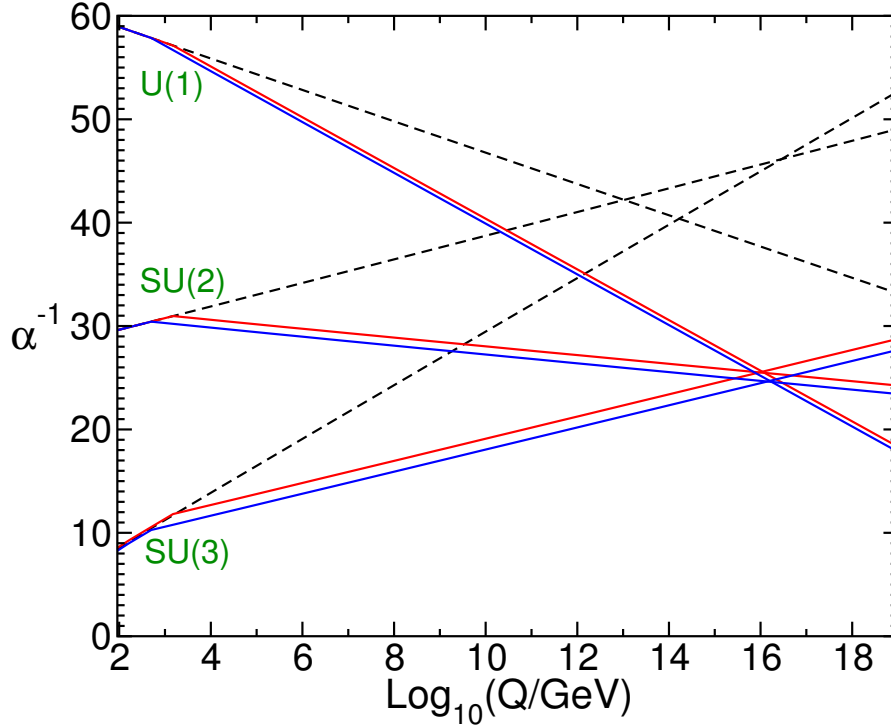
Figure 1.3.: Evolution of the inverse gauge couplings of the SM (dashed line) and MSSM (solid coloured lines). Taken from [13].

multiplicatively conserved and may be expressed as:

$$P_M = (-1)^{3(B-L)}, \tag{1.23}$$

where B and L are baryon and lepton numbers respectively. All SM particles have $P_R = +1$ (including the Higgs boson) whilst all sparticles have $P_R = -1$. This quantity introduces important phenomenological features of any manifestation of SUSY, including at hadron colliders where one expects direct production of sparticles. Assuming conserved R-parity, the Lightest Supersymmetric Particle (LSP) must be stable. If it is also weakly interacting it provides a potential candidate for DM. All sparticle decays must ultimately produce odd numbers of LSPs. Finally, sparticle production must always occur in pairs if produced at an accelerator. The LSP would escape detection at collider experiments, which, assuming knowledge of the centre of mass collision and a hermetic detector, can be exploited as a E_T^{miss} (missing energy in the transverse plane with respect to the beam line) signature in experimental searches.

SUSY Breaking

As previously mentioned it is known that if SUSY is the correct theory of particle physics beyond the weak scale, then it must also be broken since sparticles have never been observed experimentally. In a general and complete theory, the SUSY symmetry is expected to be broken spontaneously, in a similar manner to EWSB in the SM.

Although the exact mechanism for SUSY breaking at high energy scales may be implemented in a variety of manners, the MSSM may be extended 'by hand' to include symmetry breaking terms directly in the Lagrangian.

The symmetry breaking terms, which must be of positive mass dimension, may be added in a general manner via three gaugino masses (gluinos, winos and bino), scalar (squark and slepton) squared mass terms, Higgs squared mass terms and scalar cubed mass terms. The addition of the soft SUSY breaking terms takes the number of free parameters of the theory to 105. These may be constrained by the physics at the SM scale by noting that a lot of these parameters allow for unobserved physics – either excess CP violation or flavour changing neutral currents.

These constraints allow for the construction of the Constrained Minimal Supersymmetric Standard Model (CMSSM) such that at the Grand Unified Theory (GUT) scale the MSSM may be characterised by [13]:

$$M_{gluino} = M_{wino} = M_{bino} = m_{1/2}, \tag{1.24}$$

$$m^2_{sleptons} = m^2_{squarks} = m^2_0, \tag{1.25}$$

$$m^2_{H_u} = m^2_{H_d} = m^2_0,$$

$$\mathbf{a}_u = A_0 \mathbf{y}_u, \ \mathbf{a}_d = A_0 \mathbf{y}_d, \ \mathbf{a}_e = A_0 \mathbf{y}_e, \tag{1.26}$$

where equation 1.24 is the universal mass term of the gauginos, equation 1.25 is the common scalar mass and equation 1.26 is the common trilinear coupling. The $\mathbf{y}$ matrices are 3×3 matrices of Yukawa couplings. In addition to these three parameters, there is also the inclusion of $\tan \beta$ (discussed in section 1.2.1 below) and the sign of the higgsino mixing parameter μ.

This parameterisation of the MSSM provides significant simplification of the theory, with the phenomenology at the weak scale being fully described by the RG equations.

Masses in the Minimal Supersymmetric Standard Model

Mass generation in the MSSM proceeds in an analogous manner to EWSB in the SM described in section 1.1.2, albeit with additional complications due to the presence of two Higgs doublets $H_u = (H_u^+, H_u^0)$ and $H_d = (H_d^0, H_d^-)$. The VEVs of the Higgs doublets may be written as:

$$v_u = < H_u^0 > \quad \text{and} \quad v_d = < H_d^0 > \tag{1.27}$$

with their ratio defined as $\tan \beta = v_u/v_d$.

The VEVs are constrained by the mass of the SM Z^0 boson as:

$$v_u^2 + v_d^2 = \frac{2m_Z^2}{g^2 + g'^2} = 174 \text{ GeV}^2. \tag{1.28}$$

In analogy to EWSB in the SM with four degrees of freedom which produce the longitudinal polarisations of the $W^\pm$ and Z^0 and the physical SM Higgs boson, the eight degrees of freedom of the two Higgs doublets in the MSSM are accounted for as follows; three are massless and provide mass to the $W^\pm$ and Z, the other five are mass eigenstates h^0, H^0, A^0 and $H^\pm$.

EWSB in the MSSM causes the higgsinos and gauginos to mix. This produces four neutral mass eigenstates (neutralinos) via the mixing of one neutral $\tilde{H}_u^0$ or $\tilde{H}_d^0$ with one $\widetilde{B}$ or $\tilde{W}^0$, labelled $\widetilde{\chi}_{1,2,3,4}^0$. In addition to the neutralinos, mixing of $\widetilde{W}^+$ with $\tilde{H}_u^+$ and mixing of $\widetilde{W}^-$ with $\tilde{H}_d^-$ produces two positively and two negatively charged charginos, $\widetilde{\chi}_{1,2}^\pm$. The higgsinos also mix between themselves as $-1/2(-\mu)(\tilde{H}_u^0 \cdot \tilde{H}_d^0 + \tilde{H}_d^0 \cdot \tilde{H}_u^0) + h.c.$ where μ is introduced in the superpotential as a $SU(2)$ invariant coupling between the two Higgs doublets. The gluinos of the MSSM cannot mix with other sparticles due to their colour charge.

In the limit of the CMSSM, the gluino, bino and wino mass parameters are related roughly by $M_{gluino} : M_{bino} : M_{wino} \approx 6 : 2 : 1$, which implies that the gluinos are heavier than the neutralinos or charginos.

The scalar partners to the SM fermions (the squarks and sleptons) can in principle mix with each other since they have the same charges and R-parity values. In reality these mixing terms must be small due to experimental constraints discussed previously.

The masses of the first and second generations of squarks and sleptons are expected to be nearly degenerate due to small Yukawa couplings.

The Yukawa couplings between the neutral Higgs bosons and the third generation sfermions are of the form:

$$f_\tau = \frac{gm_\tau}{\sqrt{2}M_W \cos\beta},$$

(1.29)

which receives enhancements for large values of $\tan\beta$.

The mass squared term in the Lagrangian can be expressed as [32]:

$$\mathcal{L}_{\widetilde{\tau}} = -(\widetilde{\tau}_L^\dagger, \widetilde{\tau}_R^\dagger)\mathbf{m}_{\widetilde{\tau}}^2 \begin{pmatrix} \widetilde{\tau}_L \\ \widetilde{\tau}_R \end{pmatrix}, \quad \text{where} \quad \mathbf{m}_{\widetilde{\tau}}^2 = \begin{pmatrix} m_{L_3}^2 + \Delta_{\widetilde{e}_L} & m_\tau(A_0 - \mu\tan\beta) \\ m_\tau(A_0 - \mu\tan\beta) & m_{\widetilde{\tau}_R}^2 + m_\tau^2 + \Delta_{\widetilde{e}_R} \end{pmatrix}$$

(1.30)

with:

$$\Delta_{\widetilde{e}_L} = \left(-\frac{1}{2} + \sin^2\theta_W\right)m_Z^2\cos 2\beta$$

(1.31)

and

$$\Delta_{\widetilde{e}_R} = \frac{1}{3}\sin^2\theta_W m_Z^2\cos 2\beta.$$

(1.32)

The matrix $\mathbf{m}_{\widetilde{\tau}}^2$ may be diagonalised to mass eigenstates.

The degree of mixing in the $\widetilde{\tau}$ sector varies as a function of the magnitude of $\tan\beta$. For large values however, the mixing becomes significant and the mass of the $\widetilde{\tau}_1$ is lower than the masses of the first two families. Similar behaviour is expected for the stop and sbottom masses. For low values of $\tan\beta$, mixing is significantly reduced and the mass and gauge eigenstates approach degeneracy, with the mass of the $\widetilde{\tau}$ nearly degenerate with the mass of the first two slepton families.

1.3. SUSY Searches at the Large Hadron Collider

The LHC provides the necessary energy and luminosity to probe NP including SUSY. Typically, R-parity conserving SUSY signals can be characterised by the presence of hadronic activity and missing energy. The missing energy may be either measured directly in the case of a lepton collider, or in the case of a hadron collider, be measured in the transverse plane to the beam (E_T^{miss}). Additionally one can expect one or more leptons in the final state which may be exploited to reduce SM background.

Considering the large allowed parameter space of a given SUSY model, searches at the LHC should be as generic as possible and not focus on specific models.

The presence of at least two jets and E_T^{miss} is the strongest and most generic SUSY signal, allowing maximum coverage of the allowed parameter space. However significant SM background is also expected. Nevertheless, this broad search provides the most stringent probe for a CMSSM signal above the SM. Both the CMS and A Toroidal LHC ApparatuS (ATLAS) collaborations have published searches with jets and E_T^{miss} using different strategies for the combination of kinematic variables. An example of these may be found in [33, 34]. The most recent exclusion from the CMS collaboration in this channel is shown in figure 1.4.

Whilst jets and E_T^{miss} searches probe the broadest SUSY models, there are several motivations for tightening a SUSY search by adding one or more leptons to the final state [36]. Additional constraints may be applied via charge and flavour requirements.

The expected SM background in jets + E_T^{miss} searches is large at the LHC. The largest contribution to this comes from the general QCD environment of a hadron collider. Typically the E_T^{miss} originates from jet mismeasurements and calorimeter effects [37], however real E_T^{miss} may be produced in other SM processes like top quark and W-boson decay, or $Z \rightarrow$ *invisible*. These are typically estimated with combinations of kinematic variables to distinguish QCD from SUSY topology, and control samples to assess the contribution from SM events with real E_T^{miss}. Including one or more leptons in the final state significantly reduces the expected SM background.

In the event of observing an excess above SM expectations, the leptonic search channels may provide additional information about the mass spectrum of the SUSY particles [15]. In particular, decay chains producing two leptons in the final state provide a dilepton invariant mass distribution which may be used to extract SUSY mass measurements.
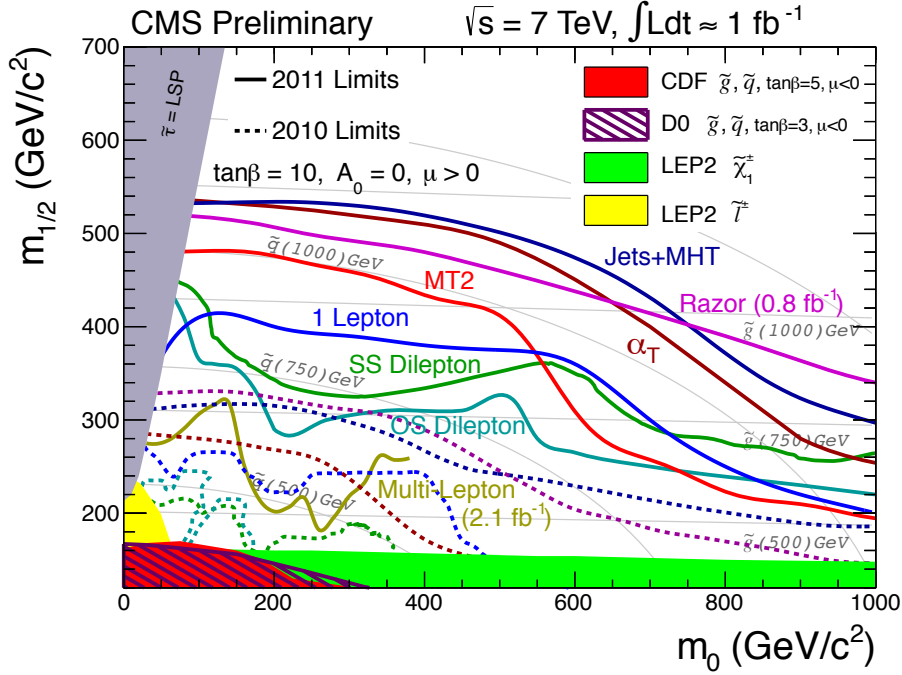
Figure 1.4.: 95% CL exclusion (observed and expected) in the CMSSM plane for CMS SUSY searches performed with 1 fb^{-1} of data. Taken from [35].

Finally, the leptonic searches are a handle for early SUSY discovery at the LHC due to the high signal to background ratio when compared to jets + E_T^{miss} for certain SUSY parameter points.

1.4. SUSY Dilepton Events at the Large Hadron Collider

As discussed above, there are several good motivations for including one or more leptons in the final state for a SUSY analysis. These can be broken into several combinations of charge and/or flavour requirements designed to probe different SUSY scenarios. The following discussion focuses on SUSY signals with SSDL [38, 39] in the final state with a particular emphasis on final states including τs as one of the reconstructed leptons.

1.4.1. Same–Sign Dilepton Events

SSDL SUSY events provide a clean signature with very little SM background compared to the jets + E_T^{miss} (+ 1 lepton or 2 opposite–sign leptons). SSDL can be produced from several processes in the MSSM and are expected to be produced in equal proportion to opposite–sign pairs since gluinos are expected to decay to positively or negatively charged leptons equally. SSDL are also expected to be readily produced in other NP scenarios – extra dimensions, heavy Majorana neutrinos [40–42] – extending the scope of searches in this final state to a wide range of potential NP scenarios. A Feynman diagram of a MSSM cascade producing SSDL in the final state is shown in figure 1.5. The SSDL channel also provides the possibility of deriving information about the masses of the sparticles in the decay by considering and combining only the measured final state lepton momenta [43].

Figure 1.5.: SSDL production from a SUSY cascade with associated E_T^{miss} originating primarily from the $\widetilde{\chi}^0$. The SUSY cascade starts with the production of gluinos which cascade to SM quarks. The charginos ($\widetilde{\chi}_1^+$) decay to neutralinos ($\widetilde{\chi}_1^0$) and SM W bosons which produce the E_T^{miss} and SSDL signature.

All six final states (ee, eμ, eτ, $\mu\mu$, $\mu\tau$, $\tau\tau$) are included in the CMS search for jets + E_T^{miss} + SSDL.

1.4.2. Enhancement of τ-leptons in the Final State

Due to the difficulties in reconstructing hadronically decaying τ, τ–jets are commonly ignored when considering final state leptons. However the possible enhancement of τ production in SUSY decays combined with the τ branching fraction to hadrons (65%) provides a possible scenario for early SUSY discovery via these channels.

Typically the mechanism for enhancement of τ in the final state is dependent on the considered SUSY model. Considering the MSSM described in section 1.2, an enhancement of $\widetilde{\chi}^{\pm}$ and $\widetilde{\chi}^0$ decays to τs is expected for large values of $\tan\beta$ due to the dependence of the Yukawa couplings and mass matrix on $\tan\beta$, as discussed in section 1.2.1. In addition to the effect of large $\tan\beta$ directly on the Yukawa coupling f_τ (equation 1.29) and mass mixing of the left and right handed $\widetilde{\tau}$, models with common scalar masses can have the third generation scalar masses lower than the first and second generation due to negative contributions of the Yukawa coupling to the RG equations governing the weak scale masses of $\widetilde{\tau}_{R,L}$ [44].

Further theoretical motivations exist for a τ enhancement in the expected final state of a SUSY decay at LHC such as a non–zero trilinear parameter in the CMSSM or minimal Super Gravity (mSUGRA) model [45], or SUSY seesaw models which suppress the mass of the left-handed $\widetilde{\tau}$ doublet [46].

The above discussion concludes the motivation for SSDL searches including hadronic τs as an important channel for SUSY and NP discovery at the LHC.

Chapter 2.

The LHC and CMS Detector

Located on the Franco–Swiss border, the LHC [8] is a 26.7 km circumference synchrotron proton–proton collider designed to probe the 1 TeV scale.

Four major experiments are located at various points on the LHC ring as shown in figure 2.1. ATLAS [47] and CMS [48] detectors are located at points 1 and 5 respectively and are complementary general purpose detectors designed for direct–detection NP discovery. This includes SM Higgs boson and SUSY/exotic physics searches.

Large Hadron Collider Beauty (LHCb) [49] (point 8) is a single–arm forward spectrometer designed to probe rare decays and make precision measurements of CP violation in B decays.

Point 2 is the location of A Large Ion Collider Experiment (ALICE) [50] – a dedicated detector for the purpose of studying lead ion collisions and the expected quark–gluon plasma produced.

2.1. The Large Hadron Collider

The LHC was installed in the existing tunnel that formerly housed the LEP, situated between 45 m and 170 m underground. It is designed to run at a nominal $\sqrt{s} = 14$ TeV centre of mass energy at $\mathcal{L} = 10^{34}$ cm^{-2} s^{-1}, colliding bunches of $\mathcal{O}(10^{11})$ protons at 40 MHz. The choice of nominal energy and luminosity specification constrains the design of the LHC. The beam intensity removes the option of a common vacuum and magnet system similar to that of the Tevatron p$\bar{\text{p}}$ collider. Instead, the counter–rotating proton beams require separate magnet fields and vacuums. To achieve this performance, protons

are accelerated and bunched by the accelerator complex [51] prior to their injection into the LHC.

The protons, produced by stripping the electron from hydrogen atoms, are first accelerated in the Linear Accelerator 2 (LINAC2) up to 50 MeV at which point they are injected into the Proton Synchrotron Booster (PSB) to be accelerated to 1.4 GeV. The Proton Synchrotron (PS) provides acceleration to 26 GeV and also sets the bunch structure and spacing. They are then injected to the Super Proton Synchrotron (SPS) which accelerates them to 450 GeV before being injected into the main LHC ring via transfer lines TI 2 and TI 8. The layout of the accelerator chain and position of LHC experiments is shown in figure 2.1.
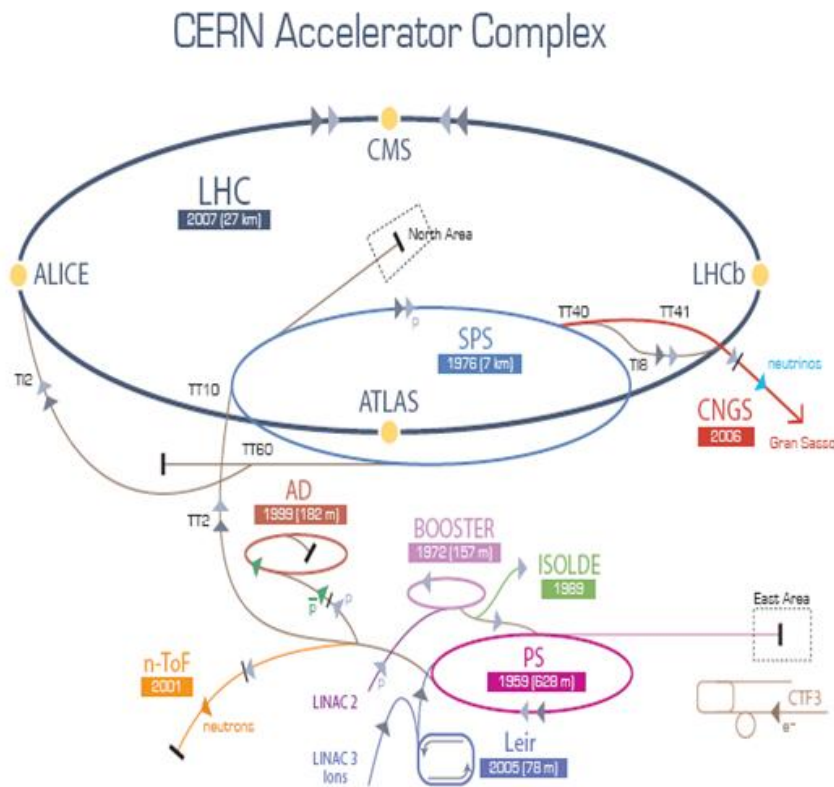
Figure 2.1.: CERN accelerator complex showing the main LHC ring with associated experiments and the various stages of injector accelerators. Taken from [52].

The LHC was due to start producing collisions in 2008 at 14 TeV. Unfortunately this was delayed due to a compromised connection between two of the LHC dipole magnets which caused a crack and consequent helium leak following a magnet quench [53]. The damage was significant and delayed the machine startup date by about a year. Following

the initial test runs of circulating beams in November 2009, the first high energy collisions were produced in March 2010 albeit at half the design centre of mass energy.

The LHC delivered around 5.6 fb^{-1} to the ATLAS and CMS experiments by the end of the 2011 run as shown on a log scale in figure 2.2a. The evolution of instantaneous luminosity throughout this period is shown in figure 2.2b.

The main analysis presented in this thesis was performed on the first 976 pb^{-1} of 7 TeV data collected at CMS in the 2011 run. The evolution of data collection up to 1 fb^{-1} at CMS is shown in figure 2.2c.

2.2. The Compact Muon Solenoid Detector

CMS is a general purpose detector of overall dimensions 21.6 m length, 14.6 m diameter for a weight of 12500 tonnes [56]. The primary goal of CMS is to explore physics at the 1 TeV scale, which includes SM Higgs Boson searches as well as probing NP. These necessitate a hermetic design focused around a strong magnetic field with high momentum and energy resolution of muons and charged particles. The detector comprises a high granularity silicon tracker and electromagnetic and hadronic calorimetry within a 4 T superconducting solenoid. Muon chambers are located on the outside of the magnet. CMS uses a coordinate system with the origin located at the nominal interaction point. The y-axis points vertically upward with the x-axis pointing towards the centre of the LHC and the z-axis pointing along the direction of the beam. Azimuth ϕ is measured with respect to the x-axis. Pseudorapidity is defined in the usual manner, $\eta = -\ln\tan(\theta/2)$, where polar angle θ is measured from the z-axis. The variable $\Delta R = \sqrt{\Delta\phi^2 + \Delta\eta^2}$ is commonly used to define angular distance within the detector. As momentum and energy are conserved in the transverse plane with respect to the beam pipe, the transverse projection of energy and momentum quantities are commonly used in CMS analyses. They are written as E$_T$ and p$_T$ respectively throughout.

2.2.1. Superconducting Solenoid Magnet

A 12.5 m long, 6 m inner diameter superconducting solenoid is used to achieve the high magnetic field required by the desired muon momentum resolution ($\frac{\Delta p}{p} = 10\%$ at p$_\mu$ = 1 TeV). The magnet is designed to deliver a nominal 4 T magnetic field, with a
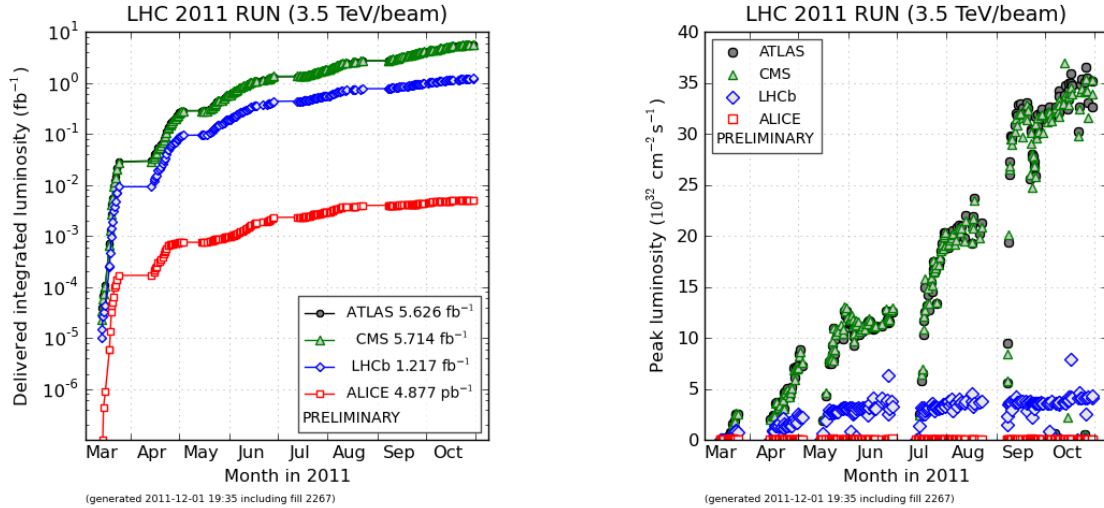
(a) Collected luminosity in 2011 shown on a log scale.

(b) Evolution of instantaneous luminosity in 2011.
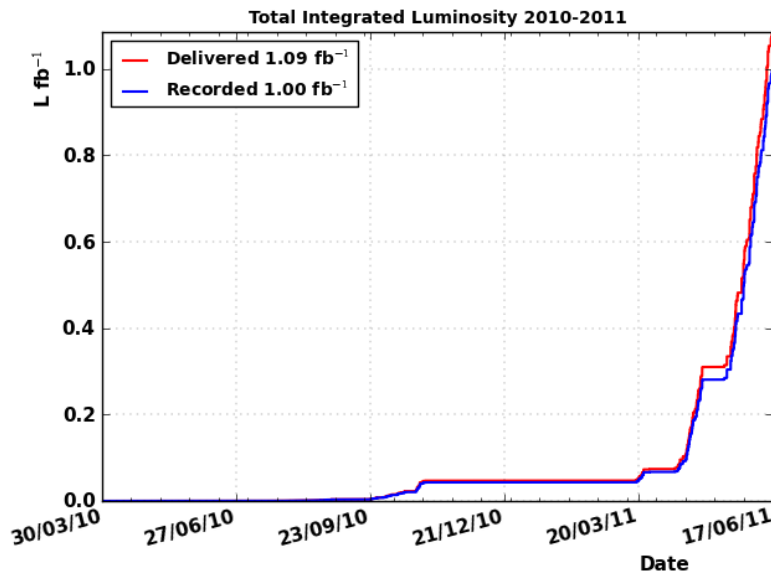
(c) The first ~ 1 fb^{-1} of data recorded at CMS and analysed in this thesis.

Figure 2.2.: Evolution of the integrated luminosity delivered by the LHC to the four primary experiments and the evolution of instantaneous luminosity (figures 2.2a and 2.2b). The integrated luminosity evolution up to 1 pb^{-1} delivered to CMS is shown in 2.2c. Taken from [54, 55].

current operational field of 3.8 T. The inner magnet volume contains the tracking and calorimetry hardware, with four muon chambers interleaved with the iron return yoke.

Very-forward
Calorimeter

Superconducting Solenoid

Silicon Tracker

Pixel Detector

Preshower

Hadronic
Calorimeter

Electromagnetic
Calorimeter

Muon
Detectors

Compact Muon Solenoid
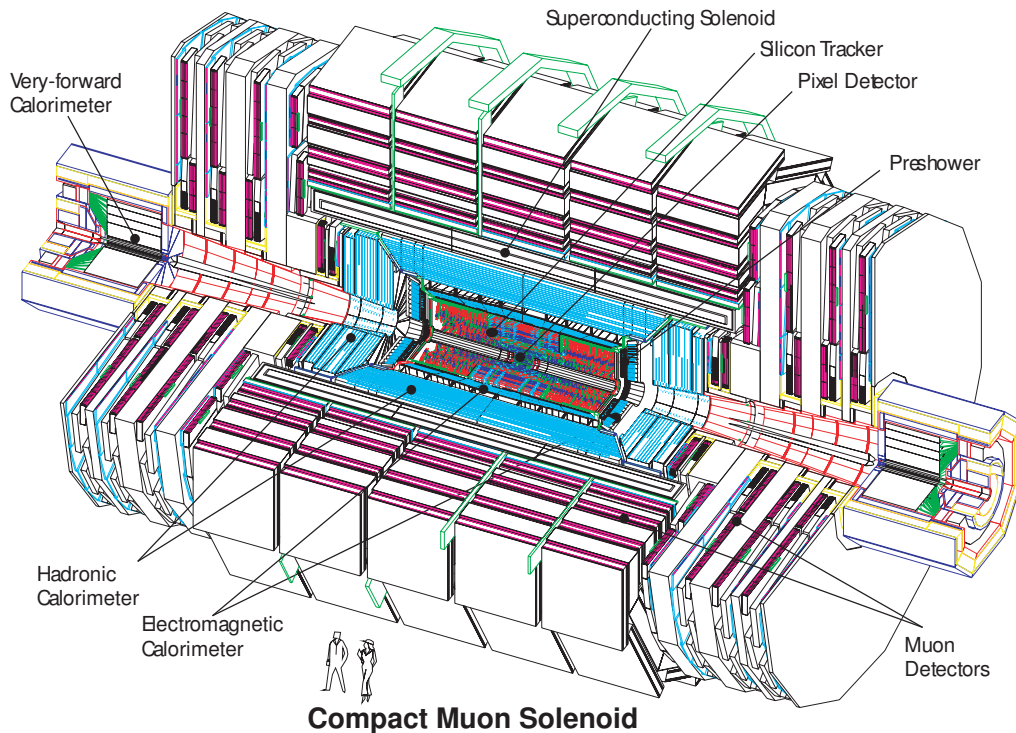
Figure 2.3.: Illustration of the CMS detector layout. Taken from [57].

The coil of the magnet is arranged in four layer windings of Niobium-Titanium (NbTi) conductor to achieve the necessary number of ampere-turns required for a 4 T magnetic field. The conductor uses Al as the insert and Al alloy for mechanical reinforcement [58]. Due to the high stored energy (2.6 GJ) and E/M ratio (11.6 kJ/kg), the CMS coil needs significant structural integrity. Due to this design constraint the CMS magnet includes structural support within the conductor itself, thereby supporting the hoop stress over the coil layers and the outer support structure rather than relying solely on the outer structure.

The return yoke section comprises six disks in the endcaps and five wheels in the barrel sections of the detector. These are mounted on a system of air and grease pads which allow precision alignment (2 mm) using a 70 point reference system in the detector hall with respect to the centre of the magnet coil.

The field inside and outside the coil has been extensively mapped. The inner coil volume was mapped to a precision of 0.07% and found to be in excellent agreement with simulation before lowering into the experiment cavern using a fieldmapper [59] for B= 2, 3, 3.5, 3.8 and 4.0 T over 33840 points inside a cylinder of radium 1.724 m and length 7 m. The mapping of the field in the barrel return yoke was found to be accurate

to 3% and 8% in the first three and last two wheels respectively using cosmic muon events [60].

2.2.2. Inner Tracking System

The CMS tracking system is split into two sections as a function of radius. From the interaction point to $r = 20$ cm where particle flux is at its highest (10^7 at $r = 10$ cm), 100×150 µm^2 silicon pixels are used, giving an occupancy of order 10^{-4} per pixel per LHC crossing at nominal operation values. The particle flux drops enough in the region immediately following the pixel tracker ($20 < r < 55$ cm) to enable the use of silicon microstrips (10 cm $\times$ 80 µm). The outermost region has sufficiently low particle flux to enable the use of microstrips with a cell size of 25 cm $\times$ 180 µm.

The total tracking subdetector is 5.5 m long and 2.4 m in diameter. It comprises 15148 modules with 9.3×10^6 channels.

Silicon Pixel Tracker

The silicon pixel detector is made up of three barrel layers located at $r = 4.4$ cm, $r = 7.3$ cm and $r = 10.2$ cm and two endcap disks located at $z = \pm 34.5$ cm and $z = \pm 46.5$ cm as shown in figure 2.4. This covers a range of $|\eta| < 2.5$.

This provides accurate tracking in $r - \phi$ and z which allows 3D vertex reconstruction, small impact parameter resolution and good secondary vertex identification.

The pixel tracker has a resolution of around 10 µm and 20 µm in $r - \phi$ and z respectively.

Silicon Strip Tracker

The silicon strip layout of the tracker in the $r - z$ plane is shown in figure 2.5. It is composed of a Tracker Inner Barrel (TIB) and a Tracker Outer Barrel (TOB) which are described below.

The TIB is composed of four layers of 320 µm micro-strip silicon detectors orientated parallel to the beam axis up to $|z| < 65$ cm and out to a radius of 55 cm. The TIB is complemented by three disks of silicon micro-strips arranged radially to the beam line
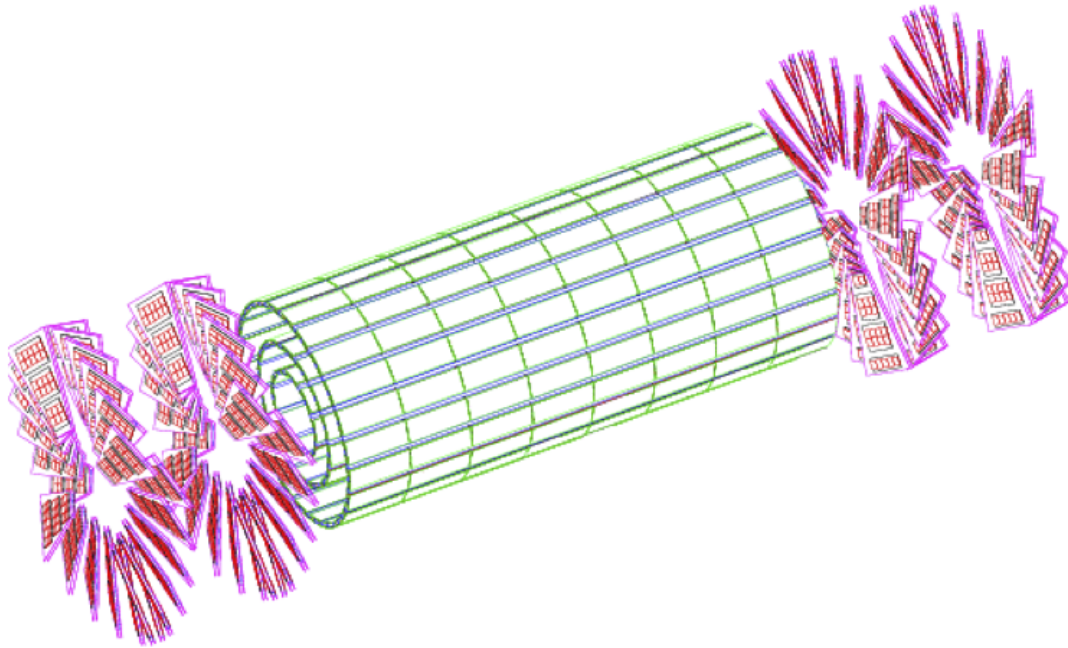
Figure 2.4.: The CMS pixel tracker configuration showing three barrel layers and two endcap disks. Taken from [61].
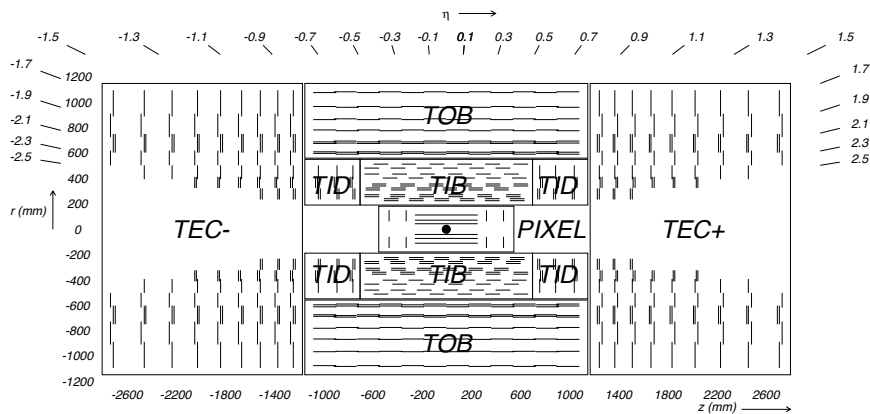
Figure 2.5.: CMS silicon strip tracker layout. Single lines show individual strip modules. Stereo modules are shown by double lines. Taken from [56].

at either end which make up the Tracker Inner Disk (TID). The strips in the TIB have an average pitch of 100 µm providing four measurements in $r - \phi$ with approximately 30 µm resolution for a single tracker hit.

The TOB uses six layers of 500 µm thick silicon strips with a pitch of $122 - 183$ µm, out to a radius of 116 cm and $|z| = 118$ cm. This provides six measurements in $r - \phi$ with

a resolution of approximately 45 μm. These are completed on either side by the Tracker End Caps (TECs) which are made up of nine disks covering the 124 cm $< |z| <$ 282 cm and 22.5 cm $< |r| <$ 113.5 cm region.

The CMS tracker provides stereo resolution in the first two layers/rings of the TIB, TID and TOB, and rings 1, 2 and 5 of TECs. This is achieved by mounting a second silicon microstrip back-to-back with the first, with a stereo angle of 100 mrad. This provides a simultaneous measurement of the complimentary coordinate in the respective part of the tracker (z in the barrel section and r in the disks).

Basic track reconstruction is performed using a Combinatorial Track Finder (CTF) algorithm which implements a Kalman Filter (KF) to assign hits to the track trajectory as well as establish the track parameters. The tracker performance was tested with the first ~ 10 nb^{-1} at $\sqrt{s} = 7$ TeV. Excellent agreement between simulation and data was found with primary vertex efficiency around 100% for vertices with ≥ 2 tracks with $p_T > 0.5$ GeV. The resolution of the Primary Vertex (PV) is found to be $20 - 30$ μm in the x, y and z directions for ≥ 20 tracks as shown in figure 2.6 [62].

(a) PV resolution in x **(b)** PV resolution in y **(c)** PV resolution in z
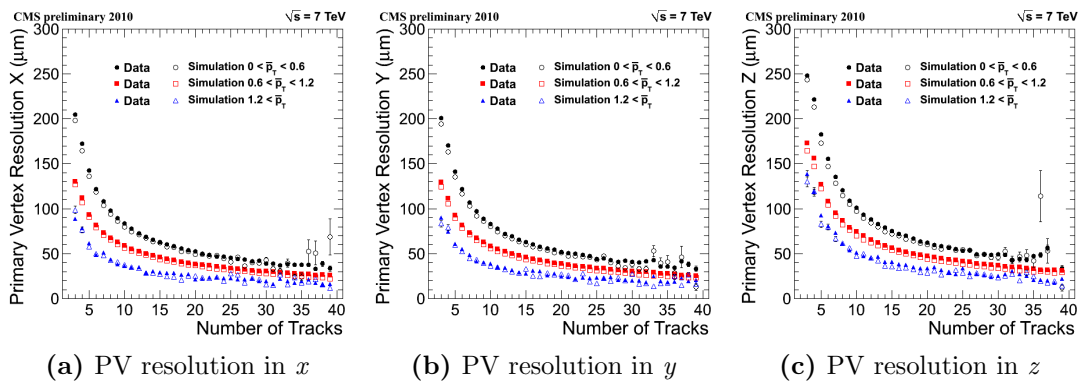
Figure 2.6.: Primary vertex resolution in x, y and z as a function of number of reconstructed tracks shown for three different average track p_T ($0 < \bar{p}_T < 0.6$ GeV, $0.6 < \bar{p}_T < 1.2$ GeV and $\bar{p}_T < 1.2$ GeV). Comparison with simulation is also shown. Taken from [62].

The tracker efficiency, p_T resolution and impact parameter resolution were measured from simulation for single muon tracks. Muon efficiency was found to be greater than 98% up to $|\eta| < 2.2$.

(a) Track reconstruction efficiency.

(b) Track resolution.

(c) Track impact parameter resolution.
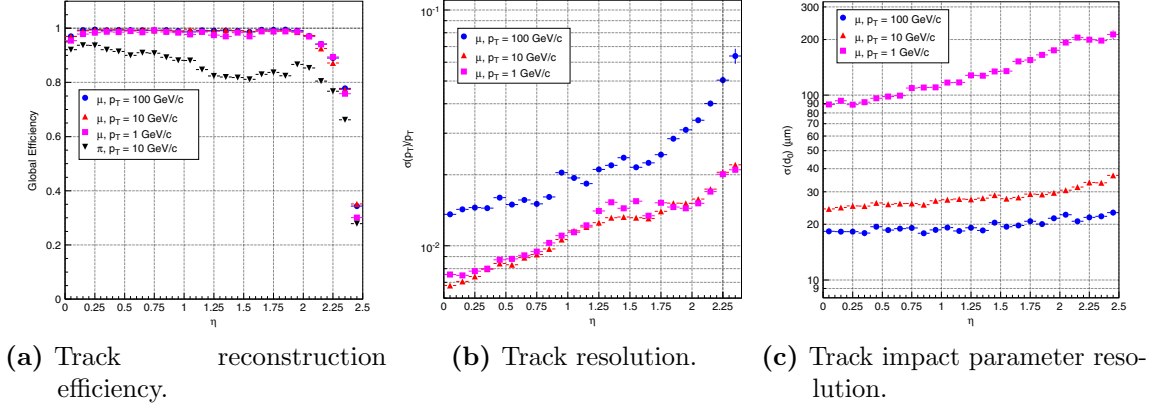
Figure 2.7.: Efficiency, impact parameter resolution and p_T resolution for single track muons. Track reconstruction efficiency is also shown for $p_T = 10$ GeV pions. Taken from [63].

2.2.3. Calorimetry

Electromagnetic Calorimeter

The CMS Electromagnetic Calorimeter (ECAL) is a homogeneous calorimeter comprised of 61200 (7324) lead tungstate (PbWO$_4$) crystals in the barrel (each endcap). This is complemented with a preshower detector in front of the endcap crystals ($1.65 < |\eta| < 2.6$). Scintillation in the crystals is detected and amplified by Avalanche Photodiodes (APDs) and Vacuum Phototriodes (VPTs) in the barrel and endcaps respectively.

The choice of crystal is motivated by the operating conditions of the LHC. The lead tungstate crystals provide a short radiation length ($\chi_0 = 0.89$ cm) and small Molière radius (2.2 cm). Additionally 80% of their light is emitted within 25 ns – the nominal bunch crossing time of the LHC. This provides a fast, high granularity response. The light output of the crystals is relatively low and temperature dependent ~ 4.5 photoelectrons/MeV at 18 °C. The scintillation light is detected by the APDs and VPTs designed specifically for the CMS ECAL in the barrel and endcaps respectively. Each APD was tested to ensure radiation hardness and longevity over ten years of LHC running. The crystals and APDs response are both sensitive to temperature. As a result, the ECAL is carefully maintained at 18 ± 0.05 °C by water cooling.

The ECAL may be considered in two sections as illustrated in figure 2.8. The barrel section (EB) covers the range of $0 < |\eta| < 1.479$. The crystals in this section have a cross-section of $\sim 0.0174 \times 0.0174$ (varies slightly with η) in $\eta - \phi$, with a length of
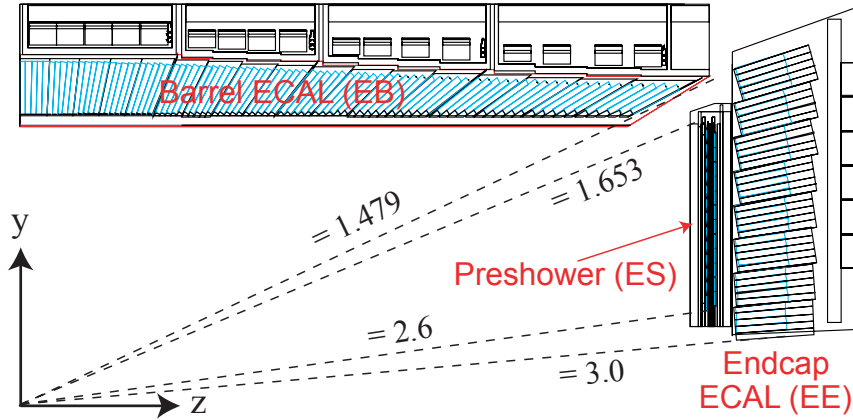
Figure 2.8.: A schematic of one quadrant of the CMS ECAL. Taken from [61].

230 mm (25.9 X_0). They are arranged at 3° in ϕ and η with respect to the line to the nominal interaction vertex to avoid particle trajectories being aligned with the cracks between adjacent crystals. Structurally, the crystals are arranged in submodules which themselves are arranged into modules containing around 400–500 crystals depending on η. These are then assembled in groups of four into supermodules.

The endcaps (EE) cover the range $1.479 < |\eta| < 3.0$. Here the crystals are grouped in 5×5 supercrystals. These are arranged with angles between 2° and 8° with respect to the interaction point. The crystals in this section of the ECAL have a cross-section of 30×30 mm^2 at the rear and 28.62×28.62 mm^2 at the front, with a length of 220 mm (24.7 X_0).

An Electromagnetic Preshower (ES) sampling calorimeter detector is contained within the ECAL in the region $1.653 < |\eta| < 2.6$ which helps identify π^0 and distinguish electrons from Minimum Ionising Particles (MIPs). The ES is composed of two layers of lead to induce an electromagnetic shower from e/γ with silicon strips to measure the profile and energy deposit.

The energy resolution of the ECAL can be described as:

$$\left(\frac{\sigma}{E}\right)^2 = \left(\frac{S}{\sqrt{E}}\right)^2 + \left(\frac{N}{E}\right)^2 + C^2, \tag{2.1}$$

where the C is the constant term, N the noise term and S the stochastic term. Figure 2.9 shows the ECAL resolution as a function of electron energy taken with a test beam. The C, N and S parameters are shown.
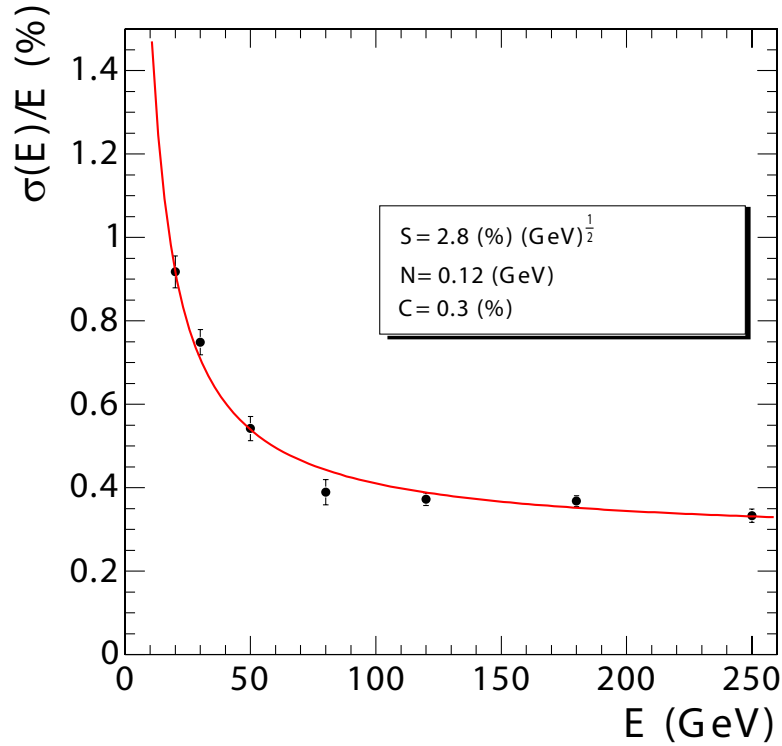
Figure 2.9.: Error function of ECAL with energy measured in 3×3 crystal arrays. Taken from [56].

Hadronic Calorimeter

The CMS Hadronic Calorimeter (HCAL) sampling calorimeter is designed to provide hermetic coverage and good containment for precise E_T^{miss} measurements. A schematic of one quadrant of the HCAL is shown in figure 2.10.

The barrel section (HB) of the HCAL is contained between the outer edge of the ECAL and the inner edge of the magnet coil. It comprises 2304 towers covering $|\eta| < 1.3$ and azimuth $0 < \phi < 2\pi$ with a segmentation $\Delta\eta \times \Delta\phi = 0.087 \times 0.087$ in the plastic scintillators.

The HB is constructed from brass plates arranged parallel to the beam axis and arranged in 36 wedges in azimuth ϕ, split between two half–barrel segments. This absorber plate structure is sandwiched with steel plates for strength. In total this comprises one 40 mm thick front steel plate, eight 50.5 mm thick brass plates, six 56.5 mm thick brass plates and finally a 75 mm steel back plate. This provides a thickness of 5.82 λ_l (interaction lengths) at $\eta = 0$ which increases with θ as $1/\sin\theta$ (10.6 λ_l at maximum $|\eta|$). The
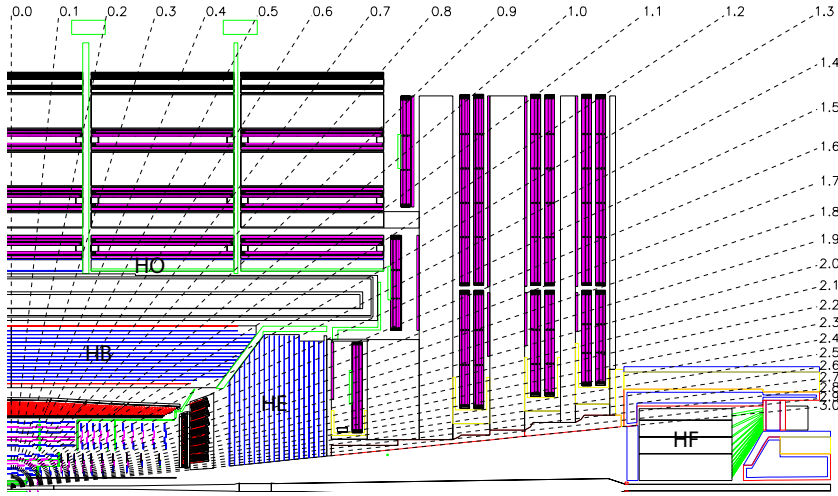
Figure 2.10.: A schematic of one quadrant of the CMS HCAL showing the barrel (HB), outer (HO), endcap (HE) and forward (HF) regions. Taken from [56].

absorbers are interleaved with the plastic scintillators. The first 9 mm layer of scintillating material sits before the first steel plate to sample showers which develop between the end of the ECAL and the start of the HB. The next 15 layers are each 3.7 mm thick. The final layer sits outside the steel back plate and is 9 mm thick to correct for showers leaking from the HB.

The HCAL is completed with endcaps (HE) comprised of 2304 towers covering $1.3 < |\eta| < 3.0$. The ϕ and η segmentation varies over the covered η range. The five outer towers (smallest η) have an $\eta - \phi$ segmentation of 0.087 rad each. The eight innermost towers have a ϕ segmentation of 0.87 rad with η varying from 0.09 to 0.35.

The outer hadron detector (HO) is composed of 10 mm thick scintillator tiles covering the region $|\eta| < 1.3$. These are positioned outside the solenoid, increasing the total number of interaction lengths in the HCAL to greater than ten. They are positioned to approximately map the tower granularity ($\Delta\eta \times \Delta\phi = 0.087 \times 0.087$) of the HB. This allows measurement of jets which escape the HB thus reducing non–Gaussian tails in the hadronic energy resolution.

Finally, there is a very forward section (HF) ($3 < |\eta| < 5$) of the CMS HCAL. This section is subject to significant particle fluxes and radiation which constrains the HF design. Consequently, the active medium is quartz fibres which generate a signal via Cherenkov light. These are inserted at two depths in the steel absorber structure – at full depth (165 cm $\sim 10\lambda_l$) and at 22 cm. Due to the choice of active medium, the HF is

primarily sensitive to the electromagnetic component of hadron showers. Reading out the energy deposits near the front and back of the absorber helps distinguish showers from e/γ which deposit most of their energy in the first set of fibres from hadronic showers which produce equal deposits in both fibre sections.

The E_T resolution in three different η regions corresponding to the HCAL subsections described above is shown in figure 2.11.
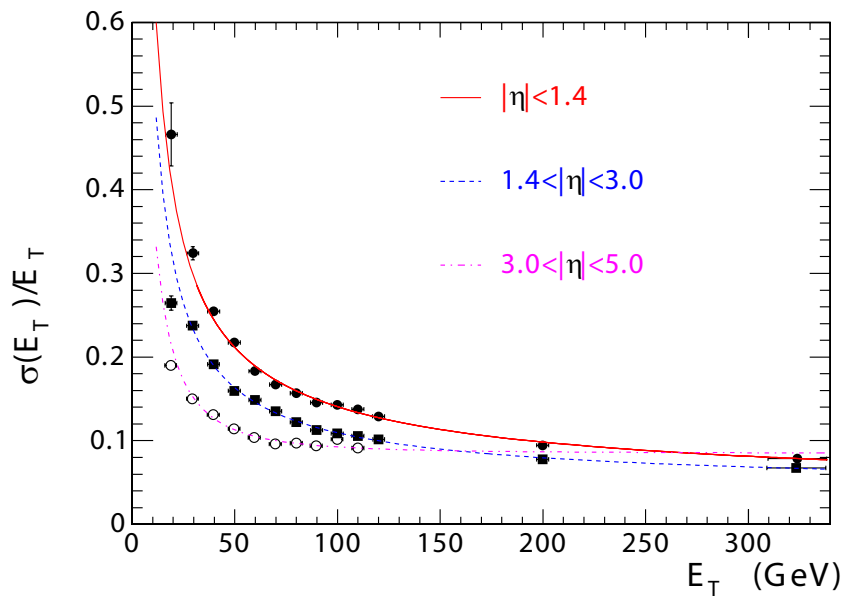
Figure 2.11.: HCAL jet E_T resolution as a function of jet E_T, for jets in the barrel ($|\eta| < 1.4$), endcaps ($1.4 < |\eta| < 3.0$) and forward ($3.0 < |\eta| < 5.0$) regions. Taken from [56].

2.2.4. Muon System

The muon system is a central feature of the CMS detector. The dedicated muon chambers sit outside the magnet coil, interleaved with the magnet's return yoke. Full muon reconstruction relies on measurements made in the inner tracker (see Section 2.2.2 for description), in the muon chambers situated after the magnet coil, and in the return yoke.

Three types of gaseous detector are used in the muon system. The barrel region ($|\eta| < 1.2$) relies on Drift Tubes (DTs), whilst the endcaps employ Cathode Strip Chambers (CSCs) due to the higher rate of muons, neutron background and the higher magnetic field. These cover a region of $0.9 < |\eta| < 2.4$. Finally, Resistive Plate Chambers (RPCs)

complete the muon chambers and cover the barrel and endcap regions. The arrangement of these subsystems is shown in figure 2.12.
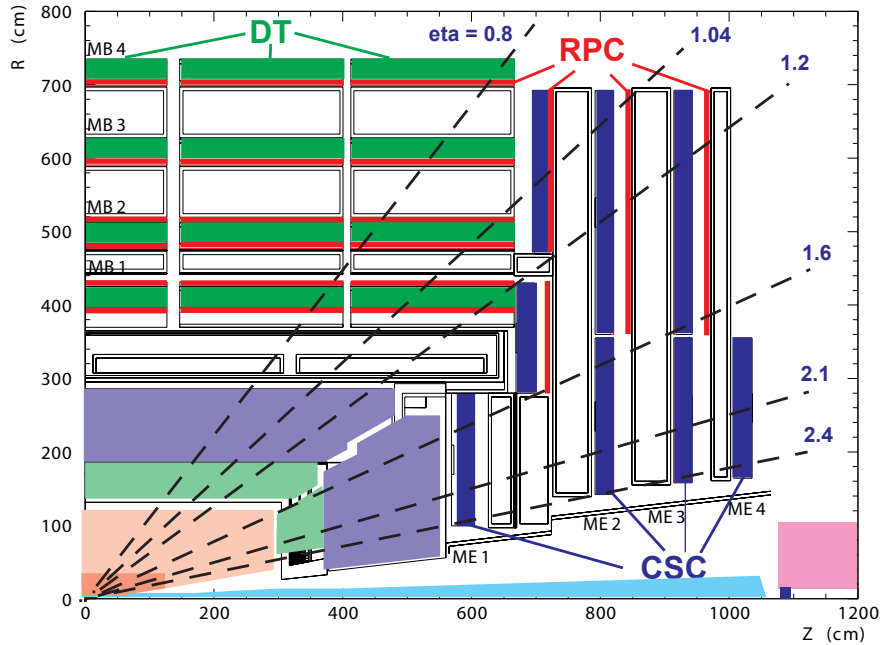
Figure 2.12.: A schematic of one quadrant of the muon chamber system showing the DTs, CSCs and RPCs. Taken from [61].

The barrel region of the muon system is arranged into five wheels. These in turn are split into sectors covering an azimuth of 30° each. Each wheel is arranged in four muon stations. The three innermost stations consist of 2×4 chambers each which provide a $r - \phi$ measurement and four more chambers which resolve the muon z coordinate. The final station only provides $r - \phi$ measurements. Considering the four muon stations as concentric cylinders around the direction of the beam, the first three consist of 60 DTs each whilst the final outer section comprises 70 DTs. These are complimented by ~ 172000 wires.

The endcap region of the muon system consists of 468 CSC – multiwire proportional chambers with six anode wire planes interleaved with seven cathode panels. The wires are arranged azimuthally and measure the muon track's r coordinate. The strips run at constant ϕ. The muon coordinate in ϕ is inferred by interpolation of the charges induced on the strips and the wires.

The RPCs, gaseous parallel-plate detectors, provide very fast (< 25 ns) ionisation tagging time. This allows muon triggering to identify clearly which Bunch Crossing (BX) a muon

is associated with. The RPC chambers are embedded in the magnet return yoke. Two are situated in the first two muon stations and one in each of the last two stations. This provides a muon measurement with at least four layers including muons which may stop before the final stations.

The DT and CSC provide a system to trigger on muon p_T which may be combined with the RPCs for a fast and independent triggering helping to resolve track ambiguities.

As shown in figure 2.13, up to $p_\mu \approx 200$ GeV the muon momentum resolution for the standalone system (excluding inner tracker) is around 9%. This increases to around 15%–40% at $p_T \approx 1$ TeV. When combined with the inner tracker (section 2.2.2), this is reduced to $\sim 5\%$ at $p_\mu = 1$ TeV – a factor of two improvement over the desired resolution motivating the magnet specification (section 2.2.1).
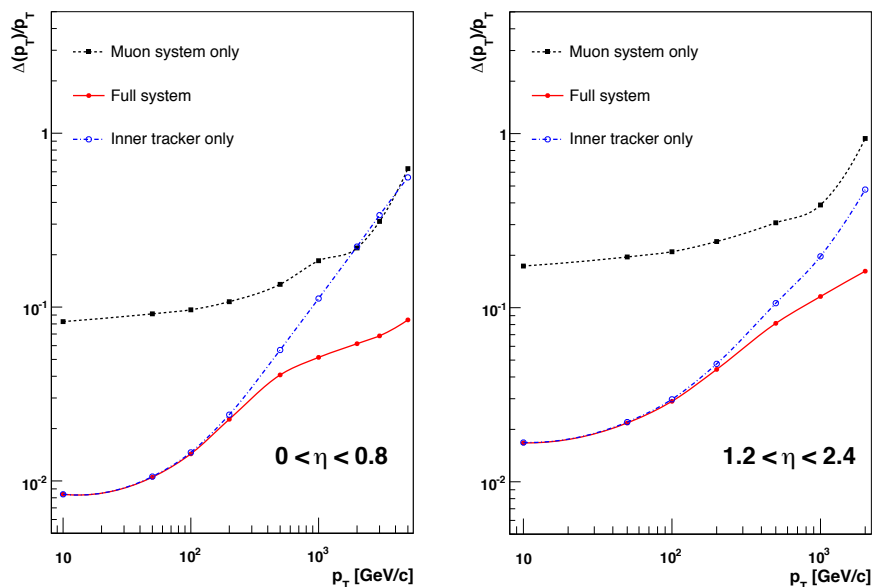
Figure 2.13.: Muon momentum resolution as a function of p_T, shown for three reconstruction regimes. Taken from [56].

2.2.5. Triggering

The nominal rate of LHC crossings is 40 MHz which must be reduced to ~ 100 Hz to be written to disk.

This is performed in two stages. A Level 1 Trigger (L1) implemented in hardware reduces the rate to 100 kHz which is further reduced[1] to $\sim$ 100 Hz by the software High Level Trigger (HLT).

Level 1 Trigger

The Level 1 Trigger (L1) uses information from the calorimeters and the muon chambers to reduce the rate to around 100 kHz. The L1 is implemented in custom hardware, using Field Programmable Gate Arrays (FPGAs) where possible and Application-Specific Integrated Circuits (ASICs) or Look Up Tables (LUTs) where necessary.

The L1 trigger can be broken into three components: local, regional and global. Calorimeter and muon triggers may be considered separately up to the Global Trigger (GT) decision made after the global trigger. Local triggers (Trigger Primitive Generators (TPG)) are taken from calorimeter deposits, and track segment/hits in the muon chambers. Specifically, the calorimeters are divided into trigger towers of $(\eta, \phi) = 0.0.87 \times 0.087$ up to $|\eta| < 1.74$ (larger beyond $|\eta| > 1.74$) where the trigger tower E_T is obtained from the energies in the ECAL crystals and HCAL towers. The information from the TPGs is then passed to the Regional Calorimeter Trigger (RCT) via serial links.

The RCT establishes e/γ candidates and $\sum E_T$ for each 4×4 trigger tower region (1×1 in the Hadronic Calorimeter (Forward) (HF)). The RCT also determines relevant isolation and MIP properties for muons, and τ–veto bits for identification of one and three prong τ decays.

Finally the Global Calorimeter Trigger (GCT) establishes jets, total $\sum E_T$, E_T^{miss}, number of jets and $H_T = \sum E_T$ for jets above a given threshold. Additionally the GCT forwards relevant muon information from the RCT to the Global Muon Trigger (GMT).

The L1 muon triggers receive contributions from all parts of the muon sub-systems (see section 2.2.4). The local trigger information is provided by barrel DT and (endcap) CSCs which deliver track and hit information. The Regional Muon Trigger (RMT) performs basic track finding from the DT and CSC track finders and this is combined with the RPC dedicated trigger detectors. Finally the GMT combines information across the three muon sub-systems with additional isolation and MIP information from the GCT.

---

[1]The HLT in fact currently outputs around 500 Hz.

The final accept/reject decision of the L1 is performed by the GT based on combined information of the objects provided by the GCT and GMT (e/γ, muons, jets, τ–jets, E_T, E_T^{miss} and H_T).

HLT

The CMS HLT [64] performs a partial reconstruction to determine whether to accept or reject the event. Although the trigger is implemented entirely in software, accept/reject decisions for a given event are performed at various stages of individual object reconstruction. This reduces Central Processing Unit (CPU) usage. To achieve this, the HLT performs its reconstruction and selection in roughly two steps.

Firstly information from the calorimeters and muon system is used to reduce the overall rate of events being processed. Tracking information is then used for events that pass this stage. Intermediate stages can occur between these which exploit part of the tracking information without reconstructing a full track. Electron/γ HLT identification illustrates this process. A 'e/γ' object is identified in the first instance using only calorimeter information. Following this, a requirement for hits in the silicon pixel tracker matching the ECAL deposit categorises the object as an electron or photon candidate. Finally, in the case of electron selection, a full track reconstruction seeded from the pixel hits is performed.

The HLT allows triggering on any basic physics object at CMS. In addition complex 'cross–triggers' which require more than one of these objects may be implemented.

In order to lower the output rate of the HLT for control and monitor triggers, a prescale factor may be applied such that the trigger output event rate is reduced by a factor of $\frac{1}{\text{prescale}}$.

Chapter 3.

Object Reconstruction and Performance with the CMS Detector

The SSDL analysis uses all reconstructed objects at CMS (excluding photons). The following sections describe physics object reconstruction and performance with the CMS detector relevant to the SSDL SUSY analysis.

3.1. Particle Flow at CMS – Jets and $\mathbf{E}_T^{miss}$

Particle Flow (PF) is a technique used in CMS to allow full reconstruction based on identifying all stable final state particles in an event. The following describes the broad features of the algorithm. A detailed description may be found in [65, 66].

PF combines components from all the subdetectors to determine which final state particles are present in the event. Generally, any particle is expected to produce some combination of a track in the silicon tracker, a deposit in the calorimeters, and a track in the muon system.

Iterative tracking is used to achieve highly efficient tracking with low fake rate which allows accurate measurement of momentum and direction of any charged particle (including hadrons) from the primary vertex. This procedure starts with a very tightly seeded track designed to minimise the fake rate. The following two steps increase the efficiency of the tracking by removing tracker hits identified in the previous step and reseeding the

tracks with a looser selection. Finally, the impact parameter constraint is relaxed to allow reconstruction of long lived particles and secondary charged particles. This process provides an efficiency of 99.5% for isolated muons and greater than 90% for charged hadrons after the first three steps and a fake rate of less than 1% after the full iteration.

Energy deposits in the various components of the calorimeters described in section 2.2.3 are clustered using an algorithm specific to PF reconstruction. The clustering starts with the identification of calorimeter–cell energy maxima above a given threshold in the calorimeter. These are then increased in size to form 'topological clusters' by including adjacent cells above a given threshold [66].

Tracks and energy deposits are combined using a linking algorithm which identifies individual particles and removes double counts and ambiguities. The linking starts by producing blocks of elements from any pair (track–calorimeter cluster). Links may also be established between calorimeter clusters in the HCAL and ECAL or the ECAL and ES. Finally links corresponding to muons in the tracker and muon chambers are made by establishing a global χ^2 fit over both tracks.

The PF algorithm runs over the blocks defined by the linking algorithm. Initially the muons are identified as PF muons and the tracks removed from the block if the global track momentum is consistent (3σ) with the silicon track momentum. Next, the electrons are identified and are also removed from the block.

The remaining tracks may be associated with some combination of ECAL and/or HCAL clusters. Neutral particles are identified using a comparison of track momentum and energy deposits in the calorimeters to first remove the charged particles. In the case where several tracks are linked to the same cluster, the sum of their momentum is compared to the energy deposit. If on the other hand one track is linked to several clusters, the link to the closest cluster is kept. When considering the ECAL, any additional clusters may occur from hadronic shower deposits or from overlapping photons. In this case, care is taken to avoid double counting or conversely missing the photon. Following this process, PF charged hadrons are formed for each of the remaining tracks, whilst unlinked calorimeter clusters are identified as PF photons or neutral hadrons for the ECAL and HCAL respectively.

E_T^{miss}– the missing transverse energy in the event – is exploited at CMS for the detection of weakly interacting particles and provides a key component of many NP searches. PF computes the E_T^{miss} of the event as the negative vector sum of the $\vec{p_T}$ of all particles reconstructed in the process described above. The computation of E_T^{miss} is particularly

sensitive to the calibration and offline noise cleaning of the calorimeters. The terms E_T^{miss} and Missing Transverse Energy (MET) are used interchangeably.

The PF algorithm is used to reconstruct the jet and missing energy quantities for the SSDL analysis. Jets are reconstructed from PF particles using the Anti-K$_T$ (AK) [67] jet clustering algorithm with a cone size of $\Delta R = 0.5$.

The AK algorithm clusters jets by defining a distance between hard (high p$_T$) and soft particles such that soft particles are clustered with hard particles before being clustered between themselves. This produces jets which are defined and altered by the presence of hard particles but are robust to soft particle radiation.

The expected performance of the PF algorithm for jet p$_T$ resolution and E_T^{miss} compared to 'standard' calorimeter jet reconstruction and Jet Plus Track (JPT) (described in [69]) is shown in MC in figures 3.1 and 3.2.

Commissioning of the PF algorithm was performed with 2009 $\sqrt{s} = 900$ GeV minimum bias LHC data [66] and 2010 $\sqrt{s} = 7$ TeV minimum bias data [70]. A very good agreement between simulation and data (figure 3.3) provides confidence in the expected improvements shown in MC for PF performance when compared to standard calorimetric jet reconstruction.

Jets are corrected with several Jet Energy Scale (JES) corrections. The L1 FastJet correction adjusts for additional jet energy originating from Pile Up (PU). L2 relative and L3 absolute corrections are applied based on dijet and γ + jets events to provide uniform jet response in η and p$_T$ respectively [71].

(a) $0 < |\eta| < 0.5$.

(b) $1 < |\eta| < 1.5$.

(c) $2 < |\eta| < 2.5$.

(d) $4 < |\eta| < 4.5$.
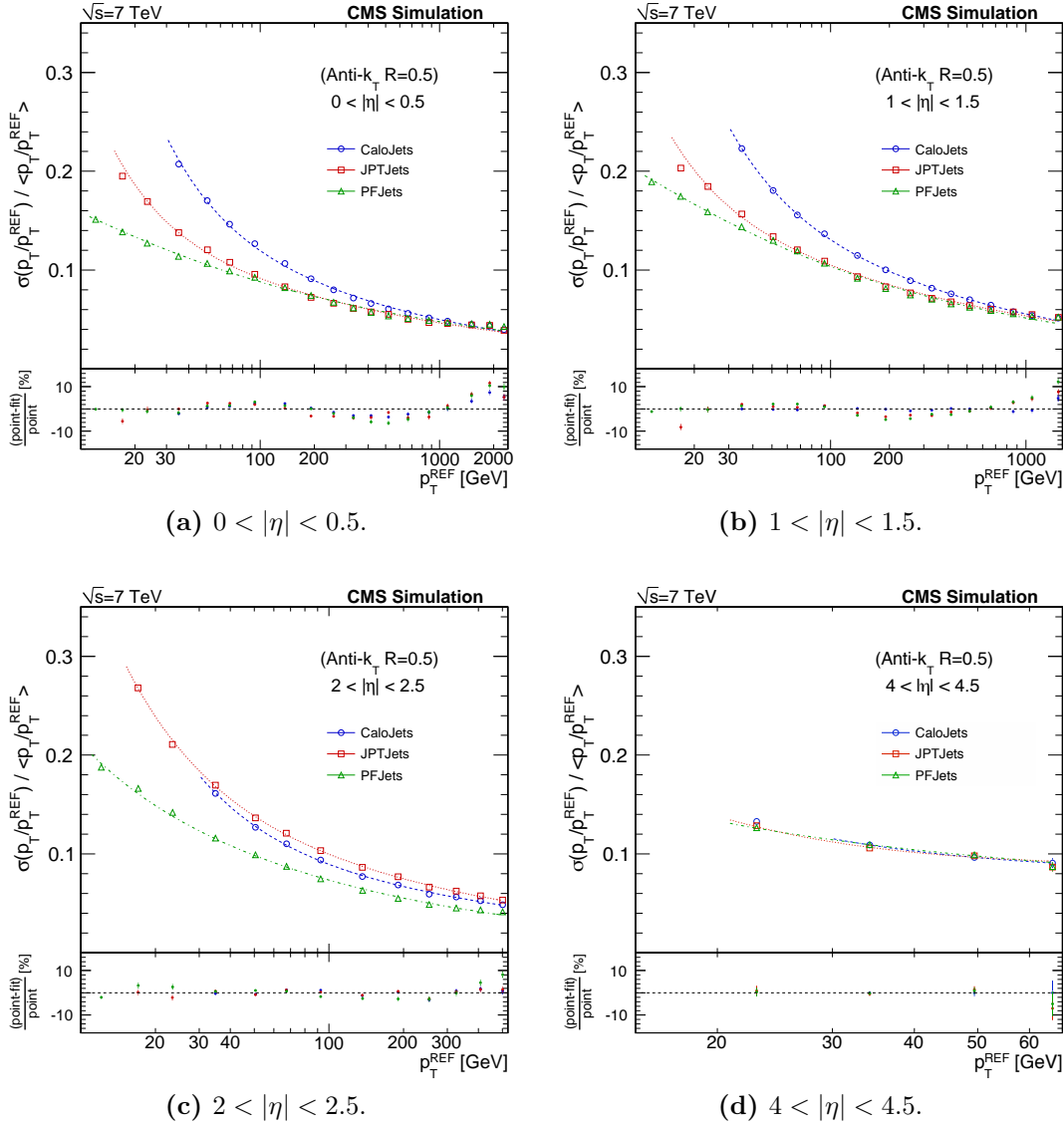
Figure 3.1.: Comparison of calo–jet, JPT and PF–jet p_T resolution from MC where calorimeter clusters (PF candidates) are used as inputs to the AK(0.5) jet clustering algorithm for four $|\eta|$ ranges covering the whole HCAL subdetector. p_T^{REF} is the p_T of the jet calculated from MC truth. Taken from [68].

(a) 20 GeV < pfMET < 50 GeV.

(b) 50 GeV < pfMET < 100 GeV.

(c) 100 GeV < pfMET < 200 GeV.

(d) 20 GeV < pfMET < 200 GeV.
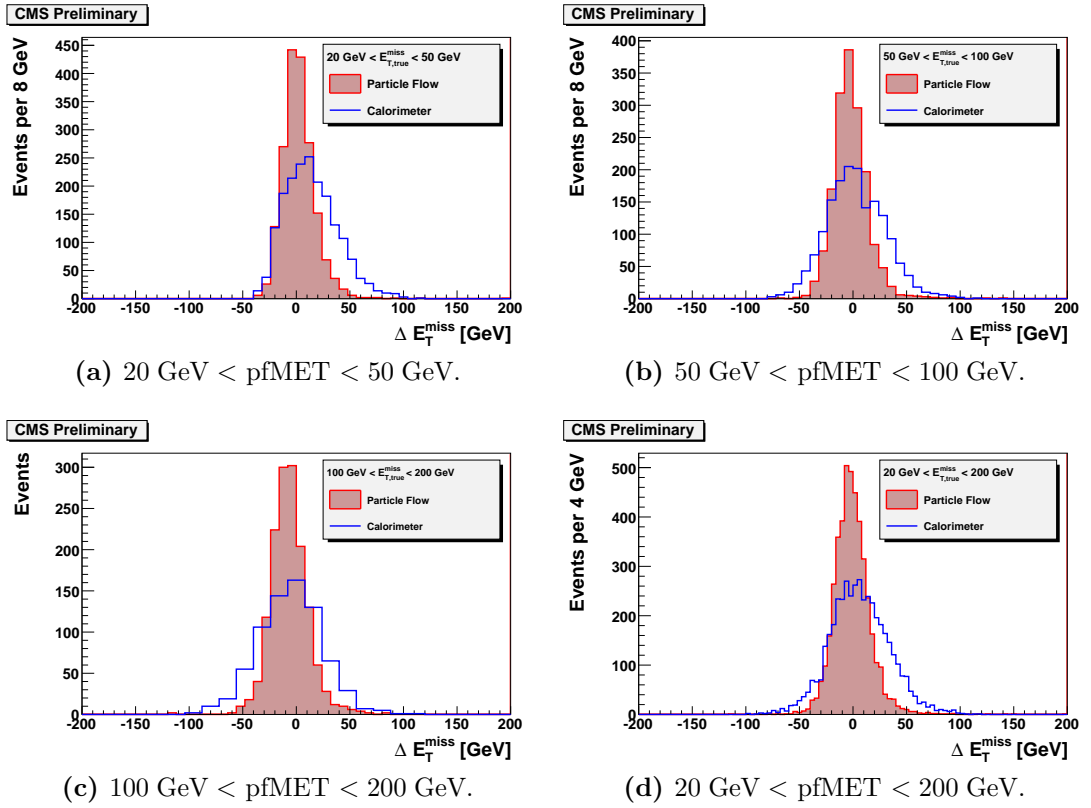
Figure 3.2.: Comparison of calo–MET versus pfMET resolution from MC. pfMET is computed from the negative vector sum of all PF objects in the events. Calo–MET is obtained from calorimeter towers corrected for the jet energy scale and identified muons in the event. Taken from [65].

(a) Jet p$_T$ (GeV).

(b) Jet η.

(c) Jet ϕ.
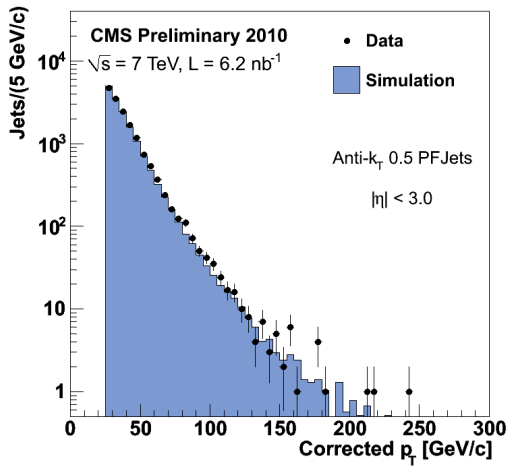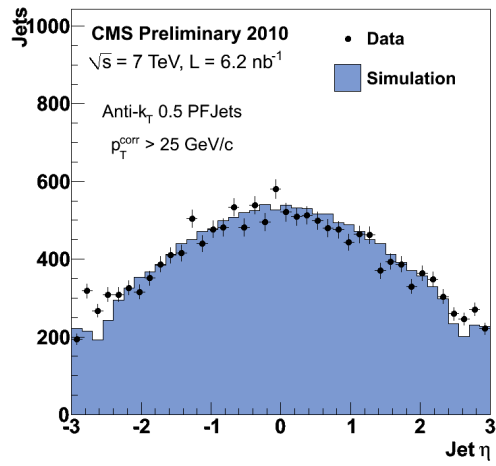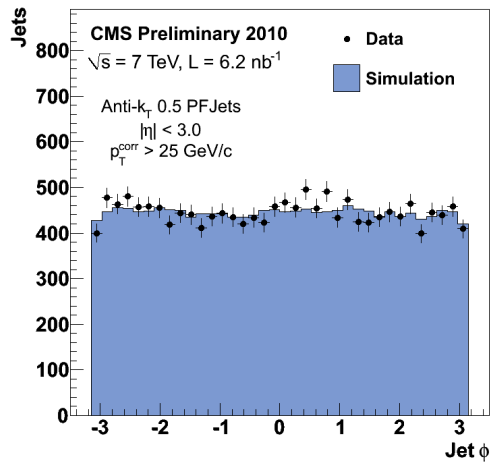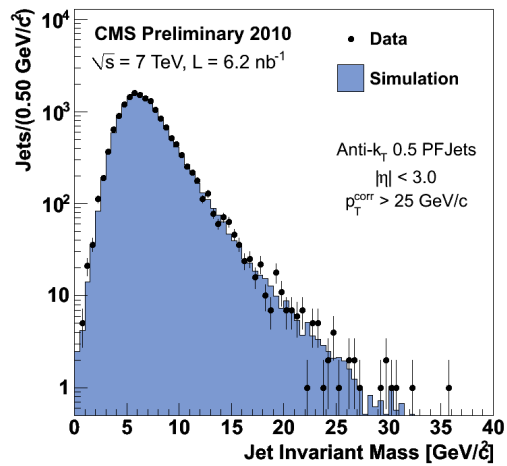
(d) Jet Inv. Mass (GeV).

Figure 3.3.: Distributions of simple AK(0.5) PF–jet properties, 3.3a jet p$_T$, 3.3b jet η, 3.3c jet ϕ and 3.3d jet invariant mass, in early CMS 7 TeV data compared to MC expectation. Taken from [70].

3.2. Electrons

Electrons may be generally characterised by the presence of a track in the silicon tracker and energy deposits in the ECAL. Information from both these subdetectors is combined to identify them. A description of the reconstruction methods and performance is presented.

Electrons are reconstructed using two methods for the track seeding [72], ECAL or tracker based. Track driven seeding is preferable for low p_T electrons and loosely isolated electrons typically contained within hadronic jets. ECAL driven seeding is established from superclusters – groupings of associated energy deposits to account for the energy spread in ϕ from radiating electrons in the tracker – with $E_T > 4$ GeV. The superclusters are matched to inner tracker hits. Electron tracks are then built from these tracker seeds, with full trajectories established by performing a Gaussian Sum Filter (GSF) [73] fit to the track rather than the default KF to account for energy loss due to Bremsstralhung in the tracker material.

Electron candidates are also subject to a preselection following the track matching. A multivariate discriminant (see section 3.4) or matching between the ECAL supercluster and GSF track is used for tracker based and ECAL based seeding respectively.

The early CMS identification strategy for electrons was to perform a robust and comparatively simple cut based selection rather than using multi-variate techniques. A set of detector variables is used to control identification and isolation. The ratio of energy deposits in the HCAL with respect to the ECAL (H/E) provides a measure of hadronic to electromagnetic deposits (hadron leakage) for clusters matched to the electron track. The matching between the ECAL cluster position and the track position may be controlled with $\Delta\eta$ and $\Delta\phi$ variables. Finally, $\sigma_{i\eta i\eta}$ measures the supercluster width in η. The choice of distinguishing shower shapes in η rather than ϕ is motivated by the negligible effect of the magnetic field in the azimuthal direction.

Photon conversions and electrons are distinguished using the impact parameter ($d0$) of the track as well as ensuring the track has hits in the inner layers of the silicon detector. Conversion rejection is further improved using the fact that conversion electron tracks are parallel to each other from the decay point and throughout the $r - z$ plane. Two variables, $d\cot(\Theta)$ and $Dist$ are defined for all CTF tracks within a cone of $\Delta R = 0.3$ of the electron GSF track, such that $d\cot(\Theta) = \cot(\Theta_{CTF}) - \cot(\Theta_{GSF})$ and $Dist$ is the distance in the $x - y$ plane between the electron GSF track and the CTF track [72, 74].

Electron reconstruction efficiency is measured using a variety of techniques. A Tag and Probe (TP) analysis using Z → ee events is used as a standard reference method [72]. One good electron with supercluster $E_T > 20\,\text{GeV}$ and identification and isolation requirements of the Z → ee analysis [75] is used as the tag. The probes are required to pass supercluster $E_T > 20\,\text{GeV}$ and have an invariant mass consistent with the Z^0 hypothesis when combined with the tag. In addition to this measurement, the reconstruction efficiency is also determined from W → $e\nu_e$ events. After supercluster and isolation requirements on the electron, an unbinned maximum likelihood fit is performed to the transverse mass and signal and background yields and reconstruction efficiencies extracted. Efficiencies are found to be $99.3\% \pm 1.4\%$ and $96.8\% \pm 3.4\%$ in the ECAL barrel and endcap respectively from the TP analysis. Similar results are found with the W → $e\nu_e$ analysis. The results of the ratio of these measurements with MC expectation are shown in figure 3.4.
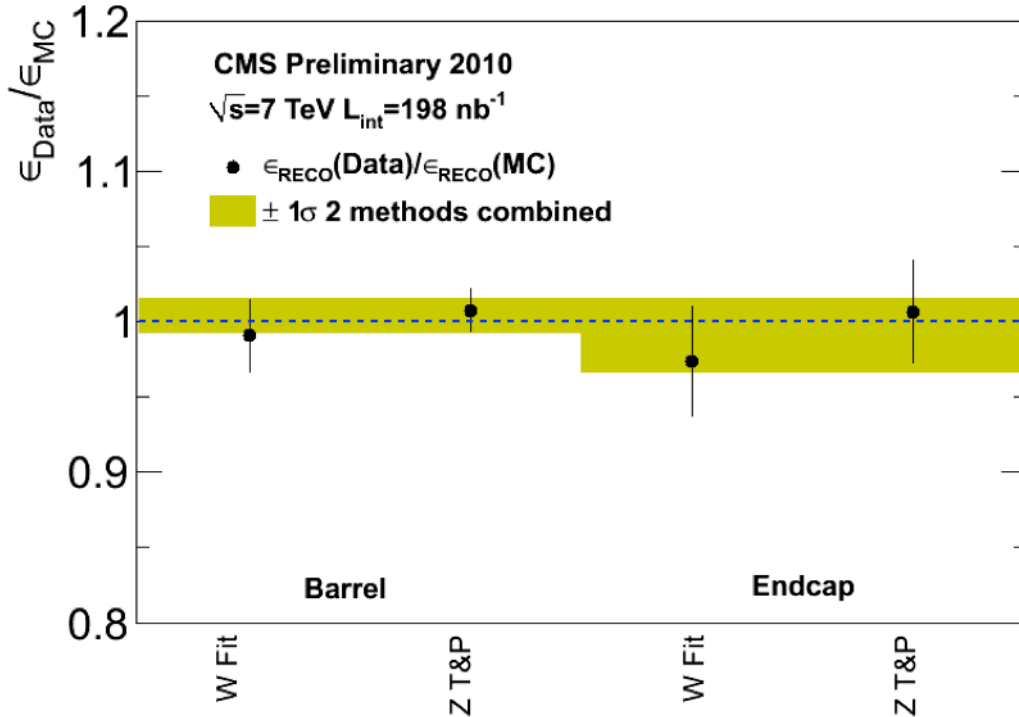
Figure 3.4.: Measured divided by expected efficiency (MC) of cut based electron identification measured in Z → ee TP and a maximum likelihood fit in W → $e\nu_e$, shown for the barrel and endcap regions of the ECAL. The combined efficiency of both measurements is also shown. Taken from [72].

The electron fake rate, defined as the number of electron candidates passing the background selection and the considered electron identification divided by the total number

of candidates passing the background selection is shown as a function of E_T and η in figure 3.5. The electron identification points WP95 and WP80 are defined from MC samples for electrons with $E_T > 20$ GeV to be 95% and 80% efficient respectively. The efficiencies in data ($Z \to$ ee and $W \to e\nu_e$) for these selection points are found to be in good agreement with the MC.
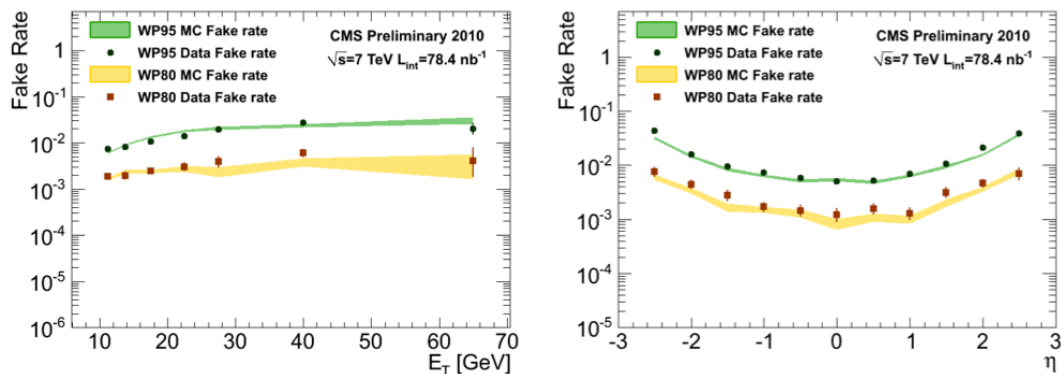
Figure 3.5.: Electron fake rate in data and MC as a function of η and E_T for 80% and 95% efficient selections. Taken from [72].

3.3. Muons

Muons are detected and reconstructed with the silicon tracker and dedicated muon system [56]. Tracks in both subsystems are reconstructed separately. These are then combined in two possible ways: *global* muons are constructed from a global fit to a track in the muon system with a matching track in the silicon tracker; *tracker* muons are constructed with the reverse approach in which tracks in the silicon tracker are extrapolated to the muon system. This procedure is more efficient for low momentum muons since only part of a track is required in the muon chambers. Finally, muons may also be reconstructed as a *standalone* muon ($\sim 1\%$ of collision muons) if either of the two previous reconstructions fails [76].

Muon identification is primarily based on the quality of the tracks in both the tracker and muon chambers. This includes the value of the χ^2 fit over the tracker and muon system, number of standalone hits and number of silicon tracker hits. In addition, the MIP nature of muons can be exploited by looking for consistent energy deposits in the HCAL and ECAL associated with candidate tracks as well as compatibility of the muon chamber segments with respect to the extrapolated silicon tracker track [61].

The efficiency for low p_T muons is measured in $J/\psi \to \mu\mu$ events using a TP technique. The results of this analysis are shown for *global* muons, for $|\eta| < 1.2$ and $1.2 < |\eta| < 2.4$ in figure 3.6.
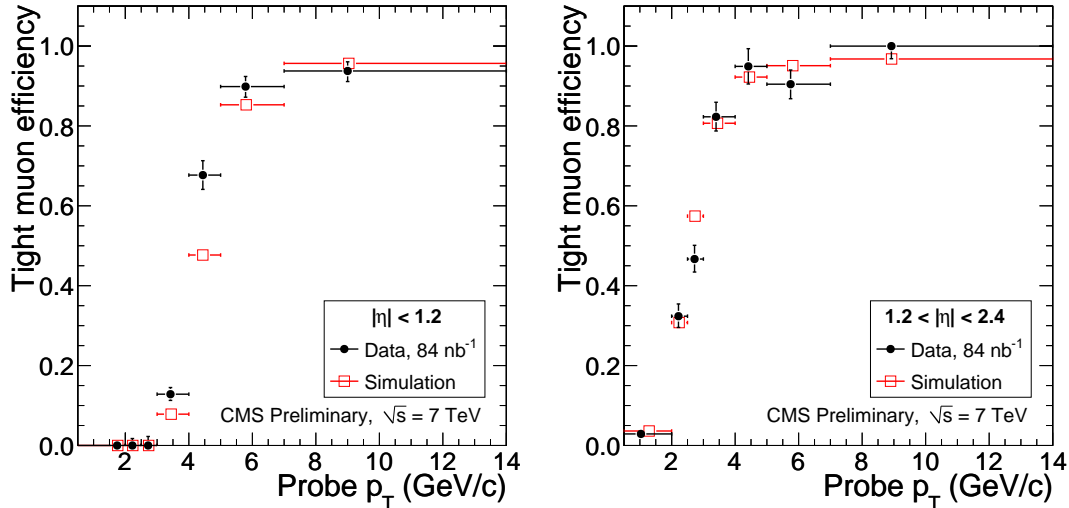
Figure 3.6.: Muon reconstruction efficiency evaluated using a TP analysis of $J/\psi \to \mu\mu$ events. Taken from [76].

Cosmic ray events show resolutions of $\Delta p/p < 1\%$ for $p_\mu = 10$ GeV increasing to $\sim 8\%$ at 0.5 TeV. Charge mismeasurement is shown to range from $< 0.01\%$ for $p_\mu = 10$ GeV to $\sim 1\%$ at $p_\mu = 500$ GeV [77]. Cosmic muons coincident with bunch crossings during LHC data taking may be distinguished from collision muons using a simple set of reconstruction variables and triggers based on timing and impact parameter considerations. Thus the expected number of *global* muons originating from cosmics is expected to be below 0.1%.

3.4. Taus

τ leptons have a lifetime of $\tau = 290.6$ fs and thus decay prior to entering the tracker ($c\tau = 87.11$ μm) with a hadronic branching fraction of around 65% [78]. The leptonic decay ($BR \approx 35\%$) modes are reconstructed and treated as electrons or muons. The hadronic τ decay is generally into one or three charged light mesons (π^+ and π^-) with neutral mesons ($\pi^0 \to \gamma\gamma$) and a ν_τ to conserve lepton flavour.

CMS uses two algorithms [79] to identify hadronic τ decays – Hadron Plus Strips (HPS) and Tau Neural Classifier (TaNC) – both of which rely on PF reconstruction described above. A τ candidate starts from a PF–jet using the anti-K$_T$ jet clustering algorithm

with a cone parameter of $\Delta R = 0.5$. The neutral pions are then reconstructed and finally combined with the charged mesons.

The HPS algorithm concentrates on identifying the photons produced in the decay of the π^0 following the τ decay. The photons are expected to convert with high probability in the tracker. This produces a broadened signature in the ECAL due to the bending of $e^{\pm}$ in the magnetic field. A strip is centered on the most energetic electromagnetic (e/γ) particle in the seed PF–jet. Electromagnetic particles are then searched for within ($\Delta\eta = 0.05, \Delta\phi = 0.20$). If any are found, the most energetic is added to the strip and the 4-momentum is recalculated. This process is repeated until no other particles are found. Hadronic τ decay modes – single hadron ($X^{\pm}\nu_{\tau}$ and $X^{\pm}\pi^0 \ \nu_{\tau}$ with a low energy π^0), single hadron + single strip ($X^{\pm}\pi^0 \ \nu_{\tau}$ with the photons close to each other), single hadron + two strips ($X^{\pm}\pi^0 \ \nu_{\tau}$ with well separated photons) and three hadrons ($X^{\pm}X^{\mp}X^{\pm}\nu_{\tau}$) – are reconstructed from the combination of the charged hadrons in the PF–jet and strips satisfying $p_T^{strip} > 1$ GeV. The hadrons and strips are required to be contained within a cone of $\Delta R = 2.8 \ \text{GeV}/p_{T_{\tau}}$ and the direction of $p_{T_{\tau}}$ must be within $\Delta R = 0.1$ of the original PF–jet [79].

The 4-momenta of the hadrons and strips are reconstructed assuming all the charged hadrons are pions and have invariant masses compatible with any intermediate resonances. Finally, isolation criteria are set. Three working points (loose, medium and tight) are defined according to the momentum threshold of particles within the $\Delta R = 0.5$ isolation cone. Specifically these require no PF charged candidate with p_T greater than 1.0 GeV (loose), 0.8 GeV (medium) and 0.5 GeV, and no PF γ candidates with E_T greater than 1.5 GeV (loose), 0.8 GeV (medium) and 0.5 GeV (tight).

Additional discriminants may be applied to control light lepton (e, μ) faking τ. Loose or tight μ rejection may be applied. These add requirements on the reconstruction of the leading track.

In the case of electrons, the faking occurs if an electron is consistent with a $\pi^{\pm}$. The PF algorithm contains a discriminant e_{disc} based on a Multivariate Analysis (MVA) to distinguish electrons from $\pi^{\pm}$, with a value varying from -1.0 (π compatible) to 1.0 (electron compatible). Three working points for electron rejection exist: loose rejection requires $e_{disc} < 0.6$, whilst medium rejection requires $e_{disc} < -0.1$ and ECAL crack rejection. Tight electron rejection adds additional requirements to the medium rejection working point based on HCAL or ECAL deposits and τ mass requirements depending on the electromagnetic content of the τ jet. The electron rejection was studied in data

for the tight and loose working points in Z → ee decays using a TP method with one reconstructed electron and one electron passing the loose HPS algorithm [79] without any electron veto. From this, it was shown that the tight electron rejection working point has a misidentification rate of $\sim 2\%$ with a drop in true τ efficiency of $\sim 4\%$. The loose electron rejection working point was optimised for τ efficiencies 99.5% and has a larger misidentification rate of 20%.

The TaNC algorithm builds on a 'shrinking cone' algorithm which takes the highest p_T particle (generally a $\pi^{\pm}$) in the PF–jet with $p_T > 5$ GeV and within $\Delta R = 0.1$ of the jet direction to be the leading τ jet particle. The τ 4-momentum is then reconstructed from the sum of all particles within $\Delta R = 0.15$ and with $p_T > 0.5$ GeV of this leading particle. A signal cone and isolation cone are defined around the leading particle. The signal cone is expected to contain the τ decay products and is defined as $\Delta R = 0.15$ for leading photons and $\Delta R = 5$ GeV/E_T (with $0.07 \leq \Delta R \leq 0.15$) for leading charged hadrons. A schematic of the signal and isolation cone arrangement can be seen in figure 3.7.
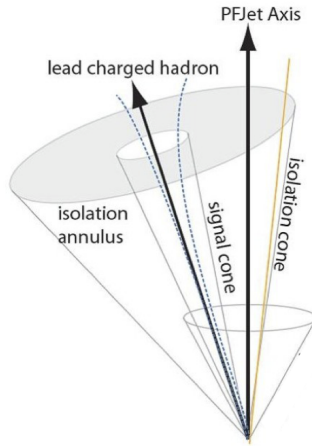
Figure 3.7.: Schematic of the signal cone, isolation cone and isolation annulus used in the TaNC τ reconstruction algorithm. Taken from [80].

The region between the signal cone and the isolation cone ($\Delta R = 0.5$) defines the isolation annulus which allows discrimination between isolated τ and QCD jets.

The τ decay mode is inferred from the particles reconstructed within the signal cone. If the decay mode is identified as a possible hadronic τ decay, a neural network is then used to determine the quality of the τ based on the particles present in the signal cone and isolation annulus. The TaNC provides three working points (loose, medium and tight – in analogy to the HPS working points) established by adjusting the selection thresholds on the output of the neural network.
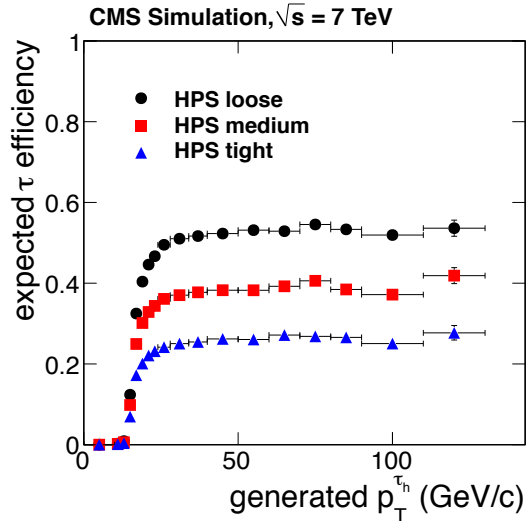
Figure 3.8.: HPS τ efficiencies for three identification points as determined in $Z \rightarrow \tau\tau$ MC events. Taken from [79].

As shown in figure 3.8, the HPS algorithm has an identification efficiency for τ with $p_T > 15$ GeV in MC $Z \rightarrow \tau\tau$ events of 23%, 34% and 46% for the tight, medium and loose working points respectively after reweighting (factor ~ 1) to data. Similarly the TaNC algorithm shows an efficiency of 30%, 43% and 54% for the analogous working points [79]. The misidentifcation probability for a jet to fake a τ taken for the loose working points of both the TaNC and HPS algorithms is shown in figure 3.9. Figure 3.10 shows the fake rate measured in the muon–enriched QCD and W+jets data sample against the τ efficiencies for both HPS and TaNC algorithms.

The SSDL analysis used both TaNC and HPS reconstructed τs in the 2010 and 2011 CMS datasets respectively.
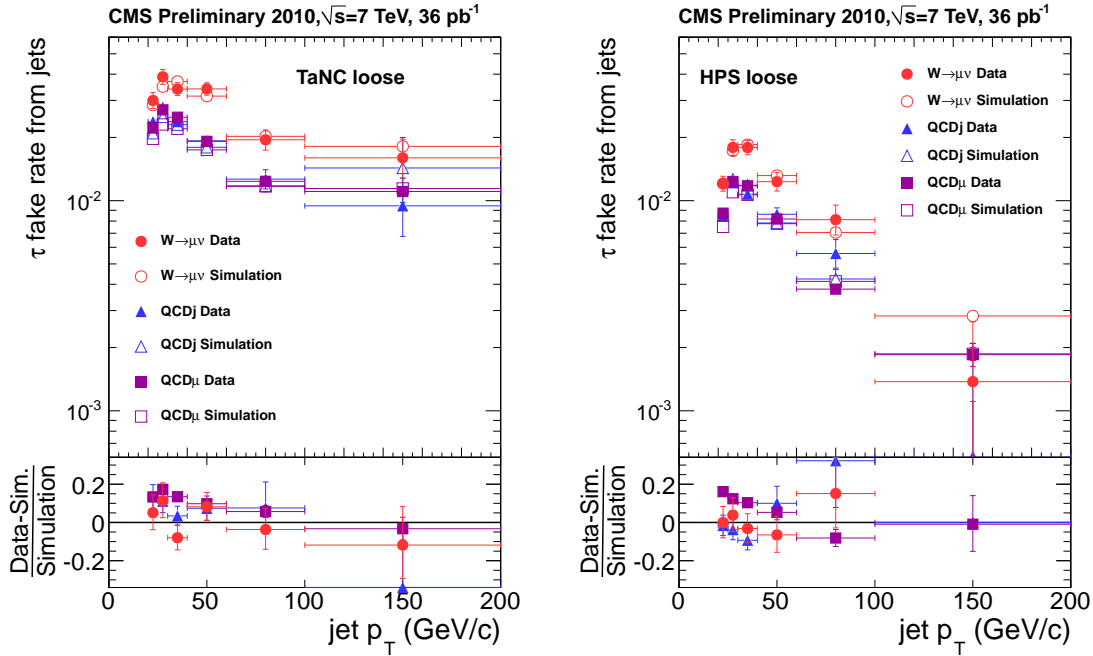
Figure 3.9.: Loose τ fake rate probability from jets for the HPS and TaNC reconstruction algorithms as a function of jet p_T, for QCD, muon–enriched QCD and W events in data and MC. Taken from [79].
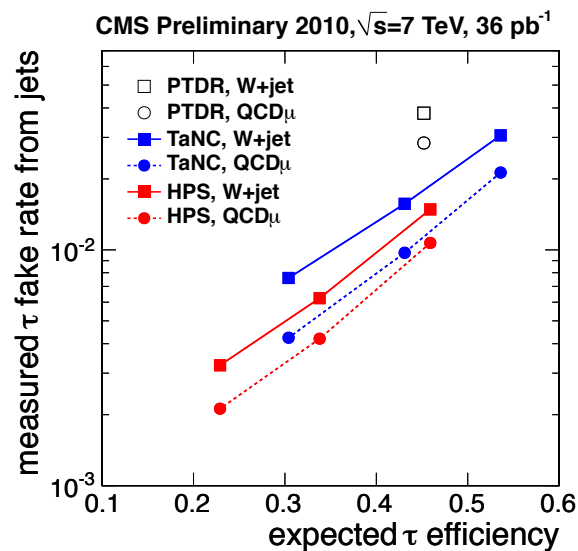
Figure 3.10.: Reconstructed τ misidentification rate for jets measured in QCD and W data against expected efficiency measured in MC for the TaNC and HPS algorithms. Expected performance of the early (now defunct) fixed-cone algorithm is also shown [9]. The loose, medium and tight selection points for both algorithms correspond to the high/mid/low points of efficiency. Taken from [79].

Chapter 4.

Same–Sign Dilepton Analysis Triggers and Selection

As discussed in section 1.3, the final states of interest in the SSDL analysis are characterised by the presence of E_T^{miss}, hadronic jets as well as same–sign electrons, muons or τ (where the τ is taken to decay hadronically). Hadronic activity is quantified directly by the presence of jets in the event and by the scale of H_T defined as the scalar E_T sum of the jets in the event.

The p_T cut of the leptons (e, μ and τ) is kept as low as possible within the constraints of the CMS reconstruction to be sensitive to a possible soft lepton p_T spectrum produced in a SUSY decay. Isolation quantities are used in the online trigger and offline selection. These are defined for the tracker, ECAL and HCAL and quantify the amount of activity surrounding the track or identified object calorimeter deposit within a ΔR cone.

4.1. Triggers

The trigger strategy differed between the published SSDL (including τ channels) analysis of 2010 [81] and the update with the certified 2011 CMS dataset [82]. Initially, whilst the LHC was delivering low instantaneous luminosity ($\sim 1 \times 10^{32}$ cm^{-2} s^{-1}) a sufficiently low H_T unprescaled trigger was available.

Specific trigger paths were implemented for the 2011 and subsequent data taking period due to the need for sensitivity to low–p_T leptons with a hadronic τ whilst maintaining a

sufficiently low rate (~ 5 Hz) at the HLT under higher instantaneous luminosity regimes ($\sim 5 \times 10^{32}$ to $> 2 \times 10^{33}$ cm^{-2} s^{-1}).

Prior to the final validation and implementation of the triggers in table 4.2, the SSDL analysis used a H$_T$ > 200 GeV with a p$_T$ > 5 GeV muon or p$_T$ > 8 GeV electron HLT path instead of the specific muon and electron SSDL paths. Only the first 31 pb^{-1} was collected using these. They are not discussed further.

The nomenclature used to label the paths describes the content of the path according to the requests. This starts with the prefix 'HLT' and then lists the lepton request and corresponding p$_T$ cut, the H$_T$ request and finally the Particle-Flow Missing Transverse Hadronic Energy (pfMHT) request. This is summarised in table 4.1.

Segment of path label	Meaning
HTxxx	Describes the quantity of hadronic activity requested by the trigger evaluated as the scalar sum of the E$_T$ of the corrected HLT jets (*e.g. HT200 corresponds to a* H$_T \geq$ *200 GeV request*).
ele/mu/diTauxx	Describes the type of lepton requested and the minimum corresponding p$_T$ requirement (*e.g. diTau10 requests two* τ *with* p$_T \geq$ *10 GeV*).
pfMHTxxx	Describes the quantity of E$_T^{miss}$ requested by the trigger (*e.g. pfMHT35 corresponds to pfMHT* $\geq$ *35 GeV*).

Table 4.1.: Nomenclature used in the HLT SSDL paths shown in table 4.2. All paths are preceded with the prefix 'HLT' and then lists the lepton request the H$_T$ request and the pfMHT request.

4.1.1. Constructing SSDL τ High Level Trigger Paths

Due to the lack of HLT paths sensitive to low p_T hadronic τs whilst maintaining a low rate, three new HLT paths designed for SUSY discovery were implemented for the 2011 data taking period. Each path consists of a pfMHT and H_T request, characteristic of a general SUSY event. In addition, a soft lepton request (e, μ, and di–τ) is added.

The pfMHT and H_T cuts are increased over the course of instantaneous luminosity increase to maintain a low and approximately constant trigger rate. This is summarised in table 4.2.

All triggers are seeded with a hadronic activity L1 path which requires $H_T > 100$ GeV.

The general construction of a HLT path is to start with the least computationally intensive request where the trigger requests are defined as an orthogonal set of requirements in the final trigger, progressing towards the most computationally intense algorithms at the end of the chain. Additionally, basic objects may be constructed once at the start of the chain (with some loose criteria) and reused in various sections of the path. An example of this is the use of PF–jets used for pfMET and the τ requests.

The following selection was used in the implementation of the HLT paths. The contributions to each request of the triggers are described below in the order in which they are computed. The construction of the trigger paths is illustrated schematically in figure 4.1. This diagram shows the chain of reconstruction and selection requests following the L1 $H_T > 100$ GeV seed for each of the H_T, pfMHT, electron, muon and τ sections of the SSDL triggers. All paths start with a H_T request following the seed. Electron or muon reconstruction follows for their respective paths, and finally the pfMHT request is made. In the case of the τ paths, the pfMHT request is made before the more computationally intensive τ request. The stages of each path are shown as organised for the individual triggers. In practice, the pfMHT request may be shared between the muon and electron path (i.e. evaluated once) to reduce computation time. In this scenario, the second pfMHT request (in the muon path if already evaluated in the electron path or vice versa) would occur following the H_T request and not at the end of the path.
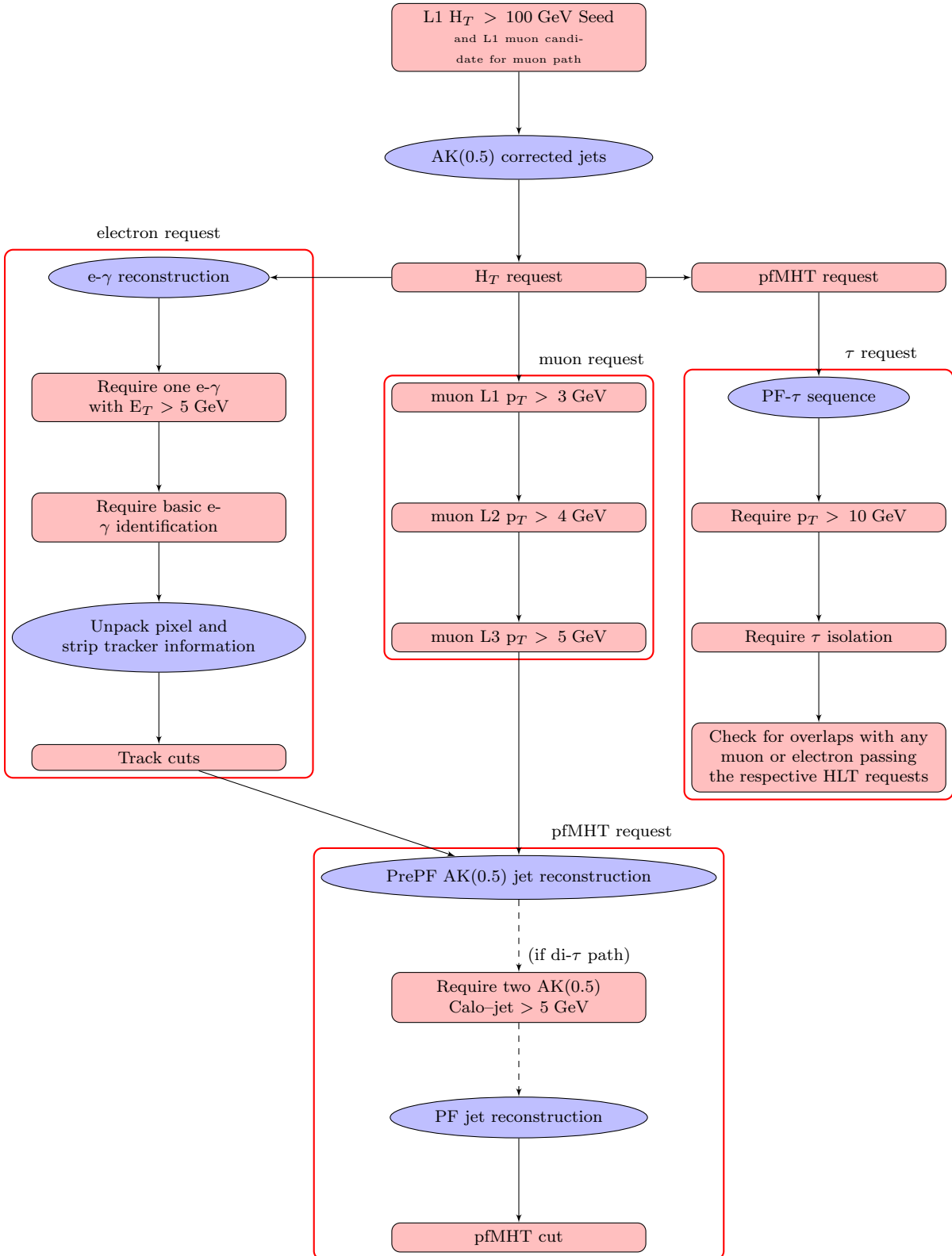
Figure 4.1.: Schematic order of HLT computations for the SSDL triggers. Reconstruction steps are illustrated by blue ellipses whilst HLT decisions are represented by red rectangles. The paths start with a L1 $H_T > 100$ GeV request followed by a HLT H_T request as specified in table 4.2. This is then followed by the lepton reconstruction and selection. Finally, the pfMHT request is applied. In the case of the τ paths, these final steps are reversed.

Inst. Luminosity (cm^{-2}s^{-1})	HLT paths	Approx. Luminonsity
5×10^{32}	HLT_HT200_ele5_pfMHT35	160 pb^{-1}
	HLT_HT200_mu5_pfMHT35	
	HLT_HT200_diTau10_pfMHT35	
1×10^{33}	HLT_HT250_ele5_pfMHT35	635 pb^{-1}
	HLT_HT250_mu5_pfMHT35	
	HLT_HT250_diTau10_pfMHT35	
2×10^{33}	HLT_HT300_ele5_pfMHT40	137 pb^{-1}
	HLT_HT300_mu5_pfMHT40	
	HLT_HT300_diTau10_pfMHT40	
$> 2 \times 10^{33}$	HLT_HT350_ele5_pfMHT45	Not used in
	HLT_HT350_mu5_pfMHT45	the analysis
	HLT_HT350_diTau10_pfMHT45	presented here.

Table 4.2.: HLT paths implemented for the SSDL τ and lepton analysis. The H$_T$ and pfMHT requests were increased as a function of instantaneous luminosity to maintain an approximately constant rate of 3 Hz.

H$_T$ request

All paths start with a L1 H$_T$ seed (H$_T > 100$ GeV) followed by a request on the amount of hadronic activity in the event, computed from corrected AK(0.5) calorimeter jets. The jets are computed by unpacking the ECAL and HCAL information into towers and applying L2 and L3 jet corrections. The cut applied for the 5×10^{32} cm^{-2} s^{-1} paths is $\sum E_T > 200$ GeV, evaluated from jets with p$_T > 40$ GeV and $|\eta| < 3$. This was increased as a function of instantaneous luminosity to control the trigger rates as shown in table 4.2.

Electrons and Muons

Following the hadronic activity request, the electrons and muons are constructed and selected for their respective paths.

Muons are constructed from a L1 muon seed and are treated in two more stages at the HLT. The HLT starts with a p_T and η cut on the L1 muon constructed solely from the muon system (RPC, CSC and DT). This stage is followed by the L2 HLT reconstruction using the L1 seed. This level refits a KF track in the muon chambers and provides calorimeter information for isolation criteria. Finally, the L3 reconstruction includes silicon tracker information. The SSDL paths reconstruct the full muon track using the 'Outside–In' algorithm, which constructs the track from the outer hits of the silicon tracker towards the center of the pixel tracker. This has been shown to be the most efficient algorithm for HLT muon track reconstruction in cosmic data [77].

The criteria applied in the SSDL HLT muon request are shown below.

Muon identification:

- p_T L1 > 3 GeV

- p_T L2 > 4 GeV

- p_T L3 > 5 GeV

- $|\eta| < 2.5$

- Distance in the transverse plane to the PV < 2 cm

- No isolation

The p_T cuts are chosen to be as low as possible in accordance with the physics aim of the analysis whilst maintaining near 100% reconstruction efficiency. The incremental increase to the final cut of 5 GeV is due to the increased p_T resolution between the different levels. The impact parameter cut is sufficiently loose to maintain a high detection efficiency for muons produced from B meson decays. No isolation is applied since this was shown in simulation and confirmed in data to be unnecessary to control the rate.

The electrons are reconstructed in stages, starting with information from the 5×5 calorimeter towers and ES. E_T and shower identification is applied to the reconstructed ECAL information. This includes cluster shape, ECAL isolation, H/E (where the HCAL activity is previously computed in the H_T request) and HCAL isolation. If the ECAL

cluster satisfies the identification criteria, the tracker information is unpacked. A pixel seed is first matched to the previously identified ECAL crystal to produce an electron candidate. Once the match criteria ($\Delta\eta$ and $\Delta\phi$) is satisfied, the full track is reconstructed using a combinatorial KF and isolation requirements are applied.

The SSDL HLT electron criteria are shown below.

Electron identification: the HLT electron identification is characterised by various working points. The 'very loose' identification point is used. Barrel and (endcap) values are shown. Isolation is evaluated in a cone of $\Delta R = 0.3$. The cuts applied are as follows:

- H/E < 0.15 (0.10)

- $\sigma_{i\eta i\eta}$ < 0.024 (0.040)

- ECAL Isolation/E_T < 0.2 (0.2)

- HCAL Isolation/E_T < 0.2 (0.2)

- $\Delta\eta$ < 0.01 (0.01)

- $\Delta\phi$ < 0.15 (0.10)

- Track isolation/E_T < 0.2 (0.2)

PF requests – pfMHT and τ

The PF segments of the triggers are evaluated at the end of the trigger paths. The muon and electron paths end with a pfMHT request. In the case of the τ path, the pfMHT request is evaluated first due to the computationally intensive PF–τ HLT modules. The PF computations begin with the reconstruction of uncorrected calorimeter AK(0.5) jets with an E_T > 5 GeV request. Pixel and strip tracks are then reconstructed and PF track candidates are found and matched to the calorimeter clusters. In addition, L2 and L3 muon reconstruction is performed and is merged with the tracks. Finally the PF sequence is run to create particle flow blocks and PF–jets are created from the AK(0.5) clustering algorithm. These jets are used to compute the pfMHT in the event (negative vector sum of the PF-jet E_T).

The pfMHT definition and cuts applied in the trigger paths are summarised as:

pfMHT: Evaluated as the negative vectorial sum $(\sum_{pfJets} -\vec{p_T})$ with PF jet thresholds $p_T > 15$ GeV and $|\eta| < 3$.

and was increased to control the rate in association with H_T as shown in table 4.2.

The HLT τ are computed in a similar manner to the pfMHT in the event. Starting from the calorimeter and track deposits, a τ PF sequence is run to create PF–τ blocks and these are then clustered into τ jets using the AK(0.5) algorithm. The path requests at least two τ–jets with $E_T > 10$ GeV before applying the isolation criteria. Each τ at the HLT is required to have a leading track with $p_T > 3$ GeV and is required to be tightly isolated to control the path rate. Finally, HLT τs are checked for overlaps with any electrons and muons passing the criteria of the light lepton paths described previously.

The PF–τ criteria are as follows:

τ identification:

- $E_T > 10$ GeV

- Intermediate reconstruction track $p_T > 3$ GeV

- PF–τ track isolation < 1 GeV

- PF–τ γ isolation < 1.5 GeV

- $\Delta\eta < 0.3$ and $\Delta\phi < 0.3$ between τ–electron and τ–muon

where the isolation criteria are taken as the tight HLT working point, consistent with other tight τ paths.

4.1.2. Trigger Performance

The trigger performance is evaluated in both online and offline quantities. The trigger rate was evaluated first by running an offline simulation of the trigger and the cuts applied in each request were adjusted such that the total bandwidth was ~ 3 Hz. Online rates were initially found to be higher than expected (~ 2 Hz, ~ 4 Hz and ~ 6 Hz for the electron, muon and di–τ paths respectively) in the early 5×10^{32} cm^{-2} s^{-1} trigger table. These were reduced to be consistent with simulation following HLT pfMHT updates..

As discussed in section 4.1.1 above, the inclusion of PF requests to an HLT path increases the computation time to evaluate the path. The timing of the full menu is checked with

and without the proposed paths in minimum bias data and the increase in computation time is calculated. This is shown with and without pileup (factor 10) in figure 4.2. The mean increase in timing with the inclusion of all HLT modules used in the SSDL triggers was negligible in the first version of the paths – 0.25 ms without pile up, and 0.7 ms with a factor 10 pile up, and is expected to decrease as the HLT PF algorithms improve.

The offline performance of the triggers is evaluated using a second set of triggers such that each HLT request may be isolated, in two instantaneous luminosity regimes – 5×10^{32} cm^{-2} s^{-1} and 1×10^{33} cm^{-2} s^{-1} respectively between which the triggers were adjusted in their H$_T$ cut to maintain a roughly constant rate throughout.

The efficiency of each request of the triggers in the corresponding offline quantity sets the lowest cut values that may be applied in the offline analysis to maintain a near 100% efficiency in the offline selection. The naming convention used below is consistent with that previously described in section 4.1 and used in table 4.2. '*lepton*' is used to refer to any of the three paths.

H$_T$ Request

The H$_T$ turn-on was evaluated for both instantaneous luminosity regimes considered. In the first regime, HLT_HT200_*lepton*_PFMHT35 was used as the denominator, and events passing HLT_HT250_*lepton*_PFMHT35 as the numerator. The second regime was used to evaluate the H$_T$ response of the HLT_HT350_*lepton*_PFMHT45, using HLT_HT250_*lepton*_PFMHT35 as the denominator. An additional offline pfMET cut of 110 GeV was applied to the denominator to account for the higher online pfMHT cut in the numerator. The performance for these two regimes is shown in figures 4.3 and 4.4. A flat efficiency greater than 98% was found at 350 GeV and 450 GeV for the first and second triggers respectively. Thus the triggers are found to be 100% efficient in offline H$_T$ around 100 GeV above the online trigger cut value.

pfMHT Request

The pfMHT turn-on is shown for both instantaneous luminosity regimes considered. In the first regime, the efficiency was evaluated using events passing HLT_HT200_*lepton* as the denominator and events passing the HLT_HT200_*lepton*_PFMHT35 as the numerator. The trigger has an efficiency greater than 98% in offline pfMET at 120 GeV as shown in figure 4.5a.
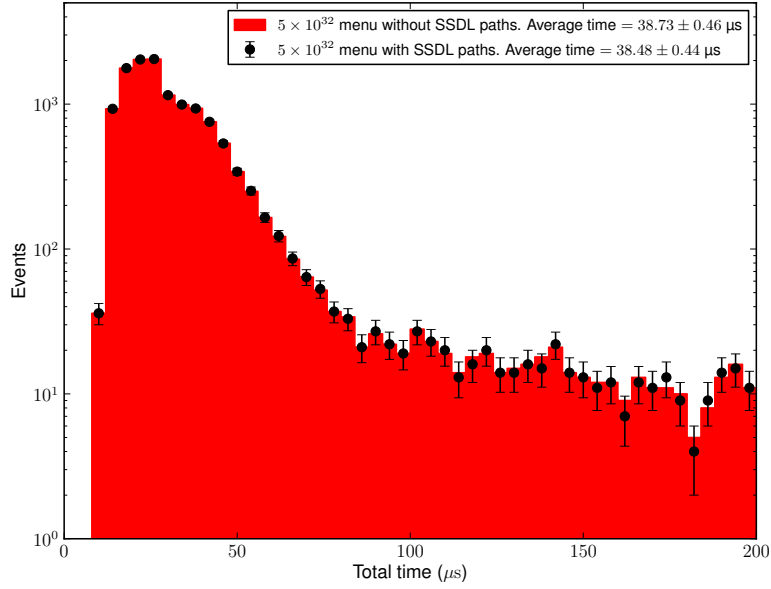
(a) Timing without PU.
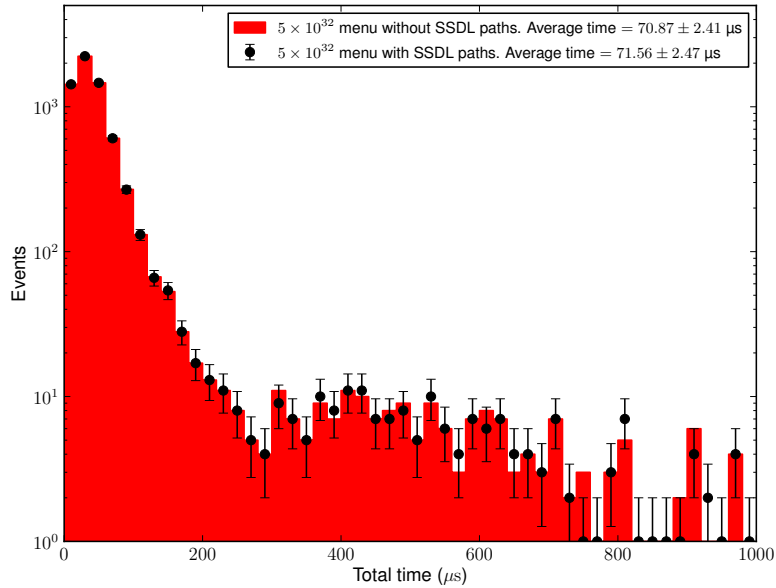
(b) Timing with PU10.

Figure 4.2.: Effect on HLT timing performance when including the first version of the SSDL triggers to the 5×10^{32} menu shown with (figure 4.2a) and without (figure 4.2b) the effects of a factor 10 PU.

Between the two considered regimes, significant improvements and debugging took place in the online PF implementation. The turn-on performance in the 1×10^{33} cm^{-2} s^{-1}
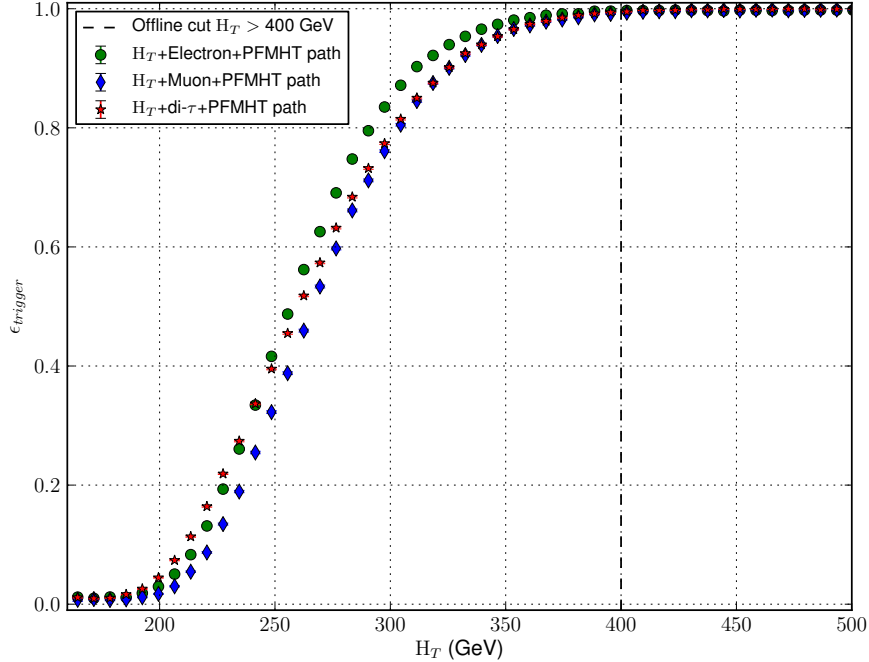
Figure 4.3.: Offline H_T turn-on in the 5×10^{32} cm^{-2} s^{-1} regime for all three trigger paths with $H_T > 200$ GeV in the denominator and $H_T > 250$ GeV in the numerator.

regime was evaluated using the `HLT_HT350_lepton_PFMHT45` in the numerator, and `HLT_HT300_lepton_PFMHT40` with an additional offline cut of $H_T > 450$ GeV. The performance is shown in figure 4.5b. The trigger turn-on is notably improved relative to the 5×10^{32} cm^{-2} s^{-1} regime, with greater than 98% efficiency being achieved at 90 GeV.

Lepton Request

The lepton requests of the triggers are investigated using events in the H_T dataset defined by purely hadronic triggers, with offline $H_T > 400$ GeV and pfMET > 120 GeV and at least one reconstructed offline lepton.

The efficiency of the online lepton cut is evaluated using the events which pass any trigger with the same lepton request as the numerator and is calculated with respect to the offline p_T of the lepton. In the case of the di–τ trigger, the second τ in p_T ordering is taken.

The quality criteria of the offline leptons is relaxed to increase the number of events passing the trigger. This causes the efficiency to plateau lower than 100%. In the case of
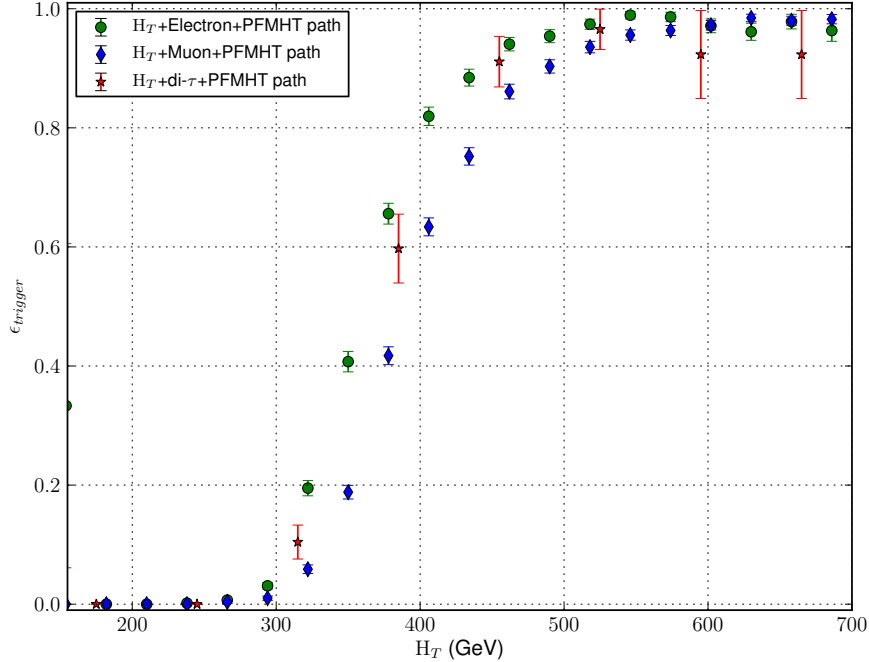
Figure 4.4.: Offline H_T turn-on in the $1 \times 10^{33}\ \mathrm{cm}^{-2}\ \mathrm{s}^{-1}$ regime for all three trigger paths with $H_T > 250$ GeV in the denominator and $H_T > 350$ GeV in the numerator. This set of trigger paths (with $H_T > 350$ GeV) was not used in the presented analysis.

the electrons and muons the criteria are only slightly relaxed giving plateau efficiencies of $> 90\%$. The τ isolation and identification are significantly relaxed due to the very limited number of events passing these triggers. As a result the efficiency plateaus at $\sim 30\%$. The plateau behaviour in the τ request is cross–checked in a τ + isolated muon ($\mathrm{p}_T > 12$ GeV) trigger which implements an identical online τ reconstruction algorithm as that used in the presented SSDL triggers and requests an online $\mathrm{p}_{T_\tau} > 20$ GeV. The offline performance of this cross–check trigger is shown in figure 4.7a for an offline selection requiring a looser τ isolation than that used in the SSDL analysis and demonstrates that the τ request reaches $\sim 95\%$ efficiency in offline p_T. A similar or better performance of the SSDL τ trigger request is assumed. The p_T value at which the efficiency becomes flat is then taken as 100% efficient in offline p_T. The values found are 8, 5 and 15 GeV for electrons, muons and τs respectively, as shown in figures 4.6a, 4.6b and 4.7b.
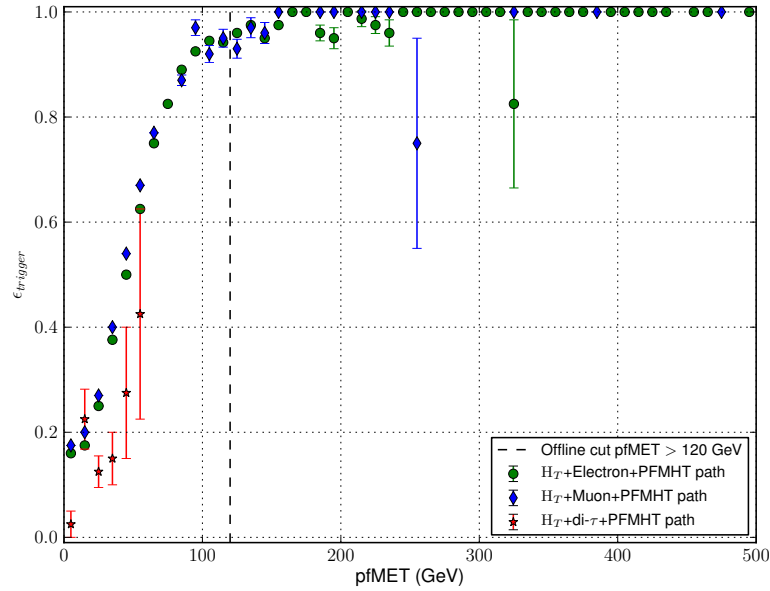
(a) pfMHT turn-on in the 5×10^{32} cm^{-2} s^{-1} regime.
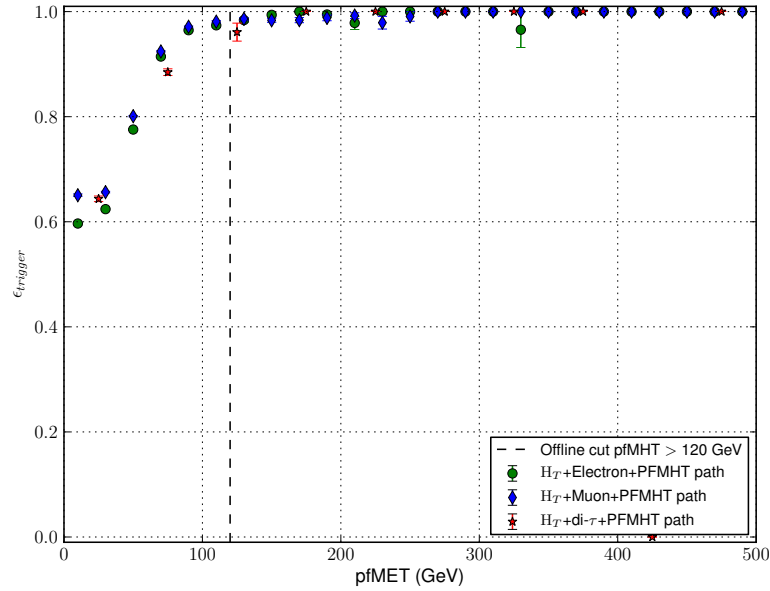
(b) pfMHT turn-on in the 1×10^{33} cm^{-2} s^{-1} regime.

Figure 4.5.: Offline pfMHT turn-on in the 5×10^{32} cm^{-2} s^{-1} and 1×10^{33} cm^{-2} s^{-1} regimes. A notable improvement in the performance is seen between the two due to improvements in the online PF implementation.
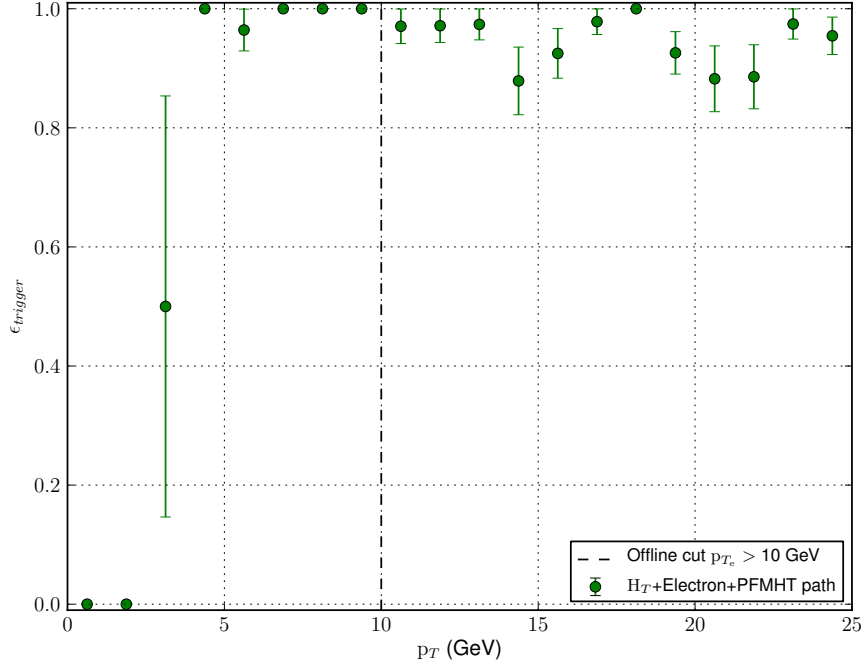
(a) Electron trigger offline p_T turn-on.
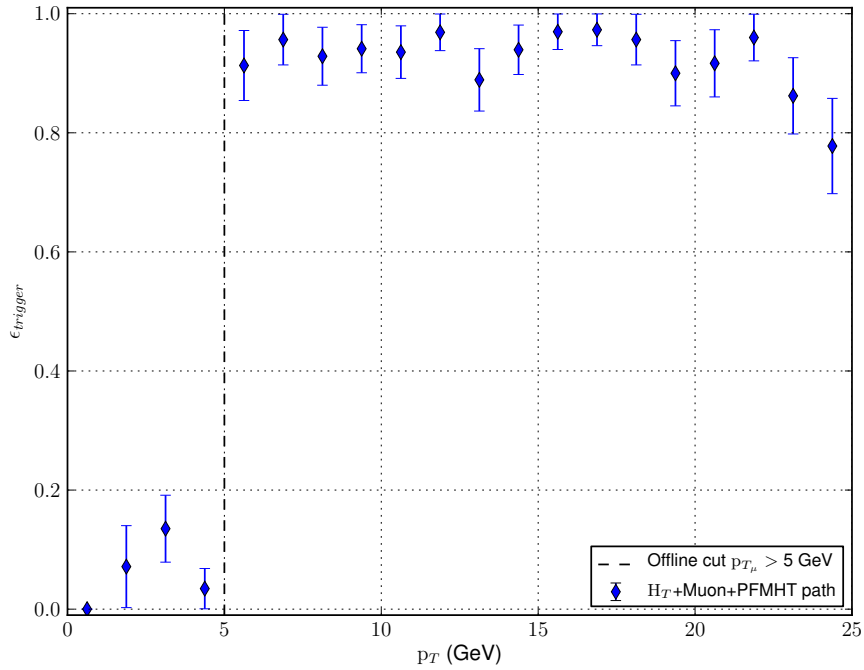
(b) Muon trigger offline p_T turn-on.

Figure 4.6.: Electron and muon trigger offline p_T turn-on. The triggers plateau at around 90% due to the relaxed post–trigger identification requirements. The value at which the efficiency becomes flat is taken to be 100% efficient and sets the value of the lowest possible offline p_T cuts.
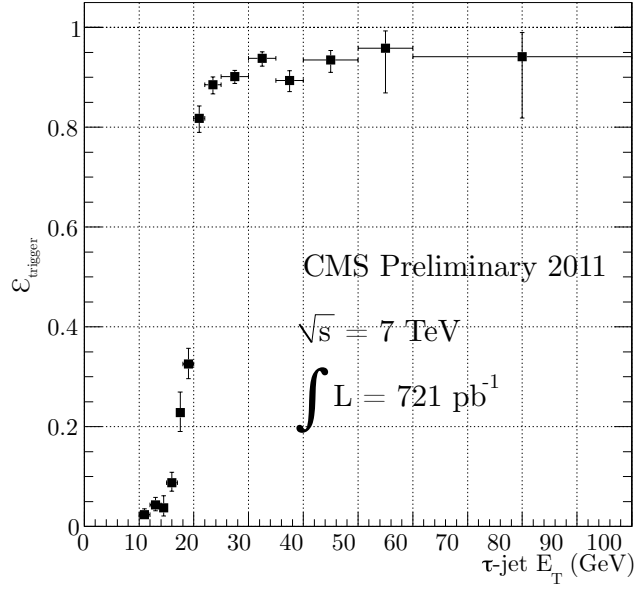
(a) Example τ trigger E_T turn-on. Taken from [83].
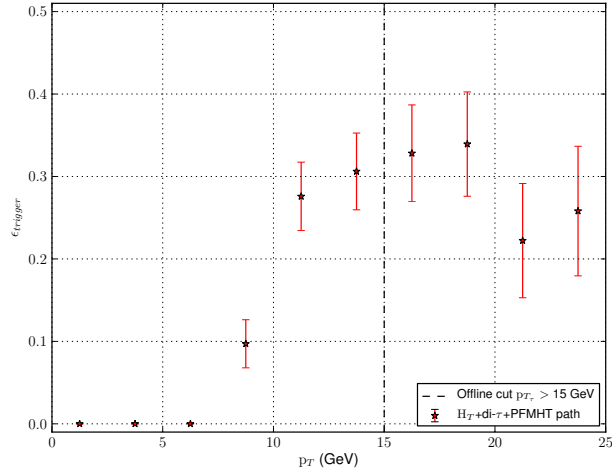
(b) SSDL τ trigger p_T turn-on.

Figure 4.7.: τ offline turn-on. Figure 4.7b shows the trigger p_T efficiency in the plateau is around 30% due to significantly relaxed τ identification criteria. The efficiency becomes flat at 15 GeV and the trigger request is taken to be $\sim 100\%$ efficient above this value. This assumption is made based on the offline E_T performance of a similar trigger shown in figure 4.7a.

4.2. Offline Selection

The 2011 SSDL SUSY search is performed in a region defined by the expected high hadronic activity and large E_T^{miss} associated with SUSY signal. The specific H_T and E_T^{miss} cuts are constrained by the trigger plateau regions.

The search region is defined with $H_T > 400$ GeV and $E_T^{miss} > 120$ GeV and is in accordance with the search region for the SSDL analysis using only light (e, μ) leptons. This region is expected to have very low SM background whilst being sensitive to regions of the CMSSM and provides a complementary search region to those used in the light lepton SSDL search discussed in section 6.1.2.

The charged leptons which pass the selections discussed below are ordered in p_T, and the first two taken as the SSDL candidates. If a third lepton is identified in the event, an additional Z^0–mass veto is applied for same–flavour and opposite–sign pairs to reduce background from Z+jet events. In addition, at least two jets are required in the event and the invariant mass of the SSDL pair is required to be greater than 5 GeV. Finally, at least one primary vertex is required.

The identification criteria for leptons, jets and missing energy are discussed below in sections 4.2.1 and 4.2.2 respectively. The signal event selection criteria used in the presented analysis is summarised in table 4.3.

The 2010 and 2011 datasets were analysed using different τ criteria. The differences where applicable are noted. The 2010 analysis is referred to for the background evaluation methods which were updated for the 2011 976 pb^{-1} analysis.

The previous 35 pb^{-1} analysis [81] defined a search region with $H_T > 350$ GeV and $E_T^{miss} > 50$ GeV. However, the triggers discussed in section 4.1 do not allow a fully efficient analysis with this search region definition. Nevertheless, a check is performed in a region defined by $H_T > 350$ GeV and $E_T^{miss} > 80$ GeV (which is 100% efficient in H_T and 90–95% efficient in E_T^{miss} for the first $\sim$795 pb^{-1}) for potentially missed signal and is shown to have no events above background. The object identification and background methods used are the same as those described below and in chapter 5. The details of this check may be found in appendix C.

4.2.1. Lepton Selection

The reconstruction of electrons, muons and hadronic τ with the CMS detector is described in chapter 3. The lepton selection is designed to probe the low–p_T part of a possible SUSY phase space. All leptons are required to be isolated. Relative isolation defined as the scalar sum of transverse track momenta, ECAL and HCAL deposits (excluding the contribution from the considered particle) divided by the considered particle transverse momentum is used to control the isolation of electrons and muons. These are both required to have a relative isolation of less than 0.15 within a cone of $\Delta R = 0.3$. τ isolation is controlled via specific PF–τ identification criteria. The following sections describe the identification applied to each object. A detailed list of the cuts and selection criteria may be found in appendix D.

Electron Identification and Selection

The electron selection used in the SSDL analysis is defined as being 80% efficient in identifying electrons produced in W $\rightarrow$ eν [75], as discussed in section 3.2 and requires $|\eta| < 2.4$ and $p_T > 10$ GeV. A stricter charge requirement is applied such that the charge of the electron is required to be consistent between CTF and GSF tracks, and the ECAL supercluster with respect to the silicon pixel tracker seed and the electron track. Electrons found within $\Delta R < 0.1$ of a muon are rejected to remove electrons originating from muon bremsstrahlung. Finally, fake electrons due to photon conversions are rejected by checking for the partner track in the conversion and requiring hits in the inner layers of the silicon pixel detector.

Muon Identification and Selection

Both tracker and global muons within $|\eta| < 2.4$ and with $p_T > 5$ GeV are considered [76]. The muon track is required to have a good χ^2 global fit with a minimum of 10 hits in the silicon tracker and have at least one valid stand alone hit in the muon chambers. The calorimeter deposits in both the ECAL and HCAL must be consistent with the MIP hypothesis.

τ Identification and Selection

Two identification definitions of τ, *loose* and *tight*, are used in the analysis. The *tight* definition is used as the selection criteria. The *loose* definition is used to predict the contribution from SM background events arising from jets faking τ.

Between the 2010 and 2011 data taking periods, the approved τ CMS identification procedure changed from TaNC to HPS. The initial (2010) *loose* and *tight* definitions were controlled using only shrinking cone τ, with the TaNC neural network output discriminant (see section 3.4) applied to define *tight*.

The presented 976 pb^{-1} analysis' τ identification criteria is described below. The identification for *loose* and *tight* τ is controlled by HPS reconstructed τs which are matched using a ΔR cone to shrinking cone τs.

Tight τ identification and selection:

Hadronically decaying τs are considered for $p_T > 15$ GeV and $|\eta| < 2.4$. The PF–τs are required to have one or three associated tracks and are required to be isolated such that no PF charged candidates with $p_T > 0.8$ GeV or PF–γ candidates with $E_T > 1.5$ GeV are present within a cone of $\Delta R = 0.5$. In addition, the τ candidate must satisfy muon and electron rejection criteria. If the leading track of the τ matches any muon chamber deposits it is rejected. Electron rejection is controlled using the output of the MVA described in section 3.4 which is required to be less than -0.1. Finally, no muons or electrons may be within $\Delta R < 0.1$ of the reconstructed τ. Technically, τ identification criteria are controlled by various binary discriminators [84] shown in appendix D.

Loose τ identification and selection:

The loose τ definition is based on the selection described above. All requirements are identical with the exception of the track multiplicity and isolation requirements which are removed.

4.2.2. Jets and E_T^{miss} Selection

PF–jets and E_T^{miss} are used throughout the analysis. The jets are clustered using the AK(0.5) algorithm [67] and are required to have $p_T > 40$ GeV and $|\eta| < 2.5$. They are corrected to account for the detector linearity and uniformity response. An additional correction is applied to account for the effects of PU as previously discussed in section 3.1.

Jets are required to have a neutral hadron fraction, neutral electromagnetic fraction and charged electromagnetic fraction individually less than 0.99. The charged hadron fraction is required to be greater than zero and the total number of constituents of the jet greater than one [85]. Finally, the jets are required to be at a distance $\Delta R > 0.4$ to the nearest muon or electron and $\Delta R > 0.1$ to the nearest τ. The offline H_T variable is defined as the scalar sum of the p_T of jets that pass these requirements. E_T^{miss} is reconstructed using PF as discussed in section 3.1. It is used without further correction and is referred to as pfMET.

4.3. Expected Results on Simulation

The MC samples used in this analysis were generated using MadGraph [86], Pythia [87] and Tauola [88]. They are presented with their names, processes, cross-sections and sample size in table 4.4. The generator used to process the sample is indicated by M (MadGraph), P (Pythia) and T (Tauola). The QCD samples are split into bins according to the underlying transverse momentum defined in the rest frame of the hard interaction.

The samples were reduced to private ntuples using a shared framework built on CMSSW [61]. The analysis of the ntuples was performed using a compiled ROOT based framework [89]. Figure 4.8 shows a good agreement between data and MC for key distributions. The data are selected using hadronic activity triggers with an online request of $H_T > 200$ GeV and offline $H_T > 400$ GeV and pfMET > 120 GeV. Offline H_T and pfMET are shown with an additional offline muon request.

The analysis selection above was performed on a set of MC samples weighted to 976 pb^{-1}. The results are presented in table 4.5. All errors shown are statistical. The total errors are evaluated as the quadrature sum of the errors in each considered process. Processes with zero event yield after the selection are shown with an error corresponding to one weighted event. These are not included in the total error.

As expected from the SSDL signal topology, most of the SM processes contribute a negligible background with the dominant sources coming from $t\bar{t}$ and W+jets processes. These sources of background may be estimated in data as discussed in chapter 5. An additional small irreducible contribution from SM processes producing same–sign isolated leptons in the final state is found in $W^{\pm}W^{\pm}$ type processes. The yield expected for the
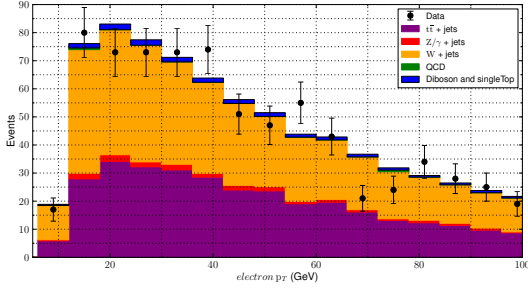
(a) Electron p$_T$ after H$_T$ and pfMET cuts.
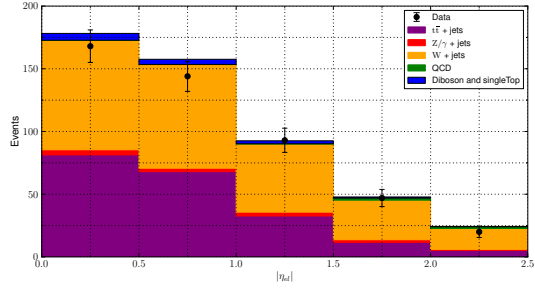
(b) Electron $|\eta|$ after H$_T$ and pfMET cuts.
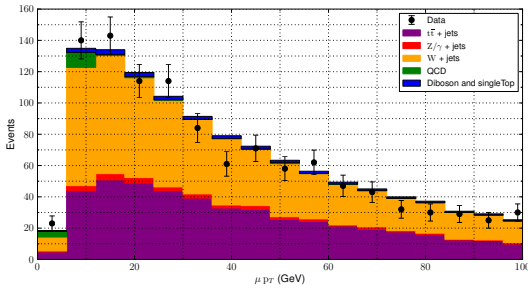
(c) Muon p$_T$ after H$_T$ and pfMET cuts.
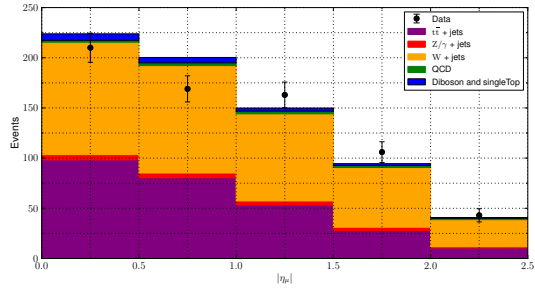
(d) Muon $|\eta|$ after H$_T$ and pfMET cuts.
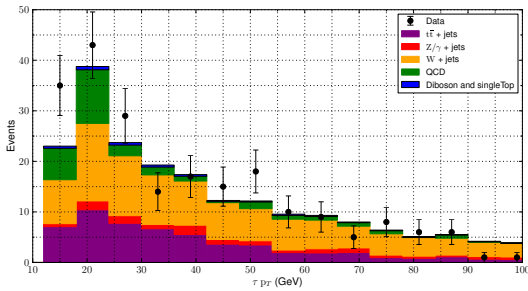
(e) τ p$_T$ after H$_T$ and pfMET cuts.
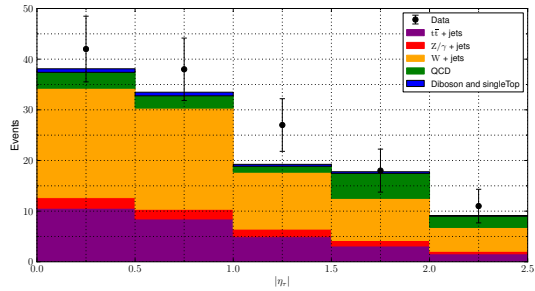
(f) τ $|\eta|$ after H$_T$ and pfMET cuts.
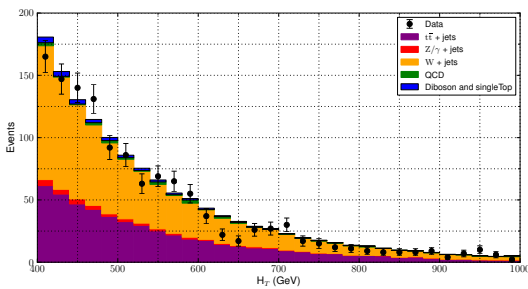
(g) H$_T$ after H$_T$ and pfMET and one muon request.
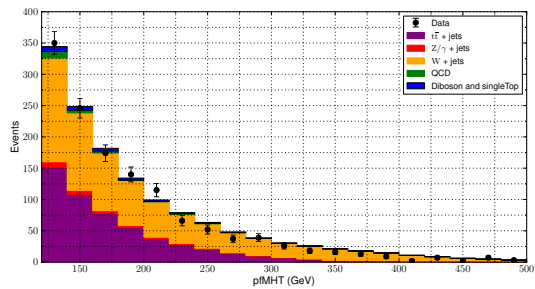
(h) pfMET after H$_T$ and pfMET and one muon request.

Figure 4.8.: Control plots showing the agreement between 976 pb^{-1} of data and correspondingly weighted MC for lepton p$_T$ and $|\eta|$, H$_T$ and pfMET after H$_T$ > 400 GeV and pfMET > 120 GeV requests.

LM6 signal point characterised by ($m_0 = 85$ GeV, $m_{1/2} = 400$ GeV, $A_0 = 0$, $\tan\beta = 10$ and $\mu > 0$) in the CMSSM parameter space is also shown. Whilst the background yield is significantly larger than the considered signal point, it is dominated by reducible SM processes.

The nature of the background MC events which pass the full selection (table 4.5) may be investigated via the generator leptons associated to the reconstructed leptons arising in the final state.

The reconstructed charged leptons are matched to their generator leptons using a $\Delta R < 0.3$ cone. The events are then categorised according to the origin of the generator leptons. A set of non–overlapping categories is used. The generator lepton is considered either *prompt* i.e. originating from SUSY particles or $W^{\pm}/Z$, or non–isolated, typically originating in the decay of heavy-flavour (HF) quarks. If a match to the reconstructed lepton is not found, it is classified as fake.

Tables 4.6 and 4.7 show this categorisation for the dominant SM backgrounds, $t\bar{t}$ +jets and W+jets. The events are organised according to the description above and additionally split according to which generator charged lepton is classified as *fake* or *prompt*. The terms *light* and *heavy* are used for this designation, and refer to the relative mass of the considered lepton pair. The *light/heavy* designation should be ignored for $\tau\tau$ final states.

As can be seen by this MC classification, the dominant contribution to background in all final states for both the $t\bar{t}$ and W+jets sample arises from one fake τ in the final state. Typically, the fake τ in question originates from a QCD jet in the event which passes the τ reconstruction and selection. The comparatively dominant contribution in the $\tau\mu$ channel of these backgrounds relative to the other channels is due to the higher probability of identifying one real, isolated muon in the event with respect to the other charged leptons.

Event selection	Lepton Identification	Jets
	Electrons:	
	$p_T > 10$ GeV, $|\eta| < 2.4$	
$H_T > 400$ GeV	Relative isolation < 0.15	
pfMHT> 120 GeV	GSF, CTF and SuperCluster charge consitency	
	Identification 80% efficient for W/Z electrons	
	No muons in $\Delta R < 0.1$	
	Muons:	
	$p_T > 5$ GeV, $|\eta| < 2.4$	
	Relative isolation < 0.15	
	Global track $\chi^2/n.d.f < 10$	
	Valid track hits > 10	
	Valid stand–alone hits > 0	
	τs:	
	$p_T > 15$ GeV, $|\eta| < 2.4$	$p_T > 40$ GeV, $|\eta| < 2.5$
	HPS τ discriminators:	
	(see appendix D)	No muons in $\Delta R < 0.4$
	ByDecay	No electrons in $\Delta R < 0.4$
	ByMediumIsolation	No τs in $\Delta R < 0.1$
	ByMediumElectronRejection	
	ByLooseMuonRejection	

Table 4.3.: Offline signal selection criteria and cuts. A complete description of all the cuts and definitions may be found in appendix D.

symbol	physics process	generator	$\sigma \times BR$ [pb]	generated N_{ev}	Luminosity pb^{-1}
W+jets	W($\to$ e, μ, τ)+jets	M, T	31314	15110974	482
Z+jets	Z($\to \ell^{\pm}\ell^{\mp}$)+jets	M, T	3048	2329439	764
t$\bar{\text{t}}$	t$\bar{\text{t}}$ + jets	M, T	157.5	1124208	7138
tW	tW + jets	M	10.6	489417	46171
Single Top, t channel	t + jets	M	63.0	484060	7683
Single Top, s channel	t + jets	M	4.6	494967	107601
WW	WW + jets	P, T	43	2061760	47947
ZZ	ZZ + jets	P	5.9	2108608	357931
WZ	WZ + jets	P	18.2	2108416	115847
W$^+$W$^+$ SPS	W$^+$W$^+$ + jets	M	0.3775	133747	354296
W$^-$W$^-$ SPS	W$^-$W$^-$ + jets	M	0.165	175075	1061060
W$^{\pm}$W$^{\pm}$ DPS	same–sign WW + jets	P	0.055085	200000	3630752
t$\bar{\text{t}}$ W	t$\bar{\text{t}}$ + W + jets	M	0.054	179998	3333296
QCD100-250	QCD, 250 > H$_T$ > 100 GeV	M	7×10^6	10266612	1.47
QCD250-500	QCD, 500 > H$_T$ > 250 GeV	M	1.71×10^5	4697363	27.5
QCD500-1000	QCD, 1000 > H$_T$ > 500 GeV	M	5200	7378686	1418
QCD1000-inf	QCD, H$_T$ > 1000 GeV	M	83	1707921	20577

Table 4.4.: MC samples used for the SSDL analysis. The results found in the τ channels considered are presented in table 4.5.

Sample	$e\tau$	$\mu\tau$	$\tau\tau$	Total
QCD100-250	0.00 ± 668.19	0.00 ± 668.19	0.00 ± 668.19	0.00 ± 668.19
QCD250-500	0.00 ± 35.68	0.00 ± 35.68	0.00 ± 35.68	0.00 ± 35.68
QCD500-1000	0.00 ± 0.69	0.00 ± 0.69	0.00 ± 0.69	0.00 ± 0.69
QCD1000-inf	0.00 ± 0.05	0.00 ± 0.05	0.05 ± 0.05	0.05 ± 0.05
W+jets	0.00 ± 2.03	2.03 ± 2.03	0.00 ± 2.03	2.03 ± 2.03
Z+jets	0.00 ± 1.28	0.00 ± 1.28	0.00 ± 1.28	0.00 ± 1.28
WZ	0.00 ± 0.01	0.00 ± 0.01	0.00 ± 0.01	0.00 ± 0.01
gamma+V+jets	0.15 ± 0.15	0.00 ± 0.15	0.00 ± 0.15	0.15 ± 0.15
$t\bar{t}$	0.69 ± 0.31	1.51 ± 0.46	0.14 ± 0.14	2.33 ± 0.57
WW	0.00 ± 0.02	0.00 ± 0.02	0.00 ± 0.02	0.00 ± 0.02
ZZ	0.00 ± 0.00	0.00 ± 0.00	0.00 ± 0.00	0.00 ± 0.00
SingleTop-schannel	0.00 ± 0.01	0.00 ± 0.01	0.00 ± 0.01	0.00 ± 0.01
SingleTop-tchannel	0.13 ± 0.13	0.00 ± 0.13	0.00 ± 0.13	0.13 ± 0.13
tW	0.00 ± 0.02	0.06 ± 0.04	0.00 ± 0.02	0.06 ± 0.04
W^+W^+ (SPS)	0.01 ± 0.01	0.03 ± 0.01	0.00 ± 0.01	0.04 ± 0.01
W^-W^- (SPS)	0.00 ± 0.01	0.01 ± 0.01	0.00 ± 0.01	0.01 ± 0.01
$W^{\pm}W^{\pm}$ (DPS)	0.00 ± 0.00	0.00 ± 0.00	0.00 ± 0.00	0.00 ± 0.00
$t\bar{t}$ W	0.02 ± 0.01	0.02 ± 0.01	0.00 ± 0.00	0.04 ± 0.02
Total Bkg	1.00 ± 0.37	3.66 ± 2.08	0.18 ± 0.15	4.84 ± 2.12
LM6	0.24 ± 0.02	0.34 ± 0.02	0.03 ± 0.01	0.61 ± 0.03

Table 4.5.: MC results for the SSDL τ channels using the search region selection ($H_T > 400$ GeV and pfMHT > 120 GeV) discussed in section 4.2 weighted to 976 pb^{-1}. The errors shown are statistical. Zero event yields are attributed an error corresponding to one weighted MC event. Total errors are evaluated as the quadrature sum of individual contributions excluding those with zero yield providing there is at least one non–zero contribution.

	2 fake	1 fake (heavy), 1 HF	1 fake (light), 1 HF	2 HF
$\tau\tau$	0.00	0.00	0.00	0.00
eτ	0.00	0.14	0.00	0.00
$\mu\tau$	0.55	0.00	0.00	0.00
	1 prompt, 1 fake (heavy)	1 prompt, 1 fake (light)	1 prompt (heavy), 1 HF	1 prompt (light), 1 HF
$\tau\tau$	0.00	0.14	0.00	0.00
eτ	0.55	0.00	0.00	0.00
$\mu\tau$	0.82	0.00	0.14	0.00

Table 4.6.: MC $t\bar{t}$ +jets background shown in table 4.5 categorised by the matched final state generator lepton.

	2 fake	1 fake (heavy), 1 HF	1 fake (light), 1 HF	2 HF
$\tau\tau$	0.00	0.00	0.00	0.00
eτ	0.00	0.00	0.00	0.00
$\mu\tau$	0.00	0.00	0.00	0.00
	1 prompt, 1 fake (heavy)	1 prompt, 1 fake (light)	1 prompt (heavy), 1 HF	1 prompt (light), 1 HF
$\tau\tau$	0.00	0.00	0.00	0.00
eτ	0.00	0.00	0.00	0.00
$\mu\tau$	2.03	0.00	0.00	0.00

Table 4.7.: MC W+jets background shown in table 4.5 categorised by the matched final state generator leptons.

Chapter 5.

Background Evaluation

Various sources of SM physics processes are expected to fake SUSY signal in the SSDL τ based channels from the MC studies discussed in section 4.3.

QCD events are characterised by jets in the final state. Typically the leptons and E_T^{miss} arise from instrumental mismeasurement, although leptons produced in the decay of heavy flavour hadrons may also pass the isolation requirements, faking the isolated lepton signal.

Electroweak processes producing W + jets may fake SSDL signals in the situation where a second lepton originates from instrumental background or from a real non–isolated lepton produced in a heavy flavour hadron decay (from one of the associated jets). Similarly, Z + jets production may fake a SSDL signal if there is a charge mismeasurement on one of the leptons produced in $Z^0 \rightarrow \ell^\pm \ell^\mp$ and E_T^{miss} produced due to jet mismeasurement. Alternatively, real E_T^{miss} may be produced via $Z^0 \rightarrow \nu\overline{\nu}$ with SSDL being produced from detector effects and/or faked from jets.

SSDL may be produced in $t\overline{t}$ + jets events. In the case of a semi leptonic decay, one of the leptons produced in the b–jets is mistakenly identified as isolated and is combined with the isolated lepton and E_T^{miss} from the W. This is generally the highest SM contribution to background across all SSDL including the light lepton channels.

Diboson production with jets is the only SM process which can produce true signal like events i.e. which don't involve any instrumental effects or bad isolation/charge reconstruction. These may arise through initial state $WZ/W^+W^-/ZZ$ decays with $W^\pm \rightarrow \ell^\pm \nu$ and $Z^0 \rightarrow \ell^+ \ell^-$.

In addition to the diboson processes discussed above, it is possible to produce same–sign W bosons via single or double parton scattering. In the case of single parton scattering, this process occurs at orders of at least α_{EW}^4 and $\alpha_{EW}^2 \alpha_{QCD}^2$ [90]. An example of the single parton scattering processes is shown in figures 5.1a and 5.1b.

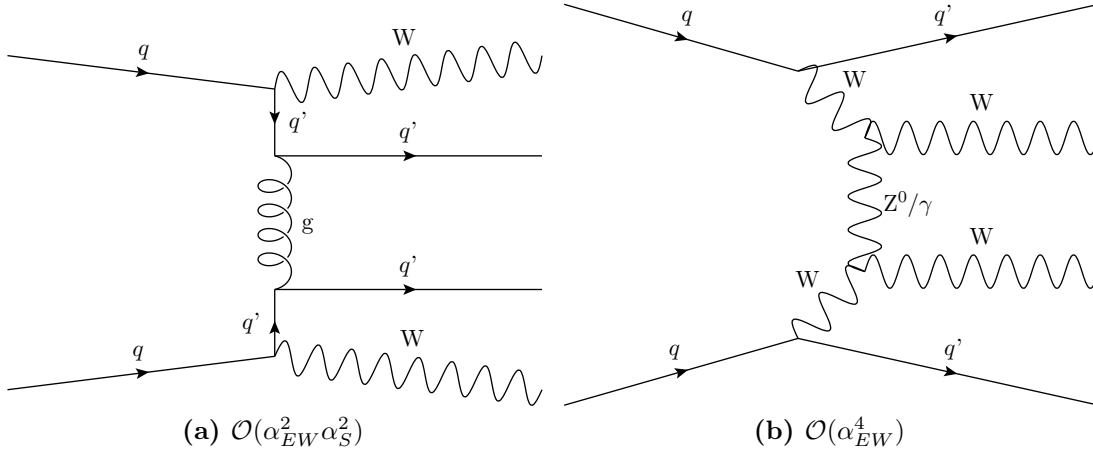**(a)** $\mathcal{O}(\alpha_{EW}^2 \alpha_S^2)$ **(b)** $\mathcal{O}(\alpha_{EW}^4)$

Figure 5.1.: Single parton scattering to same–sign WW. Two incident same charge quarks each radiate a W which are of same electric charge. The pair of W decay to SSDL and E_T^{miss} is produced via the associated neutrinos. Dijets are produced via the quarks following the W radiation. This process produces an irreducible SM background to the SSDL SUSY analysis.

Double parton scattering is currently a poorly understood phenomenon of hadron–hadron collisions, in which two partons of one hadron scatter with two partons of the second hadron. A description of this process may be found in [91].

Background for a general SSDL signal across all six final states may arise from either fake charged leptons or non–isolated leptons produced in b–jets. Electrons may be faked by the presence of a track produced by $\pi^\pm$ overlapping with a π^0 which decays to photons, or alternatively converted photons which pass the conversion rejection criteria. Faked muons may be produced in the decay of charged light mesons before their detection in the HCAL. Additionally, particles from QCD jets may 'punch–through' the HCAL (i.e. not be fully absorbed) and be identified in the muon chambers. Finally, non–isolated electrons and muons occurring in b–jets may also pass the identification requirements.

As shown in tables 4.6 and 4.7 the dominant contribution to background in SSDL eτ, $\mu\tau$ and $\tau\tau$ comes primarily from fake τs. This represents $\mathcal{O}(95\%)$ of all background as evaluated from simulation. All backgrounds arising from fake muons or electrons arising in the final state are therefore ignored and only the τ contributions are considered.

The following dominant contributions of background have been evaluated:

- 2 fake τs – these events arise primarily due to dijet QCD events.

- 1 fake τ associated with one real isolated light lepton (e/μ) – primarily due to $t\bar{t}$ and W + jets events. Other electroweak processes may contribute if an isolated charged lepton is not reconstructed.

- Charge mismeasurement of one of the τs. τ charge is measured as the sum of the charge of the hadrons present in the τ decay. If a background track is wrongly associated with the τ decay products, the charge may be incorrectly determined. Charge mismeasurement can also arise on either an electron or a muon. These rates were measured in 2010 in CMS data and have values at the 10^{-3} and 10^{-5} levels respectively [72, 76]. They are considered negligible compared to τ charge mismeasurement which is expected to occur at the $\mathcal{O}(10^{-2})$ level.

- Irreducible SM background. Single and double parton scattering producing WW (+jets) produce true SSDL in the final state.

The first three of these backgrounds are estimated using purely data–driven techniques. The contribution to the final signal observed in data from rare SM irreducible background is evaluated in MC. Triple electroweak boson production (e.g. WWW) is ignored.

The datasets used for the following analysis comprise the first 976 pb^{-1} of data collected at CMS. HLT trigger bits define the content of the datasets. Those used are the H$_T$ dataset which contains only hadronic and E$_T^{miss}$ activity triggers, the `ElectronHad` and `MuHad` datasets which contain triggers requesting hadronic activity and one or more electrons or muons respectively. Finally, the `TauPlusX` dataset is used which contains τ and one or more other objects. The above names are used when referring explicitly to a given data sample.

The SSDL triggers are included in the lepton based datasets. The H$_T$ dataset is used to measure the τ fake rate as discussed below. All data are processed in an analogous manner to the MC samples discussed in section 4.3. Data–MC agreement is shown in figure 4.8.

5.1. Standard Model Background Estimation

The following sections describe the data driven techniques used to estimate the background contributions from fake τ and τ charge misidentification.

5.1.1. Background from Fake τ

The background from fake τ is evaluated using a *tight–loose* method. The exact definition of *tight* and *loose* varies between the 2010 and 2011 analyses and is discussed in section 4.2.1.

A τ fake rate is defined in bins of $|\eta|$ and p_T as the probability of a *loose* τ passing the *tight* selection:

$$FR(p_T, |\eta|) = N_{tight}(p_T, |\eta|)/N_{loose}(p_T, |\eta|) \tag{5.1}$$

Only contributions from fake τ are considered in the evaluation of the background in the lepton $+ \tau$ channels based on the expected dominant source of fake leptons (τ) as confirmed in the results of the MC study shown in 4.3. The sample used to evaluate the τ fake rate is assumed to contain negligible numbers of real τs. To predict the number of background events in the eτ and $\mu\tau$ channels the following method is used. Considering $F_{\tau,l}(p_T, |\eta|)$ the number of background events from fake τ and $L_{l,\tau_{loose}}(p_T, |\eta|)$ the number of observed events with one good lepton (electron or muon) and one τ which passes the *loose* selection (and not *tight*), we can define the following:

$$F_{\tau,l}(p_T, |\eta|) = N^{true}_{l,\tau_{loose}}(p_T, |\eta|) \times FR(p_T, |\eta|) \tag{5.2}$$

$$L_{\tau,l}(p_T, |\eta|) = N^{true}_{l,\tau_{loose}}(p_T, |\eta|) \times (1 - FR(p_T, |\eta|)) \tag{5.3}$$

where $N^{true}_{l,\tau_{loose}}$ is the true number of events with one good lepton and one fake τ.

The number of observed background events from fake τs in a given $(p_T, |\eta|)$ bin, $F_{\tau,l}(p_T, |\eta|)$, can then be derived from equations 5.2 and 5.3 to be expressed in terms of

$L_{\tau,l}$ and the τ fake rate FR:

$$F_{\tau,l}(\mathrm{p}_T, |\eta|) = L_{\tau,l}(\mathrm{p}_T, |\eta|) \times \frac{FR(\mathrm{p}_T, |\eta|)}{1 - FR(\mathrm{p}_T, |\eta|)} \tag{5.4}$$

Finally, the total number of observed background events is evaluated by summing equation 5.4 over p_T and $|\eta|$:

$$F_{\tau,l} = \sum_{\mathrm{p}_T, |\eta|} F_{\tau,l}(\mathrm{p}_T, |\eta|) \tag{5.5}$$

$$= \sum_{\mathrm{p}_T, |\eta|} L_{\tau,l}(\mathrm{p}_T, |\eta|) \times \frac{FR(\mathrm{p}_T, |\eta|)}{1 - FR(\mathrm{p}_T, |\eta|)} \tag{5.6}$$

The background contribution in the $\tau\tau$ channel is evaluated in a manner analogous to the τe and $\tau\mu$ channels. For this channel the contribution of one or both τs being fake is considered.

The derivation is as follows:

$$F_{\tau_1,\tau_2}(\mathrm{p}_{T_1}, |\eta_1|, \mathrm{p}_{T_1}, |\eta_2|) \tag{5.7}$$
$$= N^{true}_{\tau_1^{loose}, \tau_2^{loose}}(\mathrm{p}_{T_1}, |\eta_1|, \mathrm{p}_{T_1}, |\eta_2|) \times FR(\mathrm{p}_{T_1}, |\eta_1|) FR(\mathrm{p}_{T_1}, |\eta_2|)$$
$$+ N^{true}_{\tau_1^{tight}, \tau_2^{loose}}(\mathrm{p}_{T_1}, |\eta_1|, \mathrm{p}_{T_1}, |\eta_2|) \times FR(\mathrm{p}_{T_1}, |\eta_2|)$$

where F_{τ_1,τ_2} is the number of background events in the $\tau\tau$ channel.

$$T_{\tau_1} L_{\tau_2}(\mathrm{p}_{T_1}, |\eta_1|, \mathrm{p}_{T_2}, |\eta_2|) \tag{5.8}$$
$$= N^{true}_{\tau_1^{loose}, \tau_1^{loose}}(\mathrm{p}_{T_1}, |\eta_1|, \mathrm{p}_{T_2}, |\eta_2|) \times (FR(\mathrm{p}_{T_1}, |\eta_1|)(1 - FR(\mathrm{p}_{T_2}, |\eta_2|)))$$
$$+ N^{true}_{\tau_1^{tight}, \tau_2^{loose}}(\mathrm{p}_{T_1}, |\eta_1|, \mathrm{p}_{T_2}, |\eta_2|) \times (1 - FR(\mathrm{p}_{T_2}, |\eta_2|))$$

$$L_{\tau_1} L_{\tau_2}(\mathrm{p}_{T_1}, |\eta_1|, \mathrm{p}_{T_2}, |\eta_2|) \tag{5.9}$$
$$= N^{true}_{\tau_1^{loose}, \tau_2^{loose}}(\mathrm{p}_{T_1}, |\eta_1|, \mathrm{p}_{T_2}, |\eta_2|) \times (1 - FR(\mathrm{p}_{T_1}, |\eta_1|))(1 - FR(\mathrm{p}_{T_2}, |\eta_2|))$$

where $T_{\tau_1}L_{\tau_2}$ is the number of observed events with strictly one *loose* and one *tight* τ. Similarly $L_{\tau_1}L_{\tau_2}$ represents the number of observed events with two *loose* τs. Again, $N_{\cdots}^{true}$ is the true number of events of a given background type and is unknown.

The number of background events in the $\tau\tau$ channel (F_{τ_1,τ_2}) can be expressed from a combination of equations 5.7, 5.8 and 5.9 as:

$$
\begin{aligned}
F_{\tau_1,\tau_2} = \sum_{\mathrm{p}_{T_1},|\eta_1|,\mathrm{p}_{T_2},|\eta_2|} & T_{\tau_1}L_{\tau_2}(\mathrm{p}_{T_1},|\eta_1|,\mathrm{p}_{T_2},|\eta_2|) \times \frac{FR(\mathrm{p}_{T_2},|\eta_2|)}{1-FR(p_{T_2},|\eta_2|)} \\
& - L_{\tau_1}L_{\tau_2}(\mathrm{p}_{T_1},|\eta_1|,\mathrm{p}_{T_2},|\eta_2|) \times \frac{FR(\mathrm{p}_{T_1},|\eta_1|)}{1-FR(\mathrm{p}_{T_1},|\eta_1|)} \times \frac{FR(\mathrm{p}_{T_2},|\eta_2|)}{1-FR(\mathrm{p}_{T_2},|\eta_2|)}
\end{aligned}
\tag{5.10}
$$

5.1.2. τ Fake Rate Measurement

The τ fake rate $FR(\mathrm{p}_T,|\eta|)$ is measured in the H_T dataset from events with one *loose* τ and no electrons or muons. The H_T datasets are expected to contain primarily QCD multi–jet events. The measurement is performed in two different H_T regions: $150 < \mathrm{H}_T < 300$ GeV and $\mathrm{H}_T > 300$ GeV. The first of these regions is used to check for robustness and systematics. In order to gather a sufficiently large sample size, no specific trigger was applied in this region. The second region used a prescaled hadronic trigger ($\mathrm{H}_T > 250$ GeV with prescale 500) and defines the baseline τ fake rate measurement.
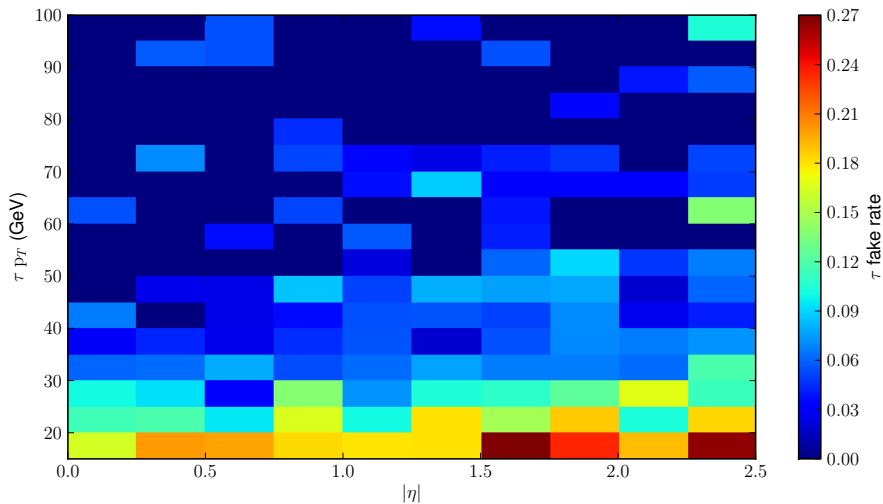
Figure 5.2.: τ fake rate measured in the $\mathrm{H}_T > 300$ GeV region, in the $(\mathrm{p}_T, |\eta|)$ plane.

Figure 5.2 shows the measured τ fake rate in the $\mathrm{H}_T > 300$ GeV region as a function of p_T and $|\eta|$. Figure 5.3 shows the comparison to the fake rate measured in the

$150 < \text{H}_T < 300$ GeV region after rebinning by a factor of four and five in $|\eta|$ and p_T respectively for two $|\eta|$ projections. The measured fake rate is demonstrated to be robust to the hadronic environment in which it is evaluated.
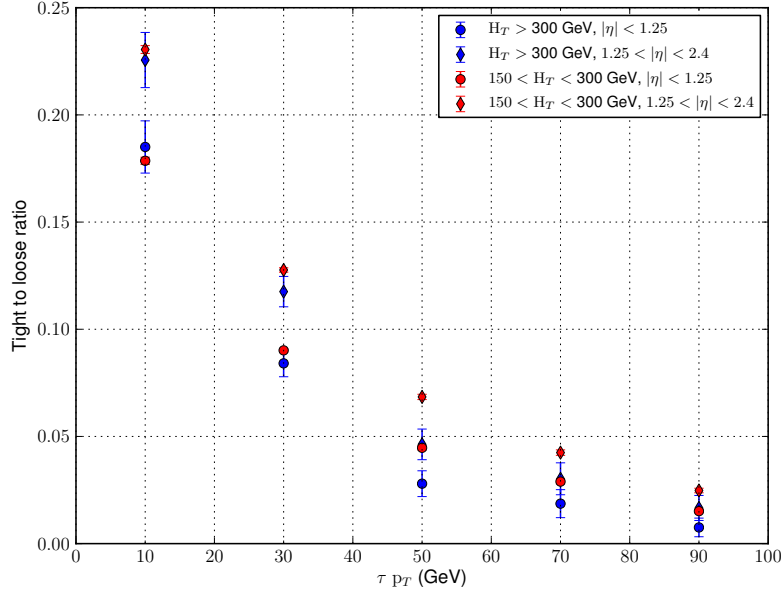

Figure 5.3.: τ fake rate measured in 850 pb^{-1} in two regions. $150 < \text{H}_T < 300$ GeV (*red*) and $\text{H}_T > 300$ GeV (*blue*). A good agreement between the two regions shows that the fake rate is robust to the amount of hadronic activity in the event.

The fake rate is also measured in MC using the generator information to demonstrate that it is robust between gluon–jet (QCD dominated events) and quark–jet (t$\bar{\text{t}}$ events) environments. This is shown in figure 5.4 for identical binning and projections as used in figure 5.3.

5.1.3. Closure Tests of Background Evaluation

The background evaluation method is tested for closure in a region ($\text{H}_T > 150$ GeV and pfMET < 50 GeV) with significantly higher statistics and a different topology in terms of hadronic activity and missing energy to the signal region.

The choice of H_T and pfMET cuts for the closure test region is motivated by considering a region dominated by SM processes, in which little or no SUSY signal is expected. A good agreement is therefore expected between the prediction and the observation.

The τ fake rate used for the closure test is as evaluated in section 5.1.2. The normalisation for the expectation in the eτ, $\mu\tau$ and $\tau\tau$ as well as the observed number of events which passed the full selection were evaluated in the `ElectronHad`, `MuHad` and `TauPlusX` datasets respectively.

The agreement between the predicted number of events and total number of events in the closure region is good in all channels, as shown in table 5.1. The errors shown are statistical errors from the combination of the τ fake rate and the normalisation factor errors. The error on the total number of predicted events is taken as the quadrature sum of the errors in the individual channels.

	eτ	$\mu\tau$	$\tau\tau$	Total
Predicted	62 ± 11	94 ± 12	19 ± 6	175 ± 17
Observed	44	83	23	150

Table 5.1.: Closure test of the background evaluation method in a region ($H_T > 150$ GeV and $pfMHT < 50$ GeV) away from the expected SUSY signal region and with higher statistics. Errors shown are statistical.
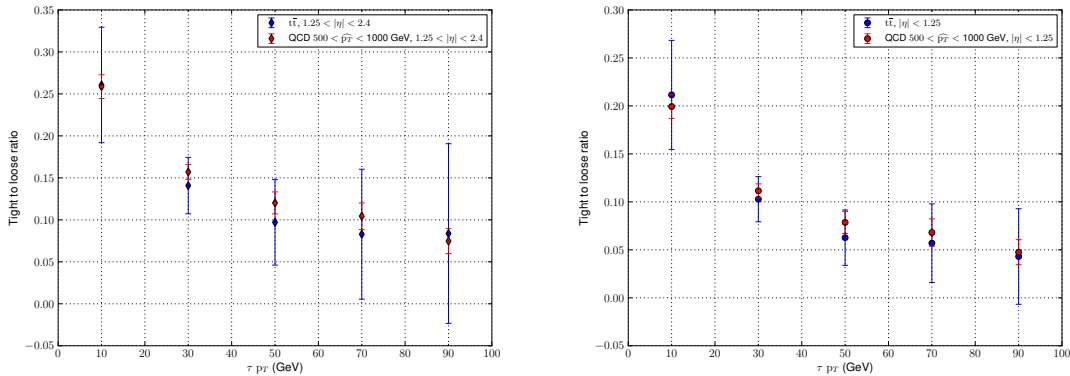

Figure 5.4.: τ fake rate measured in MC for QCD and t$\bar{t}$. The fake rate is shown to be robust to the nature (gluon/quark) of the jet environment.

5.1.4. τ Charge Mismeasurement

The τ charge mismeasurement rate is measured to be $\omega_\tau^{MC} = 3.0 \pm 0.1\%$ in MC from $Z \to \tau\tau$ events where the reconstructed τ is matched to the generator τ.

This measurement is also performed in data using a variation of the TP method used to measure τ reconstruction and identification efficiency discussed in section 3.4. $Z \to \tau(\to hadrons)\tau(\to \mu)$ events are selected and fixed templates for $Z \to \tau\tau$, $Z \to \mu\mu$, QCD and $W + $ jets are fitted to the invariant $\tau\mu$ mass where the τ and μ are of opposite or same charge. The fitting method on MC yields $\omega_\tau^{MCfit} = 2.9 \pm 2.6\%$ which agrees with the previous MC result found by matching to the generator leptons.

The fit is performed in data using the full 976 pb^{-1} available. 3004 ± 94 and 228 ± 34 $\tau\mu$ pairs are found with opposite and same–sign charges respectively. The results of the fit are shown for same and opposite charge $\mu\tau$ pairs in figure 5.5. The measured rate is found to be $\omega_\tau^{Data} = 7.1 \pm 1.0 \text{ (stat)} \pm 2.5 \text{ (syst)}\%$ where the systematic error contains a recommended 8% uncertainty assigned to the TP method, 5% from closure tests of the fit and 34% for the use of different QCD templates in the fit.

The number of events due to τ charge mismeasurement is then evaluated as:

$$N_{\tau\ell}^{mismeasured} = N_{\tau\ell}^{opposite\ charge} \times \frac{\omega_\tau^{Data}}{1 - \omega_\tau^{Data}} \tag{5.11}$$

$$N_{\tau\tau}^{mismeasured} = N_{\tau\tau}^{opposite\ charge} \times \frac{2\omega_\tau^{Data}(1 - w_\tau^{Data})}{(1 - \omega_\tau^{Data})^2 + \omega_\tau^{Data^2}} \tag{5.12}$$

The numbers of opposite–sign lepton–τ pairs used in the evaluation of the contribution to background from charge misidentification is found to be $N_{e\tau}^{opposite\ sign} = 5$, $N_{\mu\tau}^{opposite\ sign} = 5$ and $N_{\tau\tau}^{opposite\ sign} = 0$.

The numbers of predicted events due to mismeasured τ charges in each of the considered τ SSDL channels are shown in table 5.2 where errors shown are the combination of systematic and statistical error.
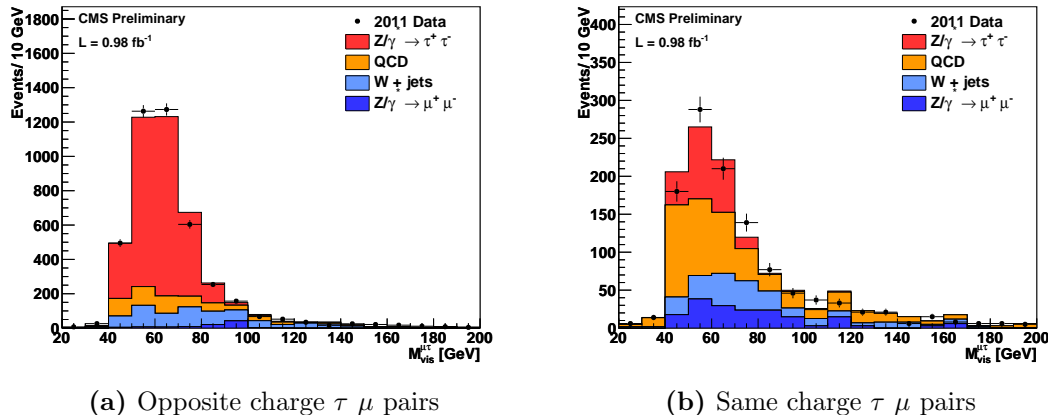
(a) Opposite charge $\tau\,\mu$ pairs

(b) Same charge $\tau\,\mu$ pairs

Figure 5.5.: Invariant mass distributions of $\mu\tau$ for opposite (5.5a) and same–sign (5.5b) charges, computed using the visible τ momentum. Data points and MC signal and background expectation is shown. The shapes of the signal and background are taken from MC and fitted to the data to determine their relative scales.

	eτ	$\mu\tau$	$\tau\tau$	Total
Predicted	0.4 ± 0.2	0.4 ± 0.2	0.0 ± 0.2	0.8 ± 0.3

Table 5.2.: Contribution to background in the signal region due to τ charge misidentification. Errors shown are the combination of systematic and statistical error.

5.2. Systematic Errors in the Background Evaluation

The possible sources of systematic error in the background contribution from fake τ are discussed in the following sections.

The measured fake rate $FR(\mathrm{p}_T, |\eta|) = N_{tight}(\mathrm{p}_T, |\eta|)/N_{loose}(\mathrm{p}_T, |\eta|)$ (see equation 5.1) could contain two possible sources of systematic error. Firstly, the τ fake rate is possibly sensitive to the environment in which it is evaluated, as quantified by the amount of hadronic activity, or H_T. This effect is measured by assessing the fake rate $FR(\mathrm{p}_T, |\eta|)$ in different H_T regions. Secondly, the baseline fake rate is evaluated for a given definition of *loose* τ. A different definition of *loose* τ is used to quantify the systematic error.

The total number of expected events due to fake τ is estimated after rebinning both the fake rate and the normalisation factor in $(p_T, |\eta|)$ prior to evaluating the final summation over p_T and $|\eta|$ (see equation 5.6). This procedure may also introduce a source of systematic error. The contribution in this case is estimated by rebinning and reevaluating the fake rate.

Finally the irreducible SM background contribution evaluated exclusively from MC is considered.

5.2.1. Fake Rate in Different Environments

The τ fake rate may show sensitivity to the environment in which it is evaluated, particularly if there are changes to the hadronic content of the events. The systematic error associated with the dependence on jets in the event is assessed by measuring the τ fake rate in the baseline region ($H_T > 300$ GeV) and comparing to the results found in a $150 < H_T < 300$ GeV region. The difference found between these two regions is taken as the systematic error on the predicted value of events due to the choice of environment. The predictions in the baseline region and $150 < H_T < 300$ GeV region are shown in table 5.3.

	eτ	$\mu\tau$	$\tau\tau$	Total
Predicted (baseline)	0.7 ± 0.1	1.3 ± 0.5	0.02 ± 0.03	2.02 ± 0.51
Predicted ($H_T > 150$ GeV)	0.8 ± 0.1	1.5 ± 0.5	0.00 ± 0.02	2.3 ± 0.51

Table 5.3.: τ fake rate is evaluated in the baseline and $150 < H_T < 300$ GeV region. The predicted number of events is then evaluated for each region. The difference in predicted number of events is taken as the systematic error.

5.2.2. Fake Rate with Different Fakeable Object Definitions

The fake τ definition is varied from the baseline definition shown and discussed in section 4.2.1 (no isolation requirements) to a definition which requires the τ to have no PF charged candidates with $p_T > 1.0$ GeV and no PF–γ with $E_T > 1.5$ GeV within the isolation cone ($\Delta R = 0.5$). This definition of *loose* is a tighter request than the baseline

definition of *loose* whilst still being loose with respect to the *tight–τ* definition shown in section 4.2.1.

The systematic error associated with this change of definition is taken as the absolute difference in predicted number of background events as evaluated using either definition of *loose* shown in table 5.4.

	eτ	$\mu\tau$	$\tau\tau$	Total
Predicted (baseline)	0.7 ± 0.1	1.3 ± 0.5	0.02 ± 0.03	2.02 ± 0.51
Predicted (*loose isolation*) τ	0.4 ± 0.1	2.6 ± 1.3	0.03 ± 0.03	3.03 ± 1.3

Table 5.4.: Predicted number of events evaluated from the baseline definition of fake τ and with a loosely isolated definition of fake τ.

5.2.3. Fake Rate with Different Binning in $(|\eta|, \mathrm{p}_T)$ Plane

The τ fake rate was rebinned from figure 5.2 in 5×5 bins as the baseline. In order to assess the systematic error associated with this procedure, the fake rate and prediction of number of events was evaluated using a different binning in $(\mathrm{p}_T, |\eta|)$ away from the baseline. The largest difference from the baseline is taken as the systematic error. The predicted number of events are shown in table 5.5.

	eτ	$\mu\tau$	$\tau\tau$	Total
Predicted (rebin = 2)	0.8 ± 0.1	1.3 ± 0.5	0.02 ± 0.02	2.12 ± 0.51
Predicted (baseline)	0.7 ± 0.1	1.3 ± 0.5	0.02 ± 0.03	2.02 ± 0.51
Predicted (rebin = 10)	0.9 ± 0.1	1.2 ± 0.4	0.00 ± 0.02	2.1 ± 0.41

Table 5.5.: Predicted number of background events with τ fake rate evaluated with the baseline definition before and after different binning in the $(|\eta|, \mathrm{p}_T)$ plane.

5.2.4. Systematic Errors Due to Irreducible SM Backgrounds

All contributions for the irreducible SM backgrounds are included in the predicted number of background events from the yield found in MC (see section 4.3). These contributions are shown in table 5.6.

Sample	$e\tau$	$\mu\tau$	$\tau\tau$	Total
WW	0.00 ± 0.02	0.00 ± 0.02	0.00 ± 0.02	0.00 ± 0.00
ZZ	0.00 ± 0.00	0.00 ± 0.00	0.00 ± 0.00	0.00 ± 0.00
WZ	0.00 ± 0.01	0.00 ± 0.01	0.00 ± 0.01	0.00 ± 0.00
W^+W^+ (SPS)	0.01 ± 0.01	0.03 ± 0.01	0.00 ± 0.00	0.04 ± 0.01
W^-W^- (SPS)	0.00 ± 0.00	0.01 ± 0.01	0.00 ± 0.00	0.01 ± 0.01
$W^\pm W^\pm$ (DPS)	0.00 ± 0.00	0.00 ± 0.00	0.00 ± 0.00	0.00 ± 0.00
ttW	0.02 ± 0.01	0.02 ± 0.01	0.00 ± 0.00	0.04 ± 0.02
Total Bkg	0.03 ± 0.02	0.06 ± 0.02	0.00 ± 0.00	0.09 ± 0.03

Table 5.6.: Irreducible background to the SSDL τ channels evaluated from MC in the search region. Errors shown are statistical. Zero event yields are attributed an error corresponding to one weighted MC event. Total errors are evaluated as the quadrature sum of individual contributions excluding those with zero yield.

A conservative 50% systematic error is assigned to the background evaluated from MC and is included in the final total errors on the total number of predicted events in the search region for each channel.

Chapter 6.

Results

The results shown concentrate on the SSDL τ channel analysis so far discussed. For completeness, a brief review and the central results of the light lepton SSDL analysis are also shown.

6.1. Signal Yields in Data and Predicted Numbers of Events

6.1.1. Results in the τ–Lepton Channels

The number of events found in the baseline normalisation regions $L_{\tau,l}(\mathrm{p}_T, |\eta|)$ as shown in equation 5.3 (section 5.1.1) for the background prediction method was as follows. For one loose τ and one tight light lepton (electron or muon) the normalisation values were eight events, 20 events and zero events in eτ, $\mu\tau$ and $\tau\tau$ respectively. Two events were found for loose τ with loose τ.

The signal events found in data are shown in a H$_T$–pfMET plane in figure 6.1. The hatched region defines the search region. Outside this region is below the trigger efficiency plateaus but is cross–checked in appendix C.

The results found in the search region are shown in table 6.1. The systematic errors shown on the fake τ contribution to the background estimation are calculated as the quadrature sum of the individual systematic errors, which are considered independent, as evaluated in section 5.2 for each individual channel. Errors in the irreducible background are shown with the 50% systematic uncertainty from evaluating this contribution in MC.
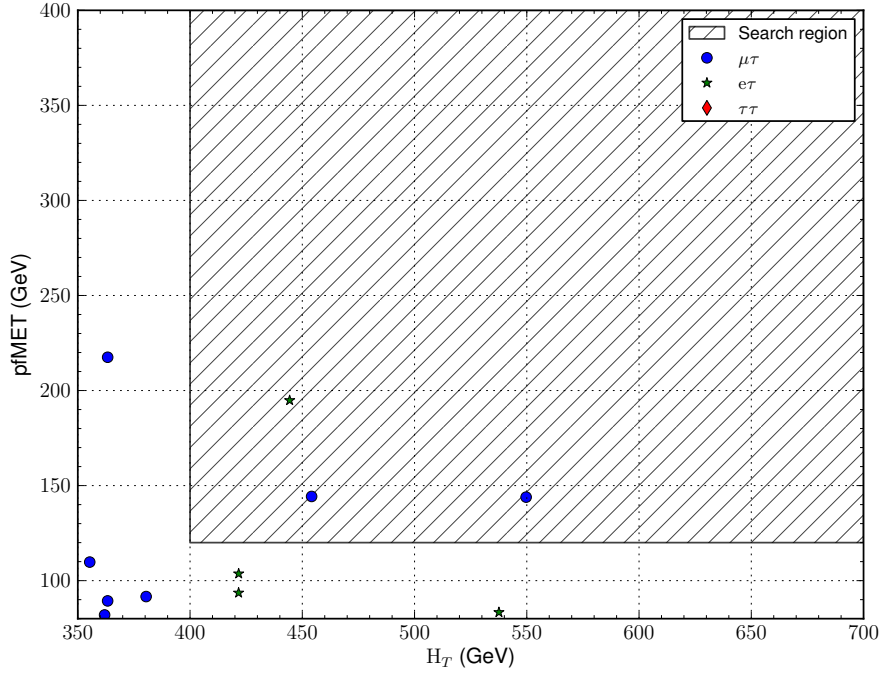
Figure 6.1.: Scatter plot of the τ SSDL events passing the full signal selection in data in the H_T–pfMET plane. The region outside the search region is below the trigger efficiency for the data taken in the 2×10^{33} cm^{-2} s^{-1} regime.

The systematic errors in the background evaluated from fake τ have a correlation across channels due the same τ fake rate (FR) being used in each channel. They are taken to be correlated in the total error for this background contribution and are summed linearly across the channels then added in quadrature with the statistical errors. The systematic errors in the charge misidentification discussed in section 5.1.4 are correlated across the three channels. The total error across all three channels is evaluated analogously to the error in the background from fake τ. Finally, the systematic error in the irreducible backgrounds is also correlated across the three channels. The total error is again evaluated similarly to above.

Total errors shown are calculated as the quadrature sum of the systematic and statistical error. The total error in the sum of all three channels is calculated as the quadrature sum of the total errors in the individual channels.

	$e\tau$	$\mu\tau$	$\tau\tau$	Total
Fake τ	0.7 ± 0.1 (stat.) ± 0.3 (syst.)	1.3 ± 0.5 (stat.) ± 1.3 (syst.)	0.02 ± 0.03 (stat.) ± 0.03 (syst.)	2.0 ± 1.7
Charge MisID	0.4 ± 0.2 (stat.) ± 0.1 (syst.)	0.4 ± 0.2 (stat.) ± 0.1 (syst.)	0.0 ± 0.2 (stat.) ± 0.0 (syst.)	0.8 ± 0.4
Irreducible Bkg	0.03 ± 0.02 (stat.) ± 0.02 (syst.)	0.06 ± 0.02 (stat.) ± 0.03 (syst.)	0.00 ± 0.00 (stat.) ± 0.00 (syst.)	0.09 ± 0.04
Total	1 ± 0.4	1.8 ± 1.4	0.0 ± 0.2	2.9 ± 1.7
Observed	1	2	0	3

Table 6.1.: Final τ SSDL results found in data with predicted and observed events for the $H_T > 400$ GeV and pfMET > 120 GeV region. The expected numbers of events are shown from the individual contributions considered in chapter 5 with statistical and systematic errors.
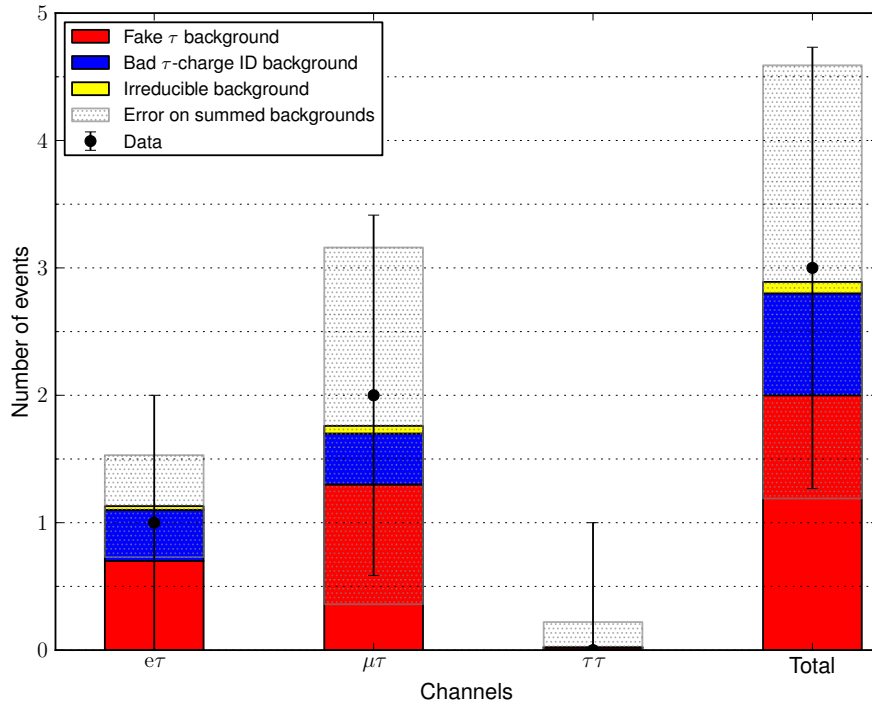

Figure 6.2.: τ SSDL channel yields in data and sums of individual background contribution.

6.1.2. Results of the Light Lepton Analysis

The results found in the non–τ channels of the all inclusive SSDL analysis are briefly discussed. A full description of these channels may be found in [81, 82].

The light lepton channels (ee, eμ and $\mu\mu$) are analysed in an inclusive dilepton closure region with $H_T > 200$ GeV and lepton identification as shown in section 4.2.1. Additionally, a second high lepton p_T region is defined with the requirement that at least one lepton has $p_T > 20$ GeV and the other lepton has $p_T > 10$ GeV. The high lepton p_T

region has a requirement of $H_T > 80$ GeV imposed by the required minimum number of jets. All other identification criteria are as discussed in section 4.2.1.

The background introduced by the presence of fake electrons and muons in these channels is evaluated primarily using a *tight–loose* method analogous to the background evaluation in the τ channels discussed in section 5, which defines *loose* based on isolation criteria.

The *tight–loose* method and alternative methods produce background estimations which agree within errors. A summary of the main results of the inclusive light lepton analysis, with background estimations is shown in table 6.2.

	ee	$\mu\mu$	eμ	Total
Background estimate	0.2 ± 0.1	0.9 ± 0.3	0.9 ± 0.3	2.0 ± 0.7
Observed	0	1	0	1

Table 6.2.: Final results of the inclusive light lepton analysis found in data with expected and observed events for the $H_T > 400$ GeV and pfMHT > 120 GeV region. The expected number of events includes the systematic and statistical error added in quadrature.

6.2. Interpreting the Results in SUSY Planes

The results presented in section 6.1 are interpreted in part of the CMSSM phase space and a Simplified SUSY Model Scan (SMS) favourable to τs in the final state.

6.2.1. Uncertainties in the Signal Yield

The uncertainty in the signal acceptance has several contributions. These are necessary to establish correctly the exclusion reach for any given model of NP [81, 82].

In order to quantify the SSDL search in a manner which allows investigation of any specific NP models without needing a full detector simulation, approximate reconstruction efficiencies are evaluated in MC and may be used to construct a simplified efficiency

model and constrain NP scenarios [81]. These efficiencies are shown and discussed in appendix A.

The efficiencies for the CMSSM and SMS scans presented in sections 6.2.2 and 6.2.3 are evaluated for each point in the scan.

Source	Uncertainty
Muon reco efficiency	5%
Electron reco efficiency	5%
Tau reco efficiency	10%
Isolation cut efficiency	5%
Trigger efficiency (H_T and pfMHT separately)	5%
H_T + pfMET cut efficiency	5%
Jet energy scale	7.5%
Luminosity	6%
ISR/FSR and PDF	20%
Total	27%

Table 6.3.: Uncertainties in the signal yield relevant to the τ SSDL analysis. The total error is the quadrature sum of the individual components.

The uncertainty in reconstruction efficiency at low p_T (5–20 GeV) for electrons and muons is measured in data to be 5%. An additional uncertainty of 5% is added per lepton to account for isolation efficiency as a function of hadronic activity in the event [82]. 10% uncertainty is assigned to τ reconstruction to account for the difference in data versus MC [79].

The hadronic JES has an associated uncertainty of 2–5% per jet [71,92]. PU contributes an additional 5% to this uncertainty. A further 5% is added to account for the difference in datasets used in the SSDL analysis and those used in [71,92]. Conservatively this amounts to a 7.5% uncertainty in jets for the SSDL analyses. The effect of this uncertainty on the signal yield in the τ SSDL channels is checked for consistency with the value of the JES uncertainty and is evaluated by scaling the jets in each event and recalculating

H_T and pfMHT. The variation in signal yield following this procedure is at most 5% for the LM6 benchmark. The uncertainty on the H_T and pfMET requirements due to the uncertainty on the JES is evaluated at 3% for LM6 benchmark events passing the full selection and is conservatively fixed at 5% to account for models with fewer high energy jets in the final state [82].

The luminosity delivered to CMS is measured in two ways [93]. The HF (described in section 2.2.3) data is used to extract the instantaneous luminosity using the average fraction of empty towers per bunch crossing. A second method is based on the rate of production of primary vertices. Luminosity measurement using these methods introduces an additional 6% uncertainty on the total integrated luminosity recorded by CMS [93].

Finally a 20% uncertainty on acceptance accounts for Initial State Radiation (ISR) and Final State Radiation (FSR) modelling as well as Parton Distribution Function (PDF) uncertainties taken from [94].

The contributions and total signal efficiency uncertainty in the τ SSDL channels are summarised in table 6.3. The total uncertainty of 27% is produced from the quadrature sum of the each individual uncertainty. This is taken as constant for models (or points in a model) of NP.

No signal above background is observed in any channel of the SSDL analysis. The observed 95% CL Upper Limit (UL) are compared to the yield in a CMSSM plane for the inclusive light lepton analysis and a τ favourable SMS for the τ channels.

The 95% CL UL are evaluated using a hybrid Frequentist–Bayesian method (CL_S) [78, 95, 96] to obtain a signal strength as the maximised ratio of signal+background to background. Efficiency and background uncertainties are modelled using log-normal distributions.

The UL found in the τ and inclusive light lepton SSDL channels, corresponding to the observed and predicted events in tables 6.1 and 6.2, are $UL_{\tau\,chan.}^{95\%\,CL} = 5.8$ and $UL_{incl.\,light\,lep.}^{95\%\,CL} = 3.0$ respectively.

6.2.2. Constrained Minimal Supersymmetric Standard Model

The results of the light lepton analysis are interpreted in a region of the CMSSM (see section 1.2.1) parameter space in a $(m_0, m_{1/2})$ plane with $\tan\beta = 10$, $A_0 = 0$ and positive

μ [82]. Each point with expected yields above the UL is considered excluded at the 95% CL. The result with 1 fb^{-1} is shown in figure 6.3.
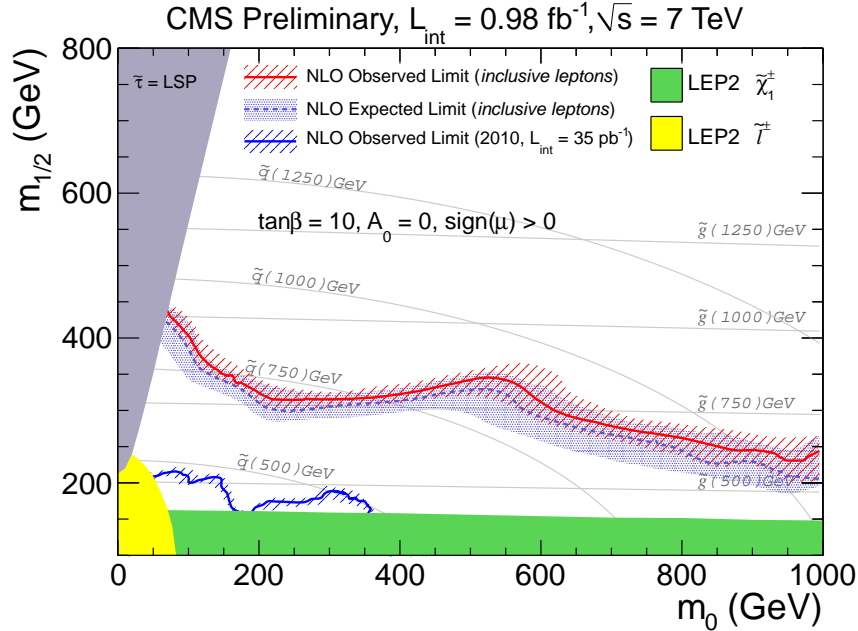

Figure 6.3.: Excluded region of CMSSM parameter space in the inclusive light lepton analysis. Expected and observed limits are shown with 1σ bands. The exclusion set in the 2010 analysis is also shown for comparison. All exclusions are calculated with next-to-leading order cross sections in the CMSSM scan. Taken from [82].

The UL in the τ channels is also shown in the CMSSM plane for completeness in figure 6.4. However, this particular model is not favourable to τ production in the final state, as can be clearly seen by the difference in reach between the inclusive light lepton curve and the τ SSDL curve. A preferred method for investigating the reach of the τ SSDL analysis is with the use of a SMS.

6.2.3. Simplified Models

In order to better quantify the scope of a search with respect to an effective model of NP it is useful to express results within the context of a Simplified SUSY Model Scan (SMS) [97, 98].

SMSs provide a model of interactions and final states described by a limited set of parameters of the complete (in this case SUSY) theory. As previously discussed, a general SUSY signature may be characterised by E_T^{miss} + jets (+ X), with X as a place holder for some additional requirement in the final state.
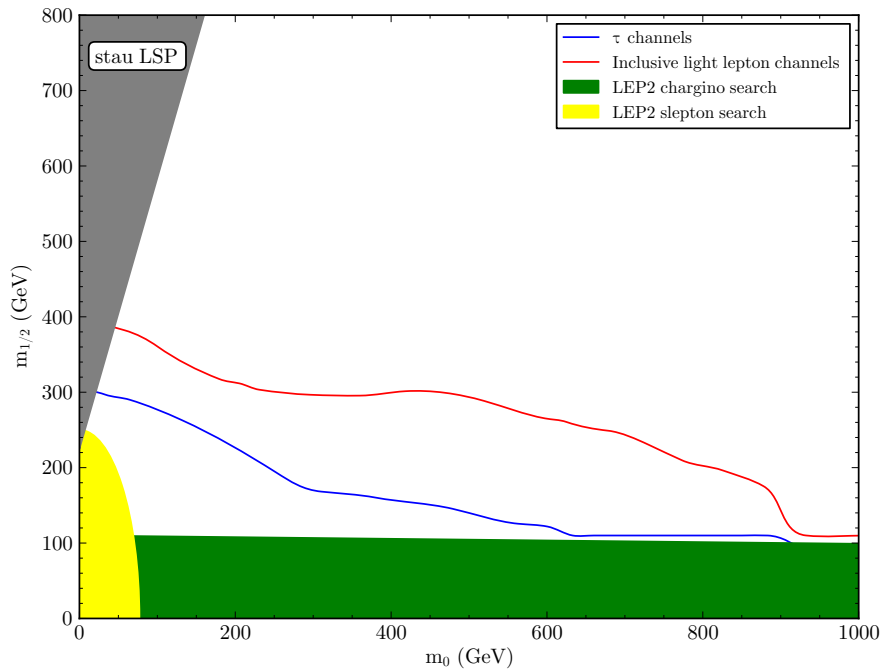
Figure 6.4.: Excluded region of identical CMSSM parameter space to figure 6.3 using the τ based SSDL channels. An approximate line for the light lepton analysis is included as a guide.

The models serve several purposes [99]. Search sensitivity across a large parameter space such as the MSSM (section 1.2.1), which is impractical to scan completely, may be performed in a consistent manner by describing only the content of the final state. In addition, they provide a framework for exploring models beyond the constraints of the usual MSSM – for example, with different mass ratios between the gauginos. This provides a powerful tool for investigating reconstruction and selection efficiencies as well as optimising search strategies to be general and cover all reachable regions of the parameter space.

In the event of positive signal, SMSs may provide a method to easily parameterise the observables in data. Alternatively, if no signal is present, limits set in SMSs may be translated to broader models.

A SMS with soft τs in the final state was used to explore the results found in the SSDL analysis. In this model, signals are produced with two low–p_T τs in the final state. These are of same–sign in 50% of the cases, and are allowed to decay via SM modes to leptons or jets with the usual branching fractions. A schematic representation of the decay mode is shown in figure 6.5.
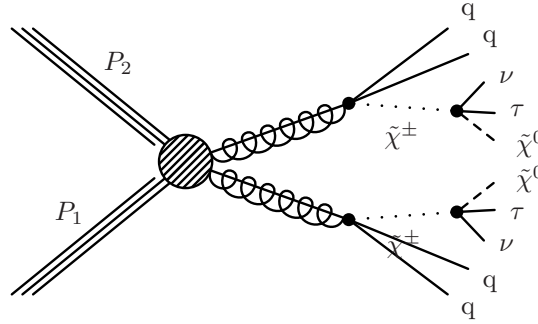
Figure 6.5.: Topology of the SMS model with τs in the final state.

The considered model has the following properties:

$$\text{pp} \to \widetilde{g}\widetilde{g}, \tag{6.1}$$

$$Br(\widetilde{g} \to \widetilde{\chi}^{\pm}_1 qq') = 100\%, \tag{6.2}$$

$$Br(\widetilde{\chi}^+_1 \to \widetilde{\chi}^0_1 \tau^+ \nu_\tau) = 100\%, \tag{6.3}$$

and is investigated in a $(0 < m_{\widetilde{g}} < 1200 \text{ GeV}, 0 < m_{LSP=\widetilde{\chi}^0_1} < 1200 \text{ GeV})$ plane. The region with $m_{LSP} > m_{\widetilde{g}}$ is unphysical.

The efficiencies are shown for each cut exclusively and for the total selection for the total scan (includes opposite–sign events and non τ channels) in figures 6.6, 6.7 and 6.8. Additionally, the lepton selection efficiency is shown after a generator selection for each considered final state (τe, $\tau\mu$ and $\tau\tau$). The efficiency in the lepton part of the selection is at a maximum of 4%, 10% and 12% for the $\tau\tau$, τe and $\tau\mu$ channels respectively. The combined efficiency of the lepton selection reaches a maximum of $\sim 3\%$. As expected, the efficiency is highest in the region of high $m_{\widetilde{g}}$/low m_{LSP} where the τ is produced with a large momentum.

The high $m_{\widetilde{g}}$/low m_{LSP} region also produces the hardest jets. Correspondingly the efficiency in the H_T request is highest in this region with a maximum of 90% as shown in figure 6.7c.

E_T^{miss} is measured as unbalanced transverse activity. The largest missing energy (note not E_T^{miss}) production is phenomenologically expected to occur when the mass of the LSP is nearly degenerate with the mass of the gluino. However, in this region the pairs of neutralinos are produced back to back with very little associated hadronic activity in

the event leading to a low efficiency in E_T^{miss} as shown around the diagonal $m_{\widetilde{g}} = m_{LSP}$ region in figure 6.7b. Conversely, the efficiency in the E_T^{miss} requirement increases as the LSP mass is reduced with respect to $m_{\widetilde{g}}$ due to this region containing hard unbalanced jets.

SMS Cross-section Limit

Figure 6.9 shows the cross-section limit in the SMS scan evaluated from the 95% C.L. upper limit on the observed number of events in the τ plus lepton SSDL analysis.

The cross-section limit is evaluated at each point as:

$$\sigma_{limit} = \frac{5.8}{\mathcal{L}(= 976 \text{ pb}^{-1}) \times \epsilon} \tag{6.4}$$

where the efficiency ϵ after the full signal selection is shown at each point in figure 6.8.

The cross-section limit is compared to next-to-leading order cross-sections for gluino production as calculated with Prospino [100] at each point in the plane.

The observed 95% CL UL on the cross-section as evaluated from equation 6.4 is shown in figure 6.9. Gluino masses below 400 GeV are excluded in the considered SMS for LSP masses up to 350 GeV with the exception of the region around $m_{\widetilde{g}} \approx m_{LSP}$. At lower LSP mass ($m_{LSP} < 100$ GeV), gluino masses of up to 620 GeV are excluded.
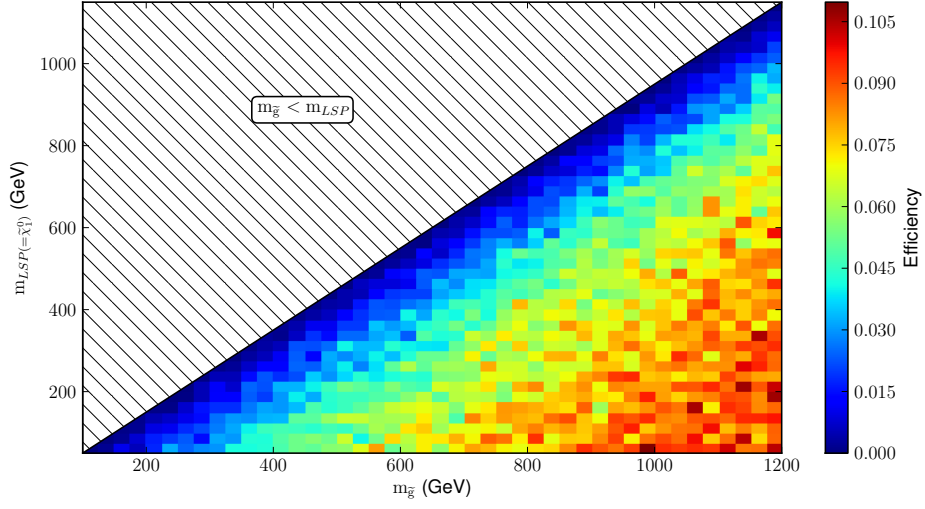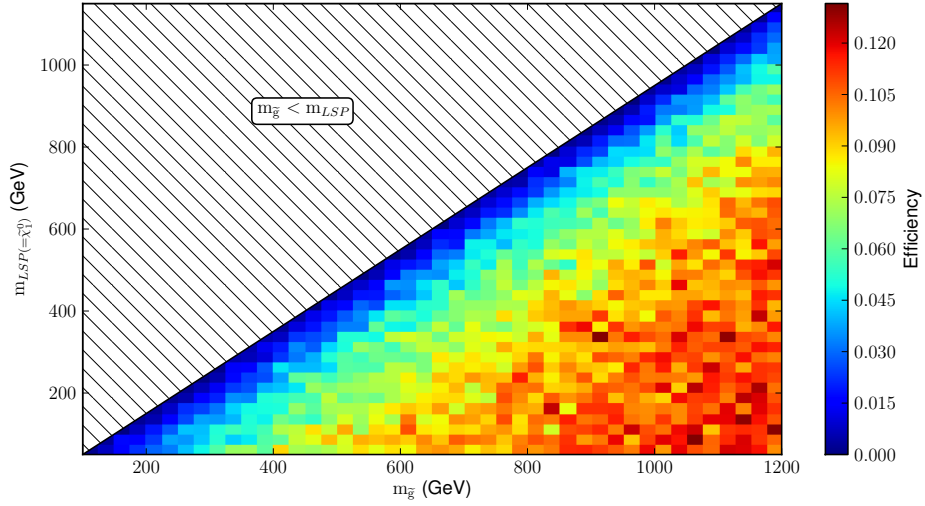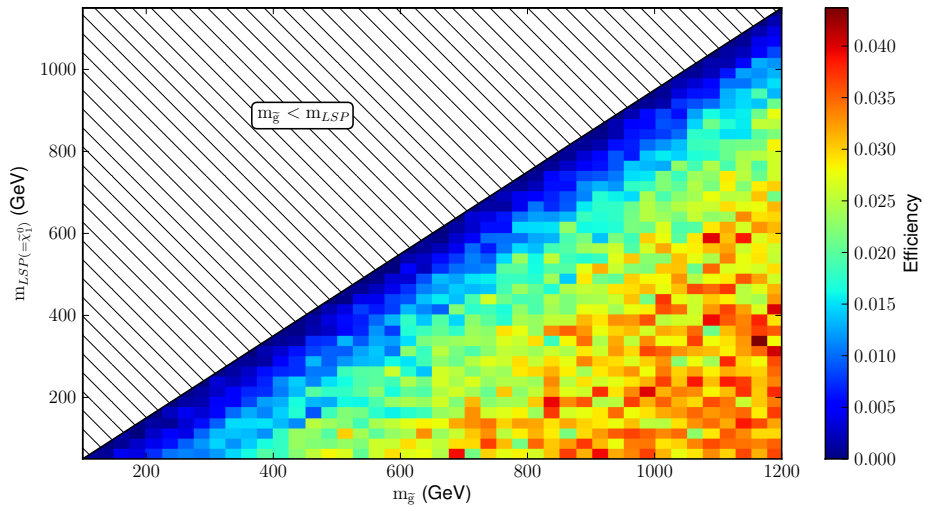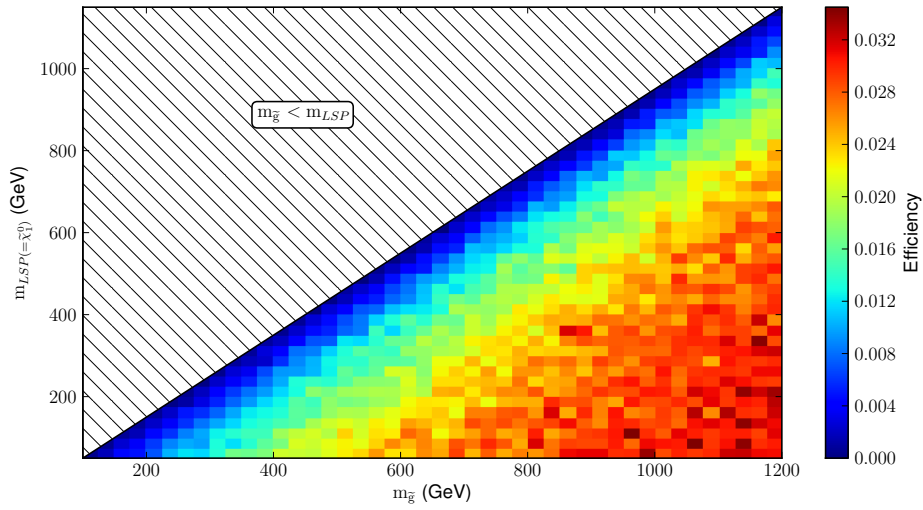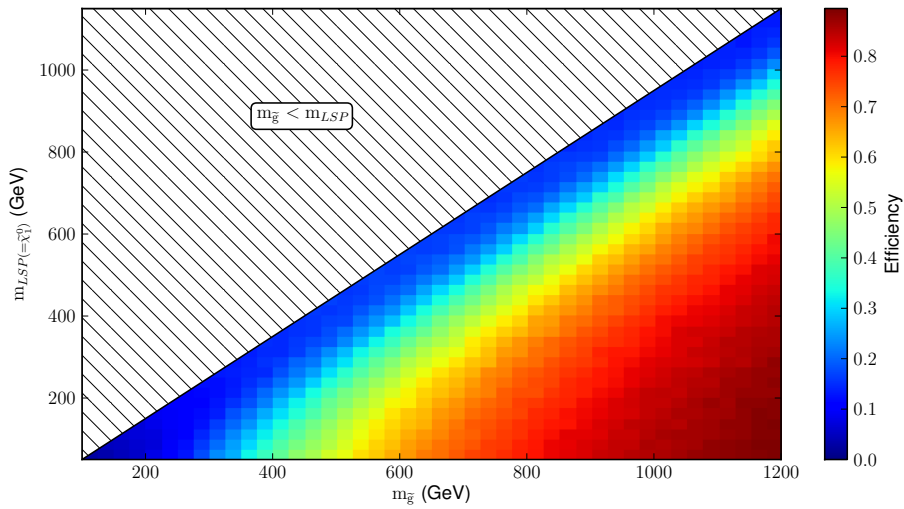
(a) Efficiency in same–sign τe after lepton selection.

(b) Efficiency in same–sign $\tau\mu$ after lepton selection.

(c) Efficiency in same–sign $\tau\tau$ after lepton selection.

Figure 6.6.: Same sign τ+lepton selection efficiency in same–sign eτ, $\mu\tau$ and $\tau\tau$ final states selected at MC generator level.

(a) Efficiency after same–sign lepton selection request in all events.

(b) Efficiency after E_T^{miss} request.
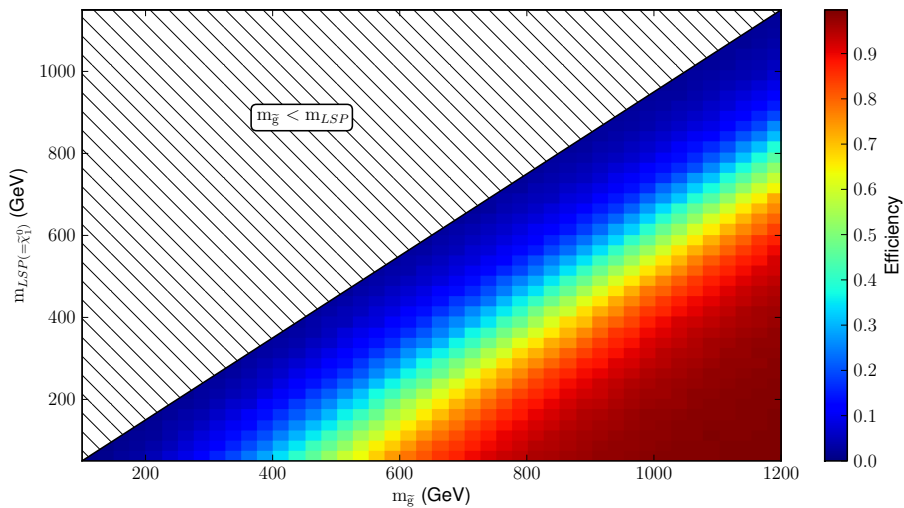
(c) Efficiency after jets and H_T request.

Figure 6.7.: Efficiencies for the full SSDL selection, pfMET and H_T requirements with respect to the full SMS.
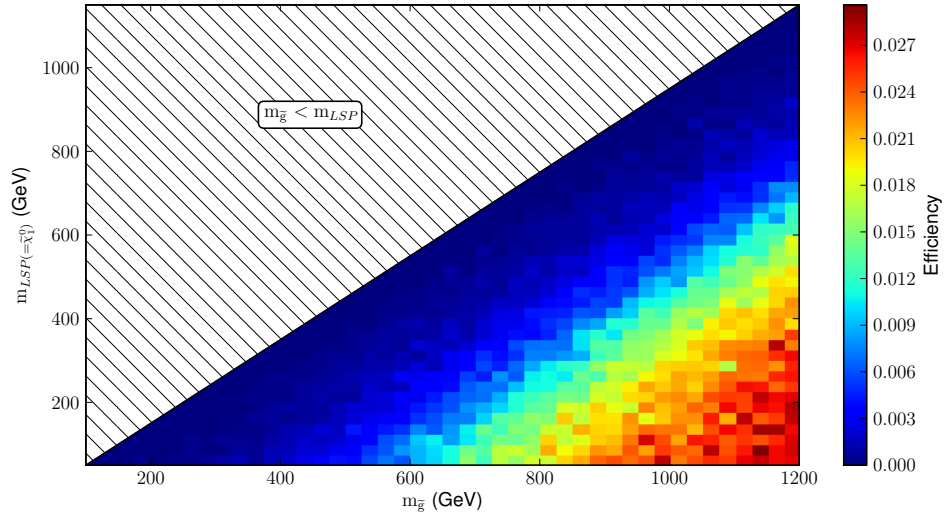
Figure 6.8.: Efficiency after the full signal selection in τ+lepton channels over the full SMS.
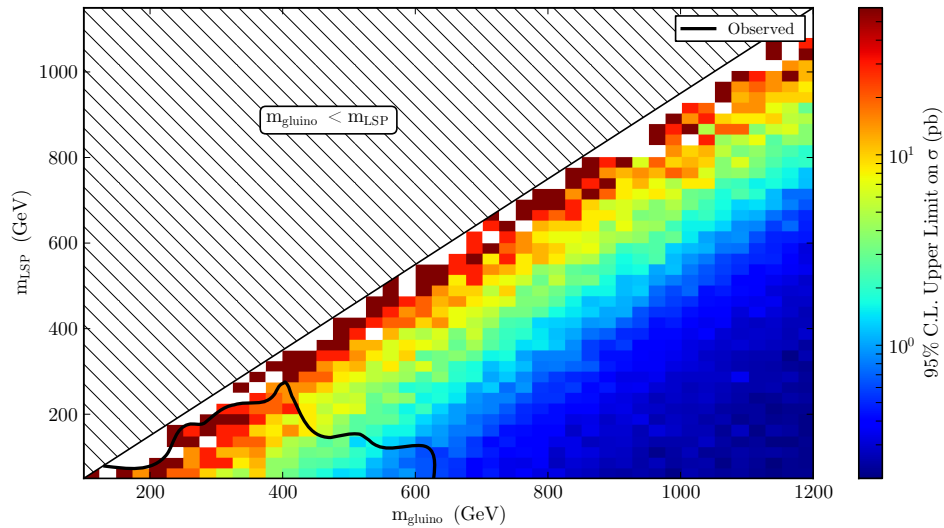

Figure 6.9.: Observed cross-section limit for the SMS scan based on the 95% C.L. UL of events observed in data with the τ plus lepton SSDL selection.

Summary and Conclusions

A search for Supersymmetry with Same–Sign Dileptons in the first 976 pb^{-1} of 7 TeV centre-of-mass energy pp LHC collision data collected at CMS was presented. A review of essential methods and results is shown below.

The SSDL channel provides a clean signature for early SUSY discovery with little contamination from SM processes. In addition, channels with τ occurring in the final state are favourable for certain regions of SUSY parameter space.

The τ channel (eτ, $\mu\tau$, $\tau\tau$) based SSDL search is performed using dedicated HLT triggers combining a H$_T$, E$_T^{miss}$ and lepton request, and exploits Particle Flow techniques at both trigger and reconstruction level. The search is focused on low lepton p$_T$ (5, 10 and 15 GeV for muons, electrons and τ respectively) in a search region with H$_T$ > 400 GeV and E$_T^{miss}$ > 120 GeV.

The dominant background contribution arises from fake τ in all three considered channels. This is evaluated using a *tight–loose* data driven technique based on measuring the τ fake rate in a different data sample to those used for the signal search, then normalising this rate to predict the total number of background events in the signal region. The method is shown to be robust and is tested for closure away from the signal region. Backgrounds arising from τ charge mismeasurement were estimated using a Tag and Probe analysis of Z $\rightarrow \tau\tau$. Finally, irreducible backgrounds from rare SM processes were evaluated from MC.

The expected numbers of observed and predicted events are summarised in table 6.4. A good prediction is found in each individual channel considered.

No signal above background was observed. The signal region yielded a total of three observed events for a background prediction of 2.9 ± 1.7 in the τ channels with a 95% CL UL on the observed number of events equal to 5.8.

	$e\tau$	$\mu\tau$	$\tau\tau$	Total	95% CL UL
Predicted	1.1±0.4	1.8±1.4	0.0±0.2	2.9±1.7	
Observed	1	2	0	3	5.8

Table 6.4.: Summary of final results found in data with predicted and observed events in the search region. The expected number of events in each channel is shown from the individual contributions considered in chapter 5 with statistical and systematic errors.

The results for the SSDL analysis were interpreted in a set of SUSY models. The light lepton analysis results were used to exclude a section of the CMSSM parameter space. This particular CMSSM model was shown to be unfavourable to τ channels and therefore, the results of this analysis were interpreted in a τ favourable Simplified SUSY Model Scan (SMS). The considered SMS is characterised by gluino pair production which decays to quarks, τs and a LSP in the final state. A 95% CL limit on the production cross-section excludes gluino masses below 400 GeV for LSP masses up to 350 GeV (with the exception of the region around $m_{\widetilde{g}} \approx m_{LSP}$) and gluino masses up to 600 GeV for LSP masses below 100 GeV.

Appendix A.

Generator Efficiencies for Constraints on New Physics

An approximate efficiency model of the SSDL analysis may be constructed for investigation of a chosen NP scenario from basic efficiencies for the principal objects used in the analysis [81, 82]. The efficiencies shown in figure A.1 are derived in MC from the signal point LM6.

The lepton efficiencies may be expressed as a function of p_T by:

$$\epsilon_{high}\text{erf}[(p_T - C)/\sigma] + \epsilon_C 1 - \text{erf}[(p_T - C)/\sigma] \tag{A.1}$$

for electrons and muons and:

$$\epsilon_{high}(1 - e^{-\alpha(p_T - C)}) \tag{A.2}$$

for τs. ϵ_{high} is the efficiency in the plateau at high momentum. For muons and electrons at $p_T = C$, the efficiency has a value of ϵ_C. σ controls the rate of the efficiency turn on for electrons and muons whilst α controls the turn on for τ. The values of these parameters are $C(\text{GeV}) = 5(10)$, $\epsilon_C = 0.24(0.19)$, $\epsilon_{high} = 0.74(0.68)$ and $\sigma(\text{GeV}) = 15(19)$ for muons (electrons). The τ parameters are 0.34, 0.052 and 15 GeV for ϵ_{high}, α and C respectively.

Similarly the H_T and E_T^{miss} efficiencies may be characterised by:

$$0.5\epsilon_{high}\text{erf}(x - x_{1/2})/\sigma] + 1 \tag{A.3}$$

with ϵ_{high} the efficiency at generator value x of H_T or E_T^{miss}, $x_{1/2}$ the position of half-plateau efficiency and σ the width of the efficiency turn on. The values of these parameters for

(a) τ reconstruction efficiency.

(b) Electron and muon reconstruction efficiency.

(c) H_T reconstruction efficiency.
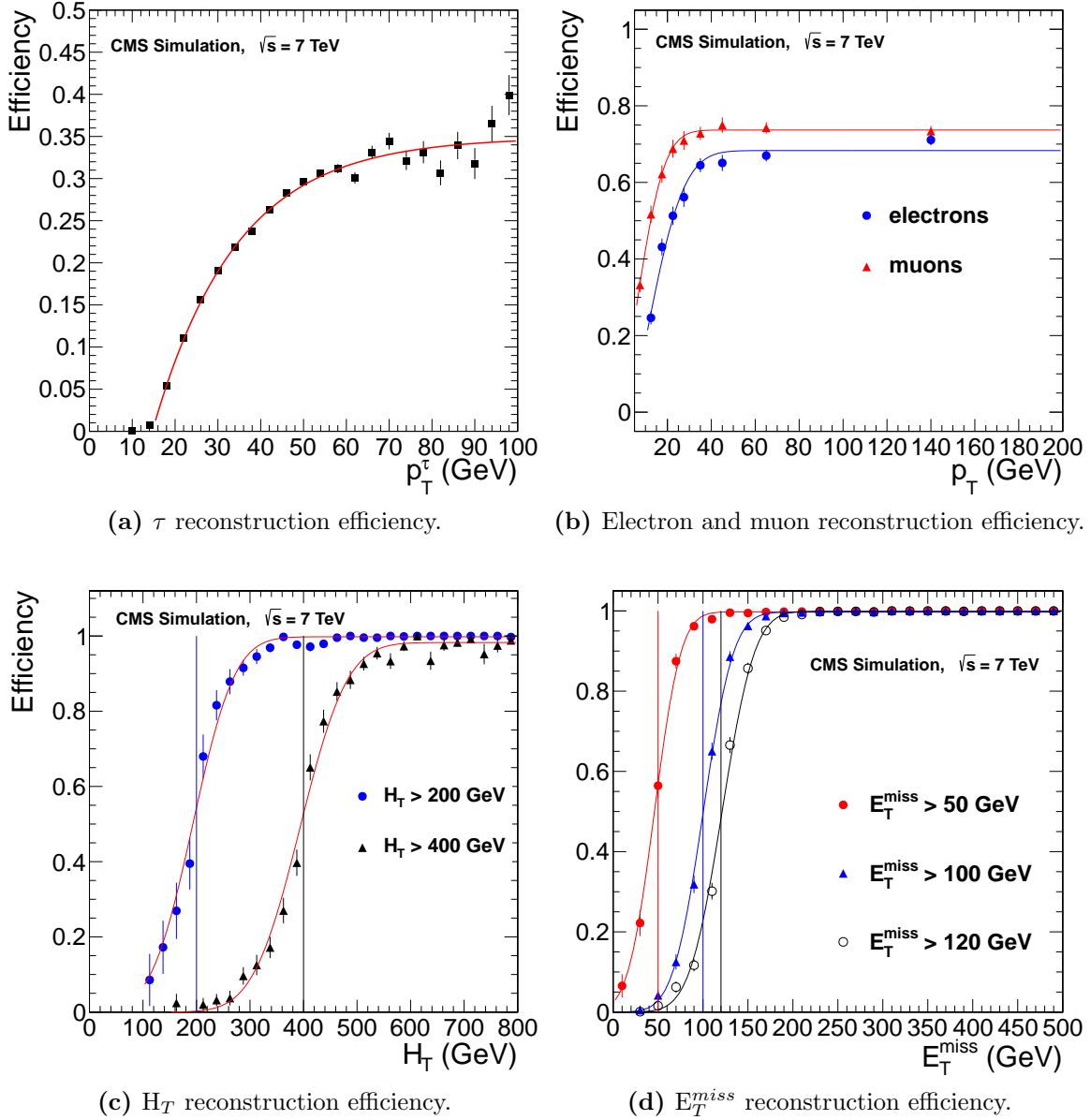
(d) E_T^{miss} reconstruction efficiency.

Figure A.1.: Lepton, H_T and E_T^{miss} reconstruction efficiencies evaluated in MC. Taken from [82].

$H_T > 400$ GeV and $E_T^{miss} > 120$ GeV are 0.987, 379 GeV and 113 GeV; 0.999, 121 GeV and 40 GeV for ϵ_{high}, $x_{1/2}$ and σ in the H_T and E_T^{miss} parameterisations respectively.

Appendix B.

Calculating Observed Limits

A full description of the CL_s method can be found in [94–96]. A summary of the procedure used to evaluate observed limits is presented below.

A likelihood function ($\mathcal{L}$) is constructed such that:

$$\mathcal{L}(data|\mu, \theta) = \mathrm{Poisson}(data|\mu \times s(\theta) + b(\theta)) \times p(\tilde{\theta}|\theta) \tag{B.1}$$

with $\mathrm{Poisson}(data|\mu \times s(\theta) + b(\theta))$ the Poisson probability of observing $data$ (the experimentally observed events), $s(\theta)$ and $b(\theta)$ the signal and background models with nuisance parameter θ (independent systematic uncertainties) and μ the signal strength modifier on ($\sigma/\sigma_{signal\ model}$). The probability density function $p(\tilde{\theta}|\theta)$ describes the probability of measuring the nuisance parameter $\tilde{\theta}$ given a true value θ. All uncertainties follow a log-normal distribution in the SSDL analysis.

A test statistic $\tilde{q}_\mu$ is used to compare $data$ for compatibility with $background$ and $background+signal$ hypothesis, with the signal being allowed to vary by μ as:

$$\tilde{q}_\mu = -2\ln \frac{\mathcal{L}(data|\mu, \hat{\theta}_\mu)}{\mathcal{L}(data|\hat{\mu}, \hat{\theta})} \tag{B.2}$$

The denominator and the numerator are both maximised. The floating parameters are (θ) and (μ, θ) in the numerator and denominator respectively which reach their maxima for ($\hat{\theta}_\mu$) and ($\hat{\mu}, \hat{\theta}$).

Following this, the values of θ (nuisance parameters) which best describe (i.e. maximise equation B.1) the observed $background$ ($\hat{\theta}_0^{obs}$) and $background+signal$ ($\hat{\theta}_\mu^{obs}$) are evaluated. Toy MC data are then generated to construct probability density functions for the test

statistic in both the *background* and *background+signal* hypotheses. The probability for a test statistic under the *background+signal* hypothesis to be as high or higher than the one observed in data can be found and the $CL_s(\mu)$ evaluated as the ratio:

$$CL_s(\mu) = \frac{P(q_\mu \geq q_\mu^{obs} | \mu \times s(\hat{\theta}_\mu^{obs}) + b(\hat{\theta}_\mu^{obs}))}{P(q_\mu \geq q_\mu^{obs} | b(\hat{\theta}_0^{obs}))} \tag{B.3}$$

A 95% CL UL on μ is then obtained for $CL_s = 1 - 0.95$. A point in a NP parameter space with $\mu \leq 1$ and $CL_s \leq 0.05$ is considered excluded.

Appendix C.

Cross–check in the $H_T > 350$ GeV and pfMET > 80 GeV Region

The results in the cross–check region ($H_T > 350$ GeV and pfMET > 80 GeV) are presented in the tables below. All the results were evaluated in a manner analogous to those presented in chapters 5 and 6. As shown in table C.6, no excess of events is observed over background.

Sample	$e\tau$	$\mu\tau$	$\tau\tau$	Total
QCD100-250	0.00 ± 668.19	0.00 ± 668.19	0.00 ± 668.19	0.00 ± 668.19
QCD250-500	0.00 ± 35.68	0.00 ± 35.68	0.00 ± 35.68	0.00 ± 35.68
QCD500-1000	0.00 ± 0.69	0.00 ± 0.69	0.00 ± 0.69	0.00 ± 0.69
QCD1000-inf	0.00 ± 0.05	0.05 ± 0.05	0.05 ± 0.05	0.10 ± 0.07
W+jets	0.00 ± 2.03	4.06 ± 2.87	0.00 ± 2.03	4.06 ± 2.87
Z+jets	0.00 ± 1.28	0.00 ± 1.28	0.00 ± 1.28	0.00 ± 1.28
γ +V+jets	0.15 ± 0.15	0.15 ± 0.15	0.00 ± 0.15	0.31 ± 0.22
$t\bar{t}$	2.06 ± 0.53	3.43 ± 0.69	0.14 ± 0.14	5.63 ± 0.88
WW	0.00 ± 0.02	0.06 ± 0.04	0.00 ± 0.02	0.06 ± 0.04
ZZ	0.00 ± 0.00	0.00 ± 0.00	0.00 ± 0.00	0.00 ± 0.00
WZ	0.03 ± 0.02	0.02 ± 0.01	0.01 ± 0.01	0.06 ± 0.02
SingleTop-schannel	0.00 ± 0.01	0.01 ± 0.01	0.00 ± 0.01	0.01 ± 0.01
SingleTop-tchannel	0.38 ± 0.22	0.26 ± 0.18	0.00 ± 0.13	0.64 ± 0.29
tW	0.02 ± 0.02	0.06 ± 0.04	0.00 ± 0.02	0.08 ± 0.04
W^+W^+ (SPS)	0.02 ± 0.01	0.05 ± 0.02	0.00 ± 0.00	0.07 ± 0.03
W^-W^- (SPS)	0.01 ± 0.01	0.01 ± 0.01	0.00 ± 0.00	0.02 ± 0.01
$W^\pm W^\pm$ (DPS)	0.00 ± 0.00	0.00 ± 0.00	0.00 ± 0.00	0.00 ± 0.00
$t\bar{t}$ W	0.02 ± 0.01	0.03 ± 0.01	0.00 ± 0.00	0.05 ± 0.02
Total Bkg	2.70 ± 0.60	8.19 ± 2.96	0.19 ± 0.15	11.08 ± 3.02
LM6	0.26 ± 0.02	0.37 ± 0.02	0.04 ± 0.01	0.66 ± 0.03

Table C.1.: MC results for the SSDL τ channels in the ($H_T > 350$ GeV and pfMHT $>$ 80 GeV) region discussed in section 4.2 weighted to 976 pb^{-1}. The errors shown are statistical. Zero event yields are attributed an error corresponding to one weighted MC event. Total errors are evaluated as the quadrature sum of individual contributions excluding those with zero yield.

	eτ	$\mu\tau$	$\tau\tau$	Total
Predicted (baseline)	2.2 ± 0.1	4.0 ± 0.9	0.2 ± 0.3	6.4 ± 0.9
Predicted (HT>150GeV)	2.7 ± 0.1	4.5 ± 0.9	0.2 ± 0.3	7.4 ± 0.9

Table C.2.: τ fake rate is evaluated in the baseline and $150 < H_T < 300$ GeV region. The predicted number of events is then evaluated for each region. The difference in predicted number of events is taken as the systematic error.

	eτ	$\mu\tau$	$\tau\tau$	Total
Predicted (baseline)	2.2 ± 0.1	4.0 ± 0.9	0.2 ± 0.3	6.4 ± 1.0
Predicted (*loose isolation* τ)	2.5 ± 0.2	7.0 ± 2.1	0.3 ± 0.3	9.8 ± 2.1

Table C.3.: Predicted number of events evaluated from the baseline definition of fake τ and with a loosely isolated definition of fake τ.

	eτ	$\mu\tau$	$\tau\tau$	Total
Predicted (rebin = 2)	2.6 ± 0.2	4.3 ± 0.9	0.1 ± 0.03	7.0 ± 0.9
Predicted (baseline)	2.2 ± 0.1	4.0 ± 0.9	0.2 ± 0.3	6.4 ± 0.9
Predicted (rebin = 10)	3.3 ± 0.1	3.7 ± 0.7	0.1 ± 0.2	7.1 ± 0.7

Table C.4.: Predicted number of background events with τ fake rate evaluated with the baseline definition before and after different binning in the $(|\eta|, p_T)$ plane.

Sample	eτ	$\mu\tau$	$\tau\tau$	Total
WW	0.00 ± 0.02	0.06 ± 0.04	0.00 ± 0.02	0.06 ± 0.04
ZZ	0.00 ± 0.00	0.00 ± 0.00	0.00 ± 0.00	0.00 ± 0.00
WZ	0.03 ± 0.02	0.02 ± 0.01	0.01 ± 0.01	0.06 ± 0.02
W^+W^+ (SPS)	0.02 ± 0.01	0.05 ± 0.02	0.00 ± 0.01	0.07 ± 0.03
W^-W^- (SPS)	0.01 ± 0.01	0.01 ± 0.01	0.00 ± 0.00	0.02 ± 0.01
$W^\pm W^\pm$ (DPS)	0.00 ± 0.00	0.00 ± 0.00	0.00 ± 0.00	0.00 ± 0.00
ttW	0.02 ± 0.01	0.03 ± 0.01	0.00 ± 0.00	0.05 ± 0.02
Total Bkg	0.08 ± 0.03	0.17 ± 0.05	0.01 ± 0.01	0.25 ± 0.06

Table C.5.: Irreducible background to the SSDL τ channels evaluated from MC in the baseline region. Errors shown are statistical. Zero event yields are attributed an error corresponding to one weighted MC event. Total errors are evaluated as the quadrature sum of individual contributions excluding those with zero yield.

	eτ	$\mu\tau$	$\tau\tau$	Total
Fake τ	2.2 ± 0.1 (stat.) ± 1.2 (syst.)	4.0 ± 0.9 (stat.) ± 3.1 (syst.)	0.2 ± 0.3(stat.) ± 0.1 (sys.)	6.4 ± 5.09
Charge MisID	1.0 ± 0.3 (stat.)± 0.4 (syst.)	1.5 ± 0.4 (stat.) ± 0.5 (syst.)	0.15 ± 0.15 (stat) ± 0.05 (syst)	2.7 ± 1.08
Irreducible Bkg	0.08 ± 0.03 (stat.)±0.04 (syst.)	0.17 ± 0.05 (stat.) ± 0.085 (syst.)	0.01 ± 0.01(stat.) ± 0.005 (syst.)	0.25 ± 0.14
Total	3.3 ± 1.3	5.7 ± 3.3	0.4 ± 0.4	9.3 ± 5.20
Observed	4	7	0	11

Table C.6.: Results found in data with predicted and observed events. The expected numbers of events in each channel are shown from the individual contributions considered in chapter 5 with statistical and systematic errors.

Appendix D.

Detailed Object Selection Criteria

The detailed selection criteria for all objects used in the SSDL analysis are listed below.

Electron Identification

- $p_T > 10$ GeV

- $|\eta| < 2.4$

- $1.44 < |\eta_{SC}| < 1.56$ excluded

- Identification cuts that have ~ 80 % efficiency for electrons from W/Z [75]:

  - $\sigma_{i\eta i\eta} < 0.01$ in the barrel and < 0.03 in the endcap

  - $d\phi_{in} < 0.06$ in the barrel and < 0.03 in the endcap

  - $d\eta_{in} < 0.004$ in the barrel and < 0.007 in the endcap

  - $H/E < 0.04$ in the barrel and < 0.025 in the endcap

- $|d0| < 0.02$ cm (taken with respect to the first Deterministic Annealing (DA) [101] vertex)

- Hit pattern and conversion rejections:

  - Number of missing hits in the inner tracker layers $= 0$

  - $|d\cot(\Theta)| > 0.02$ and $|dist| > 0.02$ of closest approach to conversion partner

- Charge consistency requirement: CTF, GSF and SuperCluster charges must all be equal

- Isolation requirements: $\text{RelIsolation}_{dR<0.3} < 0.15$, where RelIsolation is defined as: $\text{RelIsolation}_{dR<0.3} = (\text{TrkIso} + \text{ECALIso} + \text{HCALIso})/\text{p}_T$ in the endcaps ($|\eta| > 1.56$) and as: $\text{RelIsolation}_{dR<0.3} = (\text{TrkIso} + max(0., \text{ECALIso} - 1) + \text{HCAL}Iso)/\text{p}_T$ in the barrel ($|\eta| < 1.44$)

- No muons in $\Delta R < 0.1$

Muon Identification

A full description of muon identification and reconstruction may be found in [76].

- $\text{p}_T > 5$ GeV
- $|\eta| < 2.4$
- Global track $\chi^2/n.d.f < 10$
- Number of valid tracker hits > 10
- $|d0| < 0.02$ cm (taken with respect to the first DA vertex)

- Valid stand–alone hits > 0
- $\text{RelIsolation}_{dR<0.3} < 0.15$
- EcalVetoDep ≤ 4 GeV
- HcalVetoDep ≤ 6 GeV

τ Identification

- $\text{p}_T > 15$ GeV

- $|\eta| < 2.4$

- HPS τs matched with a ΔR cone to shrinking cone τs

- Discriminators for HPS τs [79, 84]:

  ByDecay – discriminates by the identified decay mode. The modes allowed are one prong, one prong + π^0, and three prong.

  ByMediumIsolation – requires no PF charged candidates with $\text{p}_T > 0.8$ GeV or PF–γ candidates with $\text{E}_T > 1.5$ GeV within an isolation cone of $\Delta R = 0.5$.

  ByMediumElectronRejection – (see 3.4) requires the e–π MVA discriminant to be < -0.1 and rejects the $1.4442 < |\eta| < 1.566$ (ECAL crack between barrel and endcaps).

ByLooseMuonRejection – no match between the leading τ track and any muon chamber hits.

- Discriminators for shrinking cone τs:

ByIsolation – requires no PF charged candidates with $E_T > 1$ GeV and no PF–γ candidates with $E_T > 1.5$ GeV inside the isolation annulus.

ByLeadingPionPtCut – requires the leading track to be contained within $\Delta R = 0.1$ of the jet axis, and requires either the leading PF charged hadron or the leading PF–γ to have $p_T > 5$ GeV.

AgainstElectron – similar to the HPS electron rejection requirement above.

AgainstMuon – similar to the HPS muon rejection requirement above.

ByLeadingTrackFinding – requires the leading track to be within $\Delta R = 0.1$ of the jet axis.

Jets and E_T^{miss} Selection

Jets

- PF AK(0.5) jets with loose identification [85]
- $p_T > 40$ GeV
- $|\eta| < 2.5$
- No muons in $\Delta R < 0.4$
- No electrons in $\Delta R < 0.4$
- No τs in $\Delta R < 0.1$

Missing Energy – pfMET, no correction.

PV requirements

Vertices

- Ndof ≥ 4

- $\rho < 2$ cm

- $|z| < 24$ cm

If more than one vertex is found, the first one in the collection passing the criteria listed above is taken.

Appendix E.

List of Acronyms

Bibliography

[1] Gargamelle Neutrino Collaboration, "Observation of neutrino-like interactions without muon or electron in the Gargamelle neutrino experiment", *Phys. Lett.* **B46** (1973) 138–140. `doi:10.1016/0370-2693(73)90499-1`.

[2] UA1 Collaboration, "Experimental observation of lepton pairs of invariant mass around 95 GeV/c^2 at the CERN SPS collider", *Phys. Lett.* **B126** (1983) 398–410. `doi:10.1016/0370-2693(83)90188-0`.

[3] UA1 Collaboration, "Experimental observation of isolated large transverse energy electrons with associated missing energy at $\sqrt{s} = 540$ GeV", *Phys. Lett.* **B122** (1983) 103–116.

[4] UA2 Collaboration, "Evidence for $Z^0 \rightarrow e^- e^+$ at the CERN anti-p p collider", *Phys. Lett.* **B129** (1983) 130–140. `doi:10.1016/0370-2693(83)90744-X`.

[5] UA2 Collaboration, "Observation of single isolated electrons of high transverse momentum in events with missing transverse energy at the CERN anti-p p collider", *Phys. Lett.* **B122** (1983) 476–485. `doi:10.1016/0370-2693(83)91605-2`.

[6] LEP Collaboration, "Precision Electroweak Measurements and Constraints on the Standard Model", `arXiv:hep-ex/0712.0929`.

[7] F. Abe et al., "Observation of Top Quark Production in $p\bar{p}$ Collisions with the Collider Detector at Fermilab", *Phys. Rev. Lett.* **74** (Apr, 1995) 2626–2631. `doi:10.1103/PhysRevLett.74.2626`.

[8] L. Evans and P. Bryant, "LHC Machine", *Journal of Instrumentation* **3** (2008) S08001. `doi:doi:10.1088/1748-0221/3/08/S08001`.

[9] CMS Collaboration, "CMS physics Technical Design Report, Volume II: Physics Performance", *J. Phys.* **G34** (2006), no. CERN-LHCC-2006-021.

CMS-TDR-008-2,.

[10] D. N. Spergel and P. J. Steinhardt, "Observational Evidence for Self-Interacting Cold Dark Matter", *Phys. Rev. Lett.* **84** (2000) 3760–3763, `arXiv:arXiv:astro-ph/9909386`. `doi:10.1103/PhysRevLett.84.3760`.

[11] M. E. Peskin and D. V. Schroeder, "An Introduction To Quantum Field Theory". Westview Press, 1995.

[12] CMS Collaboration, "Combination of SM, SM4, FP Higgs boson searches", *CMS Physics Analysis Summary* **CMS-PAS-HIG-12-008** (2012).

[13] S. P. Martin, "A Supersymmetry Primer", `arXiv:hep-ph/9709356`.

[14] J. Ellis, "Prospects for Discovering Supersymmetry at the LHC", *Eur. Phys. J.* **C59** (2009) 335–343, `arXiv:0810.1178`. `doi:10.1140/epjc/s10052-008-0790-4`.

[15] ATLAS Collaboration, "Search for Supersymmetry Signatures at the LHC"', `arXiv:0910.2964`.

[16] F. Halzen and A. Martin, "Quarks and Leptons: An introductory Course in Modern Particle Physics". John Wiley and Sons, 1984.

[17] D. Griffiths, "Introduction to Elementary Particles". John Wiley and Sons, 1987.

[18] P. Langacker, "Introduction to the Standard Model and Electroweak Physics", `arXiv:0901.0241`.

[19] S. Novaes, "Standard Model: An Introduction", `arXiv:hep-ph/0001283`.

[20] J. D. Wells, "Lectures on Higgs Boson Physics in the Standard Model and Beyond", `arXiv:0909.4541`.

[21] V. Bednyakov, N. Giokaris, and A. Bednyakov, "On Higgs Mass Generation Mechanism in the Standard Model", *Phys. Part. Nucl.* **39** (2008) 13–36, `arXiv:hep-ph/0703280`. `doi:10.1007/s11496-008-1002-9`.

[22] P. W. Higgs, "Broken Symmetries and the Masses of Gauge Bosons", *Physical Review Letters* **13** (1964) 508–509. `doi:10.1103/PhysRevLett.13.508`.

[23] G. S. Guralnik, C. R. Hagen, and T. W. Kibble, "Global Conservation Laws and Massless Particles", *Physical Review Letters* **13** (1964) 585–587.

`doi:10.1103/PhysRevLett.13.585.`

[24] F. Englert and R. Brout, "Broken Symmetry and the Mass of Gauge Vector Mesons", *Physical Review Letters* **13** (1964) 321–323. `doi:10.1103/PhysRevLett.13.321.`

[25] J. Goldstone, A. Salam, and S. Weinberg, "Broken Symmetries", *Phys. Rev.* **127** (1962) 965–970. `doi:10.1103/PhysRev.127.965.`

[26] M. Quiros, "Constraints on the Higgs Boson Properties from the Effective Potential", `arXiv:hep-ph/9703412.`

[27] K. Tobe and J. D. Wells, "Higgs Boson Mass Limits in Perturbative Unification Theories", *Phys. Rev.* **D66** (2002) 013010.

[28] J. Ellis, J. Espinosa, G. Giudice et al., "The probable fate of the Standard Model", *Physics Letters* **B679** (2009), no. 4, 369 – 375. `doi:10.1016/j.physletb.2009.07.054.`

[29] K. G. Begeman, A. H. Broeils, and R. H. Sanders, "Extended Rotation Curves of Spiral Galaxies: Dark Haloes and Modified Dynamics", *Mon. Not. Roy. Astron. Soc.* **249** (1991) 523.

[30] D. Clowe, M. Bradac, A. H. Gonzalez et al., "A Direct Empirical Proof of the Existence of Dark Matter", *Astrophys. J.* **648** (2006) L109–L113, `arXiv:astro-ph/0608407.` `doi:10.1086/508162.`

[31] N. Jarosik, C. Bennett, J. Dunkley et al., "Seven-Year Wilkinson Microwave Anisotropy Probe (WMAP) Observations: Sky Maps, Systematic Errors, and Basic Results", *Astrophys. J. Suppl.* **192** (2011) 14, `arXiv:1001.4744.` `doi:10.1088/0067-0049/192/2/14.`

[32] I. Aitchison, "Supersymmetry in Particle Physics: An Elementary Introduction". Cambridge Univ. Press, Cambridge, 2007.

[33] CMS Collaboration, "Search for Supersymmetry at the LHC in Events with Jets and Missing Transverse Energy", *Phys. Rev. Lett.* **107** (2011) 221804, `arXiv:1109.2352.`

[34] ATLAS Collaboration, "Search for squarks and gluinos using final states with jets and missing transverse momentum with the ATLAS detector in $\sqrt{s} = 7$ TeV proton-proton collisions", `arXiv:1109.6572.`

[35] "Summary of SUSY exclusions in 1fb^{-1} at CMS".
`https://twiki.cern.ch/twiki/bin/view/CMSPublic/PhysicsResultsSUS`.

[36] H. Baer, C.-h. Chen, F. Paige et al., "Signals for minimal supergravity at the
CERN Large Hadron Collider. II. Multilepton channels", *Phys. Rev.* **D53** (1996)
6241–6264. `doi:10.1103/PhysRevD.53.6241`.

[37] ATLAS Collaboration, "Prospects for standard SUSY searches at the LHC",
`arXiv:hep-ex/0810.3574`.

[38] R. M. Barnett, J. F. Gunion, and H. E. Haber, "Discovering supersymmetry with
like-sign dileptons", *Physics Letters* **B315** (1993), no. 34, 349 – 354.
`doi:10.1016/0370-2693(93)91623-U`.

[39] M. Guchait and D. P. Roy, "Like-sign dilepton signature for gluino production at
the CERN LHC including top quark and Higgs boson effects", *Phys. Rev. D* **52**
(Jul, 1995) 133–141. `doi:10.1103/PhysRevD.52.133`.

[40] R. Contino and G. Servant, "Discovering the top partners at the LHC using
same-sign dilepton final states", *JHEP* **06** (2008) 026.

[41] Y. Bai and Z. Han, "Top-antitop and Top-top Resonances in the Dilepton Channel
at the CERN LHC", *JHEP* **0904** (2009) 056.

[42] F. M. L. Almeida Jr, Y. A. Coutinho, J. A. M. Simoes et al., "Same-sign dileptons
as a signature for heavy Majorana neutrinos in hadron-hadron collisions", *Phys.
Lett.* **B400** (1997) 331.

[43] K. T. Matchev, F. Moortgat, L. Pape et al., "Precision superpartner spectroscopy
in the inclusive same-sign dilepton channel at the LHC", *Phys. Rev.* **D82** (2010)
077701. `doi:10.1103/PhysRevD.82.077701`.

[44] H. Baer, C.-h. Chen, M. Drees et al., "Collider Phenomenology for Supersymmetry
with Large tan Beta", *Phys. Rev. Lett.* **79** (1997) 986–989,
`arXiv:hep-ph/9704457`. `doi:10.1103/PhysRevLett.79.986`.

[45] U. Chattopadhyay, D. Das, A. Datta et al., "Nonzero trilinear parameter in the
minimal supergravity model: Dark matter and collider signals at the Fermilab
Tevatron and CERN LHC", *Phys. Rev.* **D76** (2007) 055008.
`doi:10.1103/PhysRevD.76.055008`.

[46] K. Kadota and J. Shao, "Enhanced Tau Lepton Signatures at LHC in Constrained

Supersymmetric Seesaw", *Phys. Rev.* **D80** (2009) 115004, `arXiv:0910.5517`. `doi:10.1103/PhysRevD.80.115004`.

[47] ATLAS Collaboration, "ATLAS: technical proposal for a general-purpose pp experiment at the Large Hadron Collider at CERN". LHC Tech. Proposal. CERN, Geneva, 1994.

[48] CMS Collaboration, "Technical proposal". LHC Tech. Proposal. CERN, Geneva, 1994.

[49] LHCb Collaboration, "LHCb : Technical Proposal". LHC Tech. Proposal. CERN, Geneva, 1998.

[50] ALICE Collaboration, "ALICE: Technical proposal for a Large Ion collider Experiment at the CERN LHC". LHC Tech. Proposal. CERN, Geneva, 1995.

[51] M. Benedikt, P. Collier, V. Mertens et al., "LHC Design Report", volume CERN-2004-003-V-1. CERN, Geneva, 2004.

[52] "CERN Accelerator Complex.". `http://www.cernmg.free.bg/en/cern3.jpg`.

[53] M. e. a. Bajko, "Report of the Task Force on the Incident of 19th September 2008 at the LHC. oai:cds.cern.ch:1168025", Technical Report LHC-PROJECT-Report-1168. CERN-LHC-PROJECT-Report-1168, CERN, Geneva, Mar, 2009.

[54] "Evolution of LHC luminosity in 2011". `http://lpc.web.cern.ch/lpc/lumiplots.htm`.

[55] "CMS luminosity up to 17 June 2011". `http://cms.web.cern.ch/news/cms-luminosity-exceeds-all-expectations`.

[56] The CMS Collaboration, "The CMS experiment at the CERN LHC", *Journal of Instrumentation* **3** (2008) S08004.

[57] "CMS Detector Drawing from CMSIM". `http://cmsinfo.web.cern.ch/cmsinfo/Resources/Website/Media/Images/Detector/DetectorDrawings/fromGEANT/cms_complete_labelled.eps`.

[58] C. Collaboration, "The CMS magnet project: Technical Design Report". Technical Design Report CMS. CERN, Geneva, 1997.

[59] V. e. a. Klyukhin, "The CMS Magnetic Field Map Performance", *Applied*

Superconductivity, IEEE Transactions on **20** (June, 2010) 152 –155. `doi:10.1109/TASC.2010.2041200`.

[60] CMS Collaboration, "Precise mapping of the magnetic field in the CMS barrel yoke using cosmic rays", *Journal of Instrumentation* **5** (2010), no. 03, T03021.

[61] C. Collaboration, "CMS Physics Technical Design Report Volume I: Detector Performance and Software". Technical Design Report CMS. CERN, Geneva, 2006.

[62] CMS Collaboration, "Tracking and Primary Vertex Results in First 7 TeV Collisions", *CMS Physics Analysis Summary* **CMS-PAS-TRK-10-005** (2010).

[63] T. Speer, W. Adam, R. Frhwirth et al., "Track reconstruction in the CMS tracker", *Nuclear Instruments and Methods in Physics Research Section A: Accelerators, Spectrometers, Detectors and Associated Equipment* **559** (2006), no. 1, 143 – 147. `doi:10.1016/j.nima.2005.11.207`.

[64] CMS Trigger and Data Acquisition Group Collaboration, "The CMS high level trigger", *Eur. Phys. J.* **C46** (2006) 605–667, `arXiv:hep-ex/0512077`. `doi:10.1140/epjc/s2006-02495-8`.

[65] CMS Collaboration, "Particle-Flow Event Reconstruction in CMS and Performance for Jets, Taus, and MET", *CMS Physics Analysis Summary* **CMS-PAS-PFT-09-001** (Apr, 2009).

[66] CMS Collaboration, "Commissioning of the Particle-flow Event Reconstruction with the first LHC collisions recorded in the CMS detector", *CMS Physics Analysis Summary* **CMS-PAS-PFT-10-001** (Apr, 2010).

[67] M. Cacciari, G. P. Salam, and G. Soyez, "The anti- k_T jet clustering algorithm", *Journal of High Energy Physics* **2008** (2008) 063.

[68] CMS Collaboration, "Jet Performance in pp Collisions at $\sqrt{s}$=7 TeV", *CMS Physics Analysis Summary* **CMS-PAS-JME-10-003** (2010).

[69] CMS Collaboration, "The Jet Plus Tracks Algorithm for Calorimeter Jet Energy Corrections in CMS", *CMS Physics Analysis Summary* **CMS-PAS-JME-09-002** (2009).

[70] CMS Collaboration, "Commissioning of the Particle-Flow reconstruction in Minimum-Bias and Jet Events from pp Collisions at 7 TeV", *CMS Physics Analysis Summary* **CMS-PAS-PFT-10-002** (2010).

[71] T. C. collaboration, "Determination of jet energy calibration and transverse momentum resolution in CMS", *Journal of Instrumentation* **6** (2011) P11002.

[72] CMS Collaboration, "Electron reconstruction and identification at $\sqrt{s}$=7 TeV", *CMS Physics Analysis Summary* **CMS-PAS-EGM-10-004** (2010).

[73] W. Adam, R. Frhwirth, A. Strandlie et al., "Reconstruction of electrons with the Gaussian-sum filter in the CMS tracker at the LHC", *Journal of Physics G: Nuclear and Particle Physics* **31** (2005) N9.

[74] CMS Collaboration, ""Study of photon conversion rejection at CMS"", *CMS Physics Analysis Summary* **CMS AN-2009/159** (2009).

[75] CMS Collaboration, "Measurement of the Inclusive W and Z Production Cross Sections in p p Collisions at sqrt(s) = 7 TeV with the CMS experiment", *JHEP* **10** (2011) 132, `arXiv:1107.4789`. `doi:10.1007/JHEP10(2011)132`. 1107.4789.

[76] CMS Collaboration, "Performance of muon identification in pp collisions at $\sqrt{s}$=7 TeV", *CMS Physics Analysis Summary* **CMS-PAS-MUO-10-002** (2010).

[77] CMS Collaboration, "Performance of CMS muon reconstruction in cosmic-ray events", *Journal of Instrumentation* **5** (March, 2010) 3022, `arXiv:0911.4994`. `doi:10.1088/1748-0221/5/03/T03022`.

[78] K. Nakamura and P. D. Group, "Review of Particle Physics", *Journal of Physics G: Nuclear and Particle Physics* **37** (2010) 075021.

[79] CMS Collaboration, "Performance of τ-lepton reconstruction and identification in CMS", *CMS Physics Analysis Summary* **CMS-PAS-TAU-11-001** (2011).

[80] CMS Collaboration, "CMS Strategies for tau reconstruction and identification using particle-flow techniques", *CMS Physics Analysis Summary* (2010).

[81] CMS Collaboration, "Search for new physics with same-sign isolated dilepton events with jets and missing transverse energy at the LHC", *Journal of High Energy Physics* (2011) 1–47. `doi:10.1007/JHEP06(2011)077`.

[82] CMS Collaboration, "Search for new physics with same-sign isolated dilepton events with jets and missing energy", *CMS Physics Analysis Summary* **CMS-PAS-SUS-11-010** (2011).

[83] CMS Collaboration, "CMS Trigger Approved Results".

`twiki.cern.ch/twiki/bin/viewauth/CMSPublic/L1TriggerDPGResults`.

[84] "PFTauDiscriminator CMS Twiki Page". `https://twiki.cern.ch/twiki/bin/view/CMSPublic/SWGuidePFTauID#Discriminators`.

[85] CMS Collaboration, "Jets in 0.9 and 2.36 TeV pp Collisions", *CMS Physics Analysis Summary* **CMS-PAS-JME-10-001** (2010).

[86] F. Maltoni and T. Stelzer, "MadEvent: Automatic event generation with MadGraph", *JHEP* **02** (2003) 027, `arXiv:hep-ph/0208156`.

[87] P. S. T. Sjostrand, S. Mrenna, "PYTHIA 6.4 Physics and Manual", *JHEP* **05** (2006) 026, `arXiv:hep-ph/0603175`.

[88] S. Jadach, Z. Was, R. Decker et al., "The tau decay library TAUOLA: Version 2.4", *Comput. Phys. Commun.* **76** (1993) 361–380. `doi:10.1016/0010-4655(93)90061-G`.

[89] "ROOT". `http://www.root.cern.ch`.

[90] J. Alwall, M. Herquet, F. Maltoni et al., "MadGraph 5 : Going Beyond", *JHEP* **06** (2011) 128, `arXiv:1106.0522`. `doi:10.1007/JHEP06(2011)128`.

[91] A. V. Manohar and W. J. Waalewijn, "What is Double Parton Scattering?", `arXiv:1202.5034`.

[92] CMS Collaboration, "On measuring transverse energy with the CMS detector in pp collisions at $\sqrt{s} = 7$ TeV", *CMS Paper in Preparation* **CMS-PAS-JME-10-009** (2010).

[93] CMS Collaboration, "Absolute Calibration of Luminosity Measurement at CMS: Summer 2011 Update", *CMS Physics Analysis Summary* **CMS PAS EWK-11-001** (2011).

[94] H.-L. Lai, J. Huston, Z. Li et al., "Uncertainty induced by QCD coupling in the CTEQ global analysis of parton distributions", *Phys.Rev.* **D82** (2010) 054021, `arXiv:1004.4624`. `doi:10.1103/PhysRevD.82.054021`.

[95] M. Bluj, "Standard Model Higgs Combination from CMS with up to 1.7 fb^{-1} of data", `arXiv:1201.5858`. Presented at the 2011 Hadron Collider Physics symposium (HCP-2011),Paris, France, November 14-18 2011, 4 pages, 4 figures.

[96] ATLAS and CMS Collaboration, "Procedure for the LHC Higgs boson search

combination in Summer 2011", *ATL-PHYS-PUB-2011-11/CMS NOTE-2011/005* (2011).

[97] B. Knuteson and S. Mrenna, "BARD: Interpreting new frontier energy collider physics", `arXiv:hep-ph/0602101`.

[98] N. Arkani-Hamed et al., "MARMOSET: The Path from LHC Data to the New Standard Model via On-Shell Effective Theories", `arXiv:hep-ph/0703088`.

[99] D. Alves, N. Arkani-Hamed, S. Arora et al., "Simplified Models for LHC New Physics Searches", `arXiv:1105.2838`.

[100] W. Beenakker, R. Hpker, M. Spira et al., "Squark and gluino production at hadron colliders", *Nuclear Physics* **B492** (1997) 51 – 103. `doi:10.1016/S0550-3213(97)80027-2`.

[101] E. Chabanat and N. Estre, "Deterministic Annealing for Vertex Finding at CMS", *Computing in High Energy Physics and Nuclear Physics 2004* (2004).